TOXICOLOGICAL AND PHARMACOLOGICAL ACTIONS OF ENGINEERED NANOMATERIALS

By

YONGBIN ZHANG

Doctor of Veterinary Medicine

China Agricultural University

Beijing, China

1997

Submitted to the Faculty of the
Graduate College of the
Oklahoma State University
in partial fulfillment of
the requirements for
the Degree of
DOCTOR OF PHILOSOPHY
May, 2009

TOXICOLOGICAL AND PHARMACOLOGICAL

ACTIONS OF ENGINEERED

NANOMATERIALS

Dissertation Approved:

Dr. Carey Pope

Dr. Melanie Breshears

Dr. Guangping Chen

Dr. Kevin Ausman

Dr. Michael Davis

Dr. A. Gordon Emslie

Dean of the Graduate College

ACKNOWLEDGMENTS

I wish to express my sincere appreciation to my major advisor, Dr. Carey Pope, for his intelligent supervision, constructive guidance and lasting friendship. My sincere appreciation extends to my other committee members Dr. Guangping Chen, Dr. Michael Davis, Dr. Melanie Breshears, and Dr. Kevin Ausman, whose assistant, guidance, encouragement are invaluable.

Moreover, I would like to express my sincere thank to those who have provided assistance and suggestions in my project : Dr. Joe Bidwell, Dr. Wei Chen, Dr. Shaopeng Wang, Dr. Yuanfang Liu, Dr. Satish Kuriyavar, Dr. Charlotte Ownby, Dr. Jerry Ritchey and Dr. Paul Weckler. I wish to thank the support and friendships from our lab members: Dr. Jing Liu, Dr. Subramana Karanth, Dr. Praveena Baireddy, Dr. Nikita Mirajkar, Dr. Anuradha Nallapaneni, Dr. Linnzi Wright, Ms. Nicole Singleton and Dr. Preeti Shanbhag.

I would also give my special appreciation to my wife Xinrong and my parents for their strong support, encouragement and understanding throughout this whole process. Also, I wish to thank my two wonderful children Andrew and Brian for making my life more enjoyable.

Finally, I wish to thank Dr. Carey Pope and the Department of Physiological Sciences for providing me the research opportunity and the generous financial support during my research.

TABLE OF CONTENTS

Chapter Page

LIST OF TABLES

Table Page

LIST OF FIGURES

Figure Page

Figure Page

Figure Page

LIST OF ABBREVIATIONS

ALT	alanine aminotransferase
AQ	aqueous
ANOVA	analysis of variance
BUN	blood urine nitrogen
BSA	bovine serum albumin
cm	centimeter
CM-H_2DCFDA	5-(and-6)-chloromethyl-2'7'-dichlorodihydrofluorescein diacetate acetyl ester
CdTe	cadmium telluride
DEM	diethyl maleate
DMSO	dimethyl sulfoxide
DMEM	Dulbecoo's Modified Eagle's Medium
DTT	dithiothreitol
DNA	deoxyribonucleic acid
dNTP	deoxyribonucleotide triphosphate
EDTA	ethylene diamine tetraacetic acid
EDC	1-ethyl-3-(3-dimethylaminopropyl
FBS	fetal bovine serum
Hr	hour
IC_{50}	concentration that inhibit 50%
i.v.	intravenous
i.p.	intraperitoneal
kg	kilogram
kJ	kilojoule
kD	kiloDalton
LDH	lactate dehydrogenase

LC	L-cysteine
MT	metallothionein
MTT	3-(4, 5-dimethylthiazol-2-yl) 2, 5-diphenyl tetrazolium bromide
MATP	meso-tetra (o-amino phenyl) porphyrin
mM	millimolar
mm	millimeter
ml	milliliter
nm	nanometer
NP	nanoparticle
NM	nanomaterial
NAC	N-acetyl-cysteine
PBS	phosphate-buffered saline
PI	propidium iodide
ppm	part per million
PAS	Photobeam Activity System
ROS	reactive oxygen species
RT-PCR	reverse transcription polymerase chain reaction
RNA	ribonucleic acid
RPMI	royal park memorial institute
rpm	revolutions per minute
SLUD	salivation, lacrimation, urination, defection
SDS	sodium dodecyl sulfate
SE	standard error
SON	sonication
s.c.	subcutaneous
THF	tetrahydrofuran
TTA	tetrahydrofuran toluene acetone
TBS	tris-buffered saline
TBE	tris-borate/EDTA
UV	ultra-violet

CHAPTER I

INTRODUCTION

Nanotechnology, a rapidly growing applied science, is expected to have a significant impact on almost all industries and all areas of society within the next decade. Nanomaterials, defined by the National Nanotechnology Initiative (NNI), have at least one dimension in the range of 1-100 nanometers. Due to their small size, the properties of nanomaterials may be different from those of their bulk substituents, showing unique chemical, physical, optical and electrical properties. Nanotechnology involves in creating and applying engineered materials at the nanoscale to take advantage of these specific properties. [1]. Potential applications of nanomaterials are being investigated in medicine, plastics, energy, electronics and aerospace. Obviously, nanotechnology, as “a new industrial revolution”, is expected to have a significant influence on many industries and our life in the future [2]. The National Nanotechnology Initiative (NNI) estimated nanotechnology could contribute trillion dollars to the U.S. economy by 2015, and 2 million people may be working in the nanotechnology field by that time [1]. Clearly, nanotechnology will play an important role in the world’s future economy.

Engineered nanoparticles have already been produced, sold, and used commercially in products such as sporting goods, tires, stain-resistant clothing, cosmetics, and imaging systems [3]. Sunscreens used in cosmetics containing nanoscale titanium dioxide or zinc oxide particles are transparent but effectively block ultraviolet rays [4]. Engineered nanomaterials designed to neutralize chemical spills are currently available. The number of future applications of nanomaterials appears almost limitless.

Semiconductor-based quantum dots are one type of nanoparticle. Due to their small size and a high surface to volume ratio, semiconductor nanoparticles have novel physical and chemical properties which make them attractive for applications in electronics, optical communications, environmental remediation, drug delivery, cancer therapy and biomedical imaging [5, 6]. While organic dyes have historically been used in cellular imaging, the broad spectral widths, photo-bleaching, complex synthetic chemistry, poor water solubility, and high cost of manufacturing constitute disadvantages for use of these probes. The use of luminescent nanoparticles can overcome some of these problems. The photophysical behavior of some luminescent nanoparticles allows fine tuning to select for discrete emission and excitation properties and thus may be advantageous for a variety of labeling and imaging applications [6]. *In vivo* applications often require that excitation and emission wavelengths are in the near-infrared (NIR) range from 700 to 1100 nm due to tissue penetration difficulties [7]. Many cadmium- and mercury-containing semiconductor nanoparticles meet this requirement. Among cadmium-containing nanoparticles

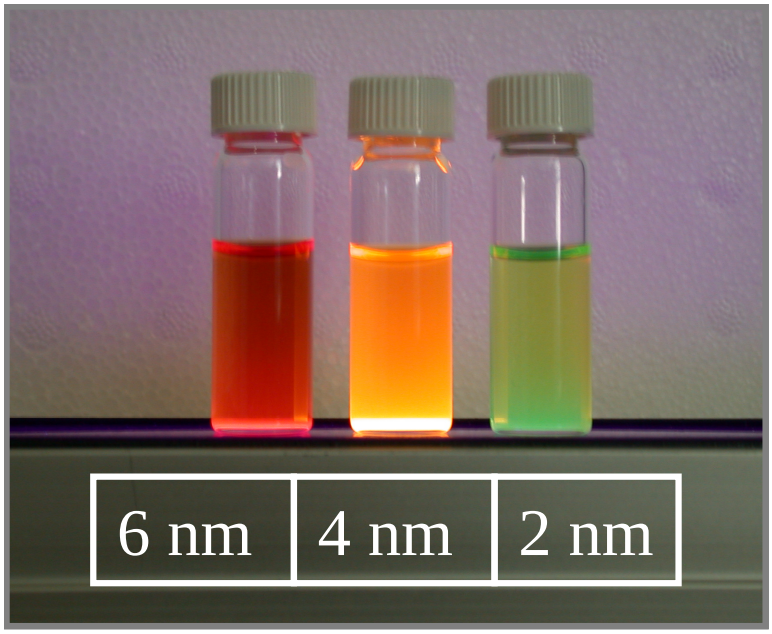

CdTe QDS

Figure 1. Three sizes of CdTe nanoparticle solution under Ultraviolet light

studied, cadmium telluride (CdTe) particles exhibit high photoluminescence quantum efficiencies, stable luminescence, and their emission can essentially cover the entire spectral range from blue to near infrared [8]. These unique properties make CdTe nanoparticles attractive candidates for imaging and many other biomedical applications. The toxic potential of these materials may limit their application potential, however.

The fullerenes, a family of carbon allotropes (C_{60}, C_{70}, and C_{80}…C_{200}) discovered in 1985, have attracted attention from different science and engineering areas, leading to the presentation of the 1996 Nobel Prize to Kroto, Smalley and Curl for their identification of these unique molecules. C_{60} was named after Richard Buckminster Fuller as buckminsterfullerene, or the "Bucky ball" [9]. Now, C_{60} and its derivatives are commonly referred to as fullerenes. This allotrope of carbon consists of 60 carbon atoms joined together to form a cage-like structure (see picture below). C_{60} is soluble in aromatic solvents (e. g, toluene or benzene), but insoluble in water and alcohol [10]. However, C_{60} can be functionalized (e.g., with –OH, -COOH, $-NH_2$) to increase its hydrophilicity. On the other hand, nanosized aqueous fullerene aggregates (nano C_{60} or nC60) can be generated by slowly mixing pure C_{60} in water or through a method involving solvent extraction. Some fullerenes have been shown to block human immunodeficiency virus (HIV) activity by inhibiting an HIV-associated protease, an essential enzyme for viral survival [11]. It was reported that some fullerenes can interact with biological membranes to elicit antimicrobial action [12, 13],

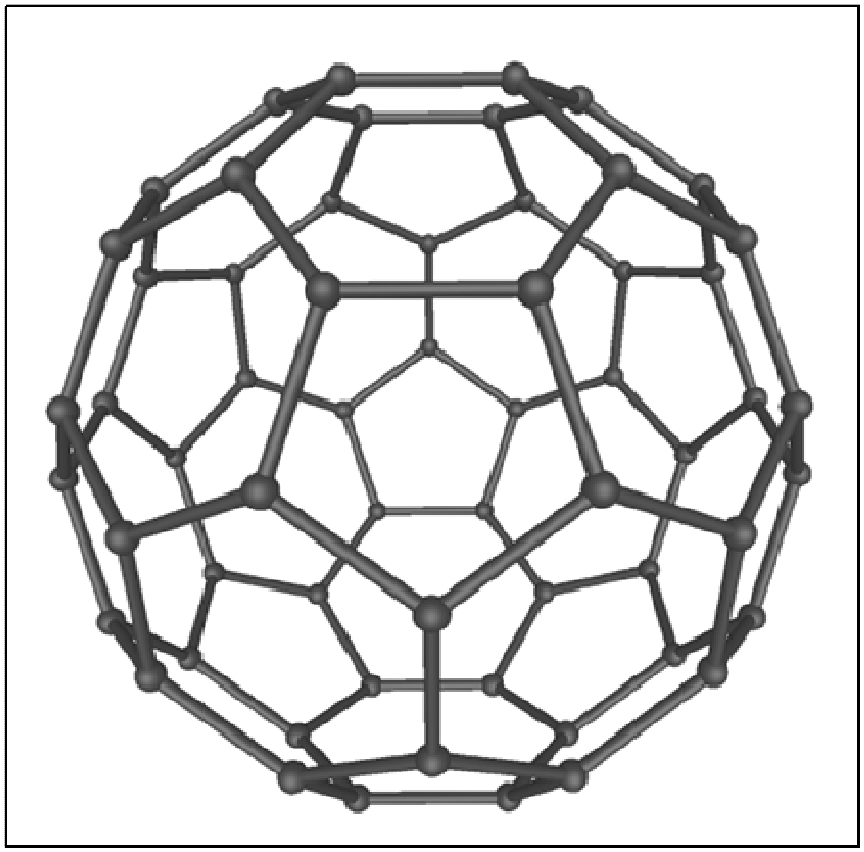

Figure 2. Cage-like structure of fullerene (C_{60})

antitumor activity [14], enzyme inhibition [15, 16], DNA photo cleavage [17, 18], and neuroprotective activity *via* antioxidant actions [19]. At present, fullerenes are commercially used in products including fuel cells, semiconductors and product coatings, e.g., bowling ball surfaces [1].

Health Concerns

Any new technology, before introduction into the market place, needs careful evaluation for health risks. Potential adverse effects of synthetic nanomaterials on human health and the environment are of concern. Exposures to natural airborne nanosized particles have been experienced by humans throughout time. Nanosized materials can be generated naturally from combustion processses such as forest fires and volcanic eruptions [4]. Respiratory diseases caused by coal mine dusts are well known from epidemiological studies and include coal worker's pneumoconiosis, chronic bronchitis, and emphysema [20-22]. There have been a number of papers highlighting the potential environmental hazards arising from nanotechnology [3, 23, 24]. Some nanoparticles appear to be able to distribute, deposit in organ systems, penetrate individual cells, and trigger toxic responses. Lam and coworkers reported that a suspension of carbon nanotubes (one of the most widely used types of nanomaterials) placed directly into mouse lungs caused granulomas, lesions that can interfere with gas exchange in the airways [25]. Warheit et al.reported that tracheal instillation led to the clustering of immune cells around nanotube deposits in the animals' lungs. At the highest dose

studied, 15% of the rats essentially suffocated due to the aggregation of the nanotubes and cells and subsequent blockade of the airways [26].

While a variety of semiconductor nanoparticle probes containing heavy metals have tremendous potential for applications in biomedicine, these constituent heavy metals (e.g., cadmium) have well known toxic potential. Relatively little is known, however, regarding the hazard potential of these and other types of nanoparticles. Size appears to be an important parameter, both for their photophysical properties and their toxic potential. As the entire field of nanotechnology is based on the size-dependent chemico-physical properties of these materials, it is not surprising that relative size would also be an important determinant of biological/toxicological effect. Oberdörster reported that surface area and particle size played important roles in the toxicity of inhaled TiO_2 particles, i.e., smaller particles induced lung tumors following inhalation at much lower exposures than larger particles of the same chemical composition [27]. Morgan and coworkers evaluated the pulmonary toxicity of cadmium gallium diselenide, copper indium diselenide and cadmium telluride “microparticles”, i.e., particles with 1,700-2,550 nm mean diameter, following intratracheal instillation in rats. Of the three, cadmium telluride elicited more extensive pulmonary damage (expressed as increased lung weight, decreased macrophages, increased lactate dehydrogenase and protein content in bronchoalveolar fluid, terminal bronchiolar necrosis with fibrin exudates, and type II cell hyperplasia) [28]. Ballou and colleagues demonstrated rapid elimination (half-lives of 12-70 minutes) of CdTe-ZnS nanoparticles following intravenous administration in mice, with surface

coating affecting tissue distribution [29]. Liver and lymph nodes were prominent sites of accumulation. Voura and coworkers used dihydroxylipoic acid-capped CdSe-ZnS semiconductor nanocrystals to label B16F10 tumor cells and follow cell extravasation in vivo after intravenous administration of the cells in mice [30]. Derfus and coworkers found that CdSe nanoparticles were cytotoxic under certain conditions, and the toxicity correlated with the liberation of free Cd^{2+} ions [31]. Lovric and colleagues reported marked cytotoxicity in PC12 and N9 cells exposed to CdTe nanoparticle concentrations as low as 10 µg/ml. Cell death was associated with chromatin condensation and membrane alterations and was more prominent with smaller sized (green,about 2 nm) than larger (red, about 5 nm) nanoparticles [32].

An important feature of the potential biological actions of fullerenes is their oxidative potential. A number of reports suggest that the carbonaceous fullerenes may act as free-radical “scavengers” [33]. Gharbi et al reported that fullerenes (up to 2 g/kg) had no acute or subacute toxicity in rats following intraperitoneal injection [34]. Interestingly, pristine C_{60} dramatically protected the liver from subsequent exposure to the prototype hepatotoxicant and free radical generator, carbon tetrachloride. Fullerenes could be detected in liver using transmission electron microscopy. Normal serum marker enzyme (ALT) levels in animals pretreated with C_{60} before carbon tetrachloride suggested a lack of hepatotoxicity [34]. A water soluble, polyalkylsufonated C_{60} preparation elicited essentially no evidence of toxicity or histopathology following acute or repeated oral dosing, whereas following intraperitoneal (500-600 mg/kg) or intravenous (100 mg/kg)

exposure renal toxicity appeared to be the major effect, and the kidneys appeared to be the major route of elimination [35]. Yamawaki and Iwai reported that endothelial cell cytotoxicity was evident following exposure to hydroxyl fullerenes (100 µg/ml for 24 hours): cell death appeared to be mediated through a ubiquitin-autophagy activation pathway [36]. Nelson and coworkers reported no acute or subchronic dermal toxicity of fullerenes in mice [37]. In contrast o these studies,on fullerenes some reports suggest that fullerene aggregates (nC60) may induce oxidative stress. Sayes et al reported that nC_{60} generated a large amount of reactive oxygen species at low concentrations, leading to lipid peroxidation in biological systems [38]. It has been reported that neither nC_{60} nor hydroxylated C_{60} elicited respiratory toxicity following either acute or subacute in vivo dosing (intratracheal instillation), based on bronchoalveolar lavage (BAL) fluid biomarkers, oxidative stress endpoints, airway parenchymal cell proliferation and histopathological evaluations [39]. Oberdörster et al reported lipid peroxidation and glutathione depletion in the brain of largemouth bass 48 hours after exposure to 0.5 ppm uncoated nC_{60} [40]. Interestingly, Isakovic and coworkers reported that gamma-irradiated nC_{60} did not generate ROS or elicit cytotoxicity, and suggested that previously reported cytotoxicity of nC_{60} may at least be partially due to residual organic solvent (tetrahydrofuran) used in their syntheses [41]. The diversity of findings on fullerene and fullerene aggregate toxicity may therefore be due to the different preparation methods used, storage time between preparation and use, and other factors, in particular relative to the organic solvent(s) used and itsremoval from or retention in the final product.

The amount of information available on the toxicity of different nanomaterials is limited. Due to different characteristics such as size, shape, surface coating, chemical substituents, physical properties, etc., evaluation of the toxicity of different nanomaterials requires a case-by-case approach and strict adherence to careful charaterization of the materials under study [4, 42]. In addition, evaluation of the adverse effects of nanomaterials should consider the potential route of exposure. Inhalation exposure may be more appropriate with materials that would likely be air contaminants, while dermal exposure might be the best model when materials are contained in products such as sunblock creams. Nanoparticles contained in food or drinking water may be absorbed or cross into the gut lymphatics and redistribute to other organs, and oral absorption could therefore be a concern [43-45]. Some nanomaterials including nanotubes, fullerenes, and quantum dots may be designed to be intentionally introduced into the body for diagnostic or therapeutic purposes [34, 46, 47]. In such cases, the intravenous exposure route may be appropriate. Surface or other modifications of nanomaterials may influence their relative ability to enter cells and tissues/organs [40, 48]. Processes of absorption, distribution, metabolism, and excretion of nanoparticles may be different based on their surface characteristics. At the cellular and molecular level, the interaction between nanomaterials and biological target molecules is still unclear. Knowledge of the mechanism of cytotoxicity of nanoparticles in biological systems is beneficial for understanding their ultimate hazard potential.

Mechanisms of Nanotoxicity

With the widearray of possible constituents making up nanomaterials, there are numerous mechanisms that could potentially contribute to their toxicity. Oxidative stress has been suggested as a basic mechanism of toxicity that could participate in the adverse effects of many types of engineered nanomaterials. Oxidative stress is broadly defined as an imbalance between reactive oxygen species generated and antioxidant capacity, leading to tissue damage [49]. Under physiological conditions, reactive oxygen species (ROS) are generated at relatively low rates such that cellular antioxidant systems can counteract their reactivity and prevent cellular damage. Oxidative stress leads to a reduction in the amount of reduced glutathione (GSH, a major reducing agent in most cell types), with a concurrent increase in oxidized glutathione (GSSG). Free radicals and peroxides generated under these conditions can damage many cellular macromolecules including proteins, lipids, and nucleic acids. Oxidative stress is thought to play an important role in various disease processes including cardiovascular disease, neurodegenative disease, lung disease, diabetes, cancer and others [50-54]. On the other hand, reactive oxygen species can be beneficial, e.g., in immune functions in the destruction of pathogens [55].

An important source for reactive oxygen species is the mitochondria, produced during the process of oxidative metabolism. In addition, NADPH oxidases and cytochromes P450 are capable of generating superoxide. The enzymes superoxide dismutase (SOD), catalase and glutathione peroxidase are widely known to participate in antioxidant processes. Enriching the antioxidant

capacity has therapeutic benefits, e.g., Vitamine E supplementation has been used to treat Alzheimer's disease [56, 57], and radical scavenging drugs have been utilized in the treatment of stroke [58].

A number of studies have evaluated the possible role of oxidative stress in lung damage elicited by inhaled particles [4, 59, 60]. Occupational exposure to mineral dusts, quartz particles, and asbestos fibers has been shown to elicit oxidative damage, inflammation and cytotoxicity. Intratracheal instillation of TiO2 nanoparticles in rats led to an enhanced inflammatory response compared to that elicited by larger size (micro) particles with the same composition and mass [60]. Single walled carbon nanotubes induced transient lung inflammation and granulomas after intratracheal instillation in rats, possibly through generation of reactive oxygen species [25]. The specific properties of engineered nanoparticles, their composition and presence of impurities, and environmental factors (e.g., light) may modulate the surface of such particles, making them more reactive with biological systems. Endpoints of oxidative stress may therefore be useful for predicting the relative toxicity of different nanoparticles.

Cell death elicited by oxidative stress could be mediated either by apoptosis or necrosis [61, 62]. Both modes of cell death have distinct morphological and biochemical markers. The cell undergoing apoptosis shows nuclear condensation, membrane shrinkage and chromatin fragmentation, while integrity of the plasma membrane and cellular organelles is maintainted until very late in the cytotoxic process. In contrast, necrotic cells show membrane and nuclear swelling and membrane damage in relatively early stages, while

organelle damage occurs only later. Caspase activation is often a prominent, early step in the induction of apoptosis. Proximal caspases cleave and thereby activate downstream caspases, and thereby amplify the “death” signal. Apoptosis is involved in the toxicity of numerous xenobiotics (e.g., heavy metals, radiation), genotoxic drugs and a number of biological ligands such as Fas-L and tumor necrosis factor (TNF) [63-66]. Most of these factors can induce apoptosis and/or necrosis in a time- and dose-dependent manner [67-69].

In the preparation of nanomaterials (e.g., CdTe, carbon nanotubes), metal residues are often present, and metal reactivity may change (e.g., because of the release of free metal from nanomaterial degradation) between the time of nanomaterial synthesis and their use. The intracellular protein metallothionein (MT) is known to bind to many heavy metals with high affinity and capacity [67]. Metallothioneins are a family of low molecular weight (6-7 kDa), cysteine-rich proteins which could be important in binding to heavy metals possibly released by metal-containing nanomaterials. Although the physiological function(s) of MTs is unclear, heavy metal detoxification and protection against oxidative stress are generally agreed to be important activities. MTs participate in the uptake, transport, and regulation of zinc in biological systems through binding with the thiol group of the cysteine residues. Therefore, by binding and releasing zinc, MTs regulate the levels of this essential metal throughout the body. On the other hand, cysteine residues from MTs can capture oxidant radicals (e.g., superoxide and hydroxyl radicals) [70]. In this reaction, cysteine is oxidized to cystine and zinc is released, which can then activate the synthesis of more MTs [71]. Metal-

containing nanoparticles may therefore activate the synthesis of MT expression and this could be important in the regulation of oxidative stress.

As stated before, relatively little is known about the toxicity of nanomaterials. A number of studies suggest that the toxicity of nanoparticles can be based on multiple factors related to their different physico-chemical properties and extrinsic/environmental conditions [2]. However, the present toxicity data is still limited to elucidate the relative hazards and toxic mechanism(s) of diverse nanomaterials, including their potential subcellular localization and tissue distribution following systemic administration. Due to their relatively larger surface area , nanoparticles may be more bioactive than larger, “fine” particles made of the same constituents. As noted above, some toxic components (e.g., heavy metals) may be released from nanoparticles during synthesis, during storage or within biological or environmental systems [31]. In addition, nanoparticles may aggregate in biological systems to influence uptake, cellular activity, and elimination. On the other hand, nanoparticles may bind to the cell surface because of the interaction with cell surface proteins or lipids. One possibility is that smaller sized particles may enter cell nuclei and affect gene transcription whereas larger particles may fail to enter cells or be restricted to distribution only within the cytosol. Differential subcelluar localization of nanoparticles could therefore contribute to differential mechanisms of toxicity. Nanoparticles may distribute into tissues throughout the body, complex with plasma proteins, be retained, or be effectively excreted. All these processes will ultimately contribute to the toxic potential of the particular nanomaterial.

The selective use of nanotoxicity, e.g., for targeting cancer cells, has numerous applications in medicine. Ovarian cancer is the fifth leading cause of cancer deaths in US women. The American Cancer Society estimated over 22,000 new cases of ovarian cancer with over 15,000 deaths in 2007 [72]. Conventional therapy involves surgery followed by chemotherapy or radiation therapy to eliminate residual malignant cells. Although surgical techniques and chemotherapy have markedly improved in recent years, postsurgical pain and complications, non-specific targeting and adverse effects of chemotherapy and radiotherapy remain problematic [73]. Development of safer alternatives and more selective treatment approaches are needed [74-76]. One of the most promising approaches is selective photodynamic therapy (PDT) mediated by reactive oxygen species. Photodynamic therapy combines three relatively safe elements (photosensitizer, light and oxygen) to produce the ultimate toxicant reactive oxygen species, i.e., singlet oxygen ($^1O_2$). Essentially, light is used to activate a photosensitizer which transfers energy to molecular oxygen, which in turn generates singlet oxygen to elicit cytotoxicity. Ideally, the photosensitizer would be selectively targeted and accumulate in the cancer cells , thereby eliciting selective damage to those cells only. Moreover, PDT can be used in combination with chemotherapy, radiotherapy and/or surgery [77]. The first generation photosensitizers were hematoporphyrin derivatives, e.g., Photofrin®, but considerable side effects were noted with their use. For example, the “capillary-leak syndrome” with substantial fluid loss was found in some patients after de-bulking surgery and photodynamic therapy [78]. Second generation

photosensitizers (e.g., benzoporphyrins, chlorines, naphthalocyanines) have some advantages but have lesser selective accumulation in cancerous tissues [79].

The continuing development of nanotechnology has the potential for markedly improving a variety of treatments including PDT[80]. A number of studies indicate improved drug delivery and targeting *via* nanomaterial conjugation [46]. It was reported that phthalocyanine could be easily taken up by HeLa cells after conjugation with gold nanoparticles, enhancing their phototoxicity [81]. The photosensitizer *meta*-tetra (hydroxyphenyl)-chlorin (m-THPC) embedded in a sol-gel silica matrix generated more reactive oxygen species than the same photosensitizer alone [82]. Ideta and coworkers [83] reported the utility of a micelle-loaded dendritic form of photosensitizer at destroying neovascular lesions contributing to macular degeneration.

A novel therapeutic strategy referred to as self-lighting photodynamic therapy (SLPDT) has been recently designed, using nanoparticle conjugates to activate photosensitizers for photodynamic therapy [84]. Nanoparticles are conjugated with the photosensitizer and targeted to cancer cells. In the presence of irradiation and oxygen, the nanoparticles are activated to emit strong luminescence or scintillation, which in turn activates the conjugated photosensitizer to locally generate singlet oxygen and destroy the cancer cell [84]. For some applications, ZnO nanoparticles may be one of the best candidates for this application, e.g., their UV emission matches well with the UV absorption of most porphyrin photosensitizers [84]. In addition, strong x-ray

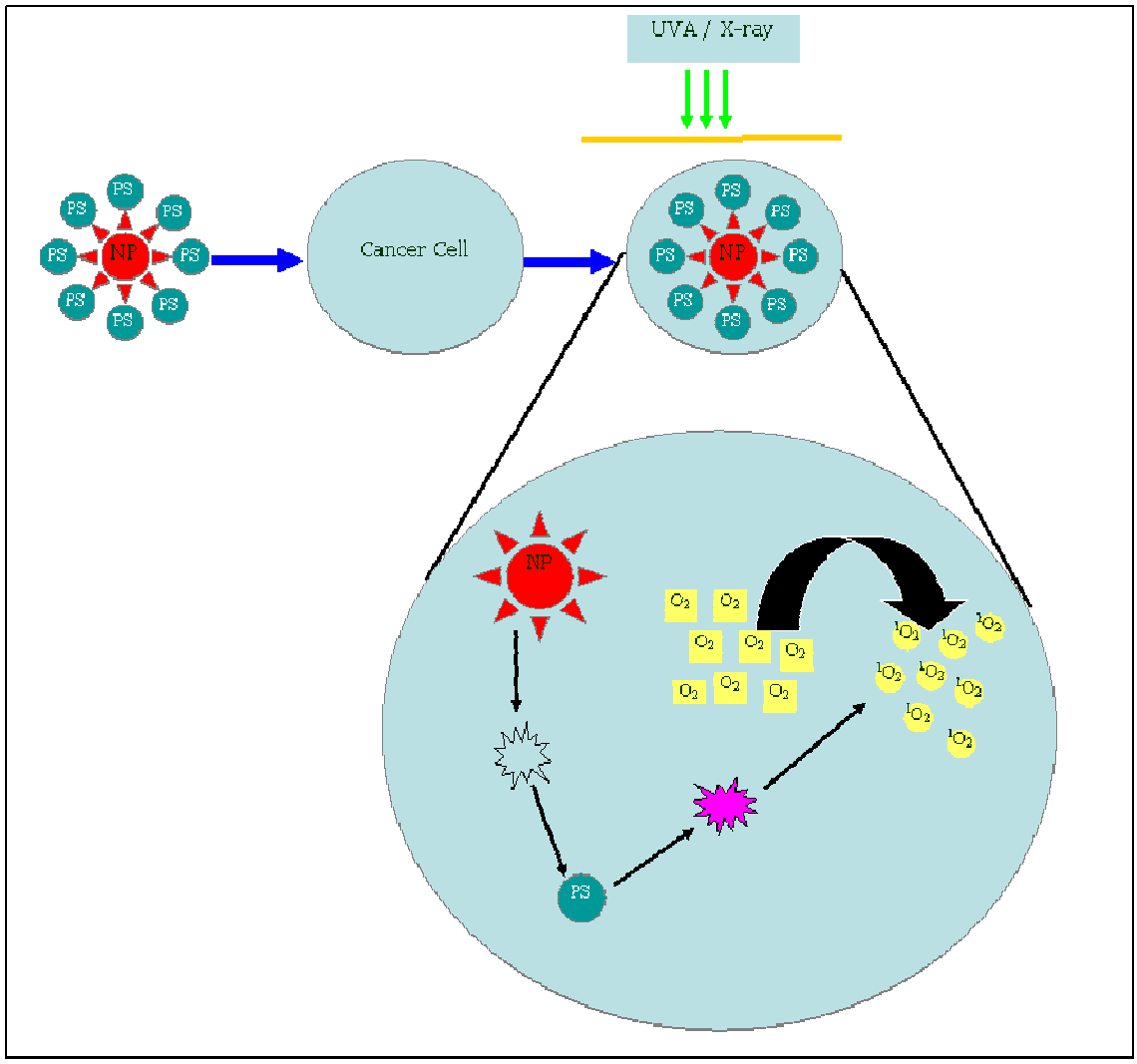

Figure 3. Schematic Self-lighting Photodynamic Therapy

excited luminescence has been observed in ZnO nanoparticles [85]. We recently reported the synthesis of a number of water-soluble ZnO nanoparticles with strong photoluminescence and their conjugation to a porphyrin derivative (meso-tetra (o-amino phenyl) porphyrin) in aqueous conditions [86].

In summary, nanomaterials are a diverse group of chemicals with high variability in chemical and biological reactivity. The evaluation of toxicity of nanomaterials is a requirement for their effective application. Understanding basic mechanisms of reactivity and toxicity could aid in the design of safer nanomaterial-based products, and potentially in the production of therapeutic tools that can harness and focus the biological reactivity of nanomaterials. A basic mechanism of toxicity that may be shared among different types of nanomaterials is oxidative stress. Based on the above background information, we hypothesized that CdTe, fullerenes and zinc oxide-porphyrin conjugates can all elicit in vitro and in vivo toxicity via generation of reactive oxygen species and subsequent oxidative stress**.** We investigated the relative cytotoxicity, cytotoxic mechanisms and subcelluar distribution of the selected nanoparticles in cultured cells. We also evaluated the in vivo effects of CdTe semiconductor nanoparticles and their distribution following systemic administration. To test our hypotheses, we developed the following specific aims:

1. Evaluate the toxicity and distribution of CdTe nanoparticles in both cellular and mammalian (rat) models
2. Assess the phototoxicity and subcellular distribution of ZnO-MTAP nanoparticle conjugates in human ovarian cancer cells (NIH OVCAR-3)

3. Investigate the cytotoxicity of fullerene aggregates (i.e., nano C_{60} or nC_{60}) and their cellular distribution in cells
4. Determine the role of reactive oxygen species/oxidative stress in the toxicity of CdTe, nC_{60}, and ZnO nanoparticle conjugates

CHAPTER 2

MATERIALS AND METHODS

Chemicals and Reagents

3-(4,5-dimethylthiazol-2-yl)-2,5-diphenyl tetrazolium bromide (MTT), N-acetyl-cysteine (NAC), di-ethyl maleate (DEM)), dimethylsulfoxide (DMSO), Trypan blue, Dulbecco's Modified Eagle's Medium/Nutrient Mixture F-12 Ham (DMEM/Hams') and RPMI-1640 media were purchased from Sigma Chemical Company (St. Louis, MO). Caspase-Glo 3/7 kit, and Cytotox 96-Non-Radioactive Cytotoxicity kit to measure lactate dehydrogenase release (LDH) were purchased from Promega Company (Madison, WI). The fluorescent dye Hoechst 33342, propidium iodide (PI) and the reactive oxygen species probe CM-H_2DCFDA were purchased from Invitrogen Corporation (Carlsbad, CA). Fetal bovine serum (FBS) was obtained from Hyclone (Logan, UT). The plastic wares for cell culture were obtained from Falcon, Becton Dickinson Company (San Jose, CA).

Cadmium telluride nanoparticles (CdTe) and zinc oxide nanoparticle conjugates (ZnO-MTAP) were synthesized at ICx Technologies (Stillwater, OK). These nanomaterials were stored 4^{o}C in the dark. Fullerene aggregates (nC60) were provided by Dr. Kevin Ausman in the Department of Chemistry at Oklahoma State University (Stillwater, OK) and stored at room

temperature under dark conditions. Considering that synthesis methods can potentially affect the chemical properties of the nanomaterials, the synthesis methods are briefly described below.

CdTe nanoparticles were prepared by the reaction of cadmium perchlorate hydrate [$Cd(ClO_4)_2*H_2O$] and hydrogen telluride (H_2Te) under vigorous stirring. The Cd^{2+} containing solution was prepared as follows: 0.7311 g of $Cd(ClO_4)_2*H_2O$ was dissolved in 125 mL of water. Thioglycolic acid (TGA, 0.396 ml) was added to the solution and the pH was adjusted to ~11 by the addition of 0.1M NaOH. The solution was then purged with nitrogen for at least 30 minutes. H_2Te gas was generated by the chemical reaction of excess aluminum telluride with 0.5 M sulfuric acid in an inert atmosphere (N_2) and was combined with the above solution. After the completion of the reaction, a yellowish solution of CdTe nanocrystal nuclei was obtained. This solution was then refluxed at 100^oC to promote crystal growth. Particle size was controlled by reaction time and evaluated by transmission electron microscopy. The nanoparticles of different sizes were extracted at different reaction times and stored at 4^oC in the dark. Using a similar procedure, CdTe nanoparticles were also synthesized in air instead of N_2 as described before [87]. Both samples showed similar photoluminescence efficiency.

For ZnO synthesis, 2.5×10^{-4} mol of $ZnAc_2.2H_2O$ and 50 ml of diethylene glycol were mixed in a 100 ml three-neck flask, and heated under stirring for 10 min., resulting in 5×10^{-3} mol/L of ZnO fluorescent nanoparticles. Ten ml 5×10^{-3} mol/L of such prepared ZnO diethlene glycol solution and 0.1 ml 0.5 M L-cysteine

in water were then mixed and heated at 60℃ for 48 hr to form ZnO-L-cysteine (ZnO-LC). The pH of the obtained ZnO-LC was adjusted to 7.0. The nanoparticles were purified with Econo-Pac 10DG desalting column (Bio-Rad) with a molecular cut-off of 6 kD. ZnO nanoparticles were conjugated to porphyrin by adding 9.58 mg of 1-ethyl-3-dimethylaminopropyl (EDC) to 10.85 mg of N-hydroxysulfosuccinimide (sulfo-NHS) and mixing into 10 ml 5×10^{-3} mol/L of ZnO-L-cysteine solution. This was allowed to react for 15 min at room temperature. Then 8.4 mg of MTAP [meso-tetra (o-amino phenyl) porphyrin] was added to and allowed to react for at least 2 hr. The pH of the obtained ZnO conjugates was adjusted to 7.0 and purified on the desalting column as above.

Animals

All procedures involving animals were in accordance with protocols outlined in the NIH/NRC *Guide for the Care and Use of Laboratory Animals* and approved by the Institutional Animal Care and Use Committee at Oklahoma State University. Male, Sprague-Dawley rats (30 days of age) were used throughout to evaluate potential *in vivo* toxicity of the CdTe (6 nm) nanoparticles. The rats were purchased from Harlan Sprague-Dawley (Indianapolis, IN) and housed in steel mesh cages with a 12h:12h light:dark illumination cycle and free access to food and water. Female BALB/c nude mice (5 weeks of age) from Charles River Laboratory were used in ovarian tumor development studies. The mice were housed in a micro-isolator cage and given standard autoclaved food pellets and water. The animals were allowed to acclimimate for 1 week after arrival.

Acute Toxicity and Tissue Distribution Studies

Animal Treatment

In the acute toxicity study, rats were divided into 2 experimental groups (n=8 per treatment group): control rats received vehicle (PBS, 1 ml/kg *via* tail vein) while treated rats received CdTe red nanoparticles (2 mM, 1 ml/kg).

In the tissue distribution study, rats were divided into 4 groups (n=6 per treatment group): control rats received 1 ml PBS while, the treated groups received CdTe red nanoparticles: 5 mM CdTe red nanoparticles at 1 ml/kg, 2 ml/kg, or 5 ml/kg.

Tail Vein Injection Procedure

The treated rat was restrained within a polypropylene device that allowed access to the tail vein. The tail was warmed using a lamp for about 30 seconds and then wiped with gauze containing 70% alcohol. The lateral tail vein was identified on one side and a tuberculin syringe with a 27-gauge needle was used to inject solution into the vein. Fluid could be seen entering the vein during the injection. After the needle was removed, a gauze was used to impair bleeding before the animal was returned to its home cage.

Functional and Behavioral Measurements

Animals were observed at 0, 0.5, 1, 2, and 4 hours and just before sacrifice at 24 hours after dosing. Involuntary movements and SLUD signs (acronym for signs of autonomic nervous system disruption including salivation, lacrimation, urination, and defection) were evaluated by the method of Moser and co-workers as previously described [88]. Involuntary movements were scored as

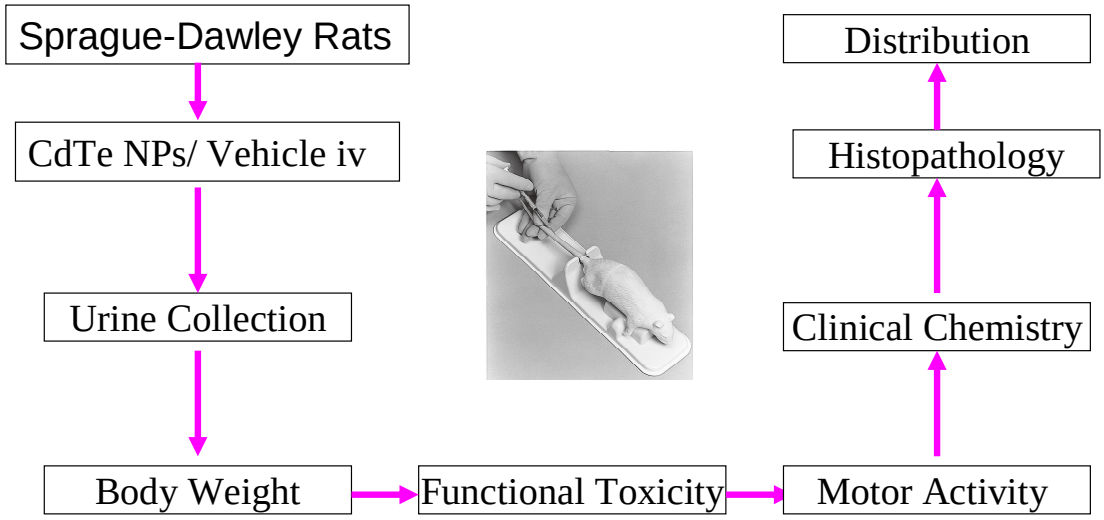

Figure 4. Flow chart showing toxicity evaluation

2 (normal quivering of vibrissae, head and limbs); 3 (mild, fine tremor typically seen in the forelimbs and head); 4 (whole body tremor). Autonomic dysfunction was scored as 1 (normal, no excessive secretion); 2 (slight, 1 SLUD sign or very mild multiple signs); 3 (moderate, multiple, overt SLUD signs); and 4 (severe, multiple, extensive SLUD signs).

Locomotor Activity Measurement

Motor activity was measured for two hours a) on the day before dosing, b) immediately following dosing, and then c) 24 hours after dosing. Ambulation and rearing were measured using a 16 home-cage-based Photobeam Interruption System and the Photobeam Activity System Control Software for Windows NT4 (PAS, San Diego Instruments, San Diego, CA). Each rat was treated and placed into a clean polycarbonate cage (with fresh bedding approximately 2 cm deep) just prior to beginning motor activity measurements. Motor activity was measured for the subsequent two hours (1000-1200 hrs) and data are reported as counts/2 hour observation period.

Clinical Chemistry

The rats were transferred to metabolic cages (Mini-mitter, #650-0100-00) through the remainder of the light cycle for collection of urine and subsequent estimation of urine volume, appearance, color, pH, protein concentration, ions, glucose, and ketones. Rats were sacrificed after motor activity measurements on the day after dosing. Blood (about 1 ml) was collected via heparinized syringes and centrifuged at 10,000 rpm (1 minute) in a microcentrifuge. Plasma was analyzed for blood urine nitrogen (BUN), creatinine, alanine

aminotransferase (ALT), total protein, albumin, globulin, alkaline phosphatase, and total bilirubin.

Histopathology

After collecting blood, rats were euthanized and necropsied. A complete gross and histological necropsy evaluation was performed on all rats. Brain, liver, kidney, lung, heart, and spleen were trimmed and fixed in 10% buffered neutral formalin for routine histopathological processing. Slides were evaluated by a board certified veterinary pathologist who was “blinded” to treatment.

Cell Cultures

Both human hepatoma $HepG_2$ cells and human ovarian carcinoma NIH: OVCAR-3 cells were obtained from the American Type Culture Collection (Manassas, VA). The $HepG_2$ cell line is a common cell culture model for studying xenobiotic-induced hepatotoxicity. The NIH: OVCAR-3 cell line can develop into a solid tumor in nude mice and is considered an ideal model system to study drug resistance/therapy of human ovarian cancer. $HepG_2$ cells were maintained at 37^{o}C (5% CO2, 95% air) in DMEM/Ham’scontaining 10% fetal bovine serum and 1.5 g/L sodium bicarbonate. OVCAR-3 cells were grown at 37^{o}C (5% CO2, 95% air) in T-75 culture flasks containing RPMI culture medium supplemented with 1 mM sodium pyruvate, 0.01 mg/ml bovine insulin and 10% fetal bovine serum. Fresh medium was replaced every other day. Confluent cells were harvested with 0.25% trypsin-EDTA solution. Before treatment with nanomaterials, $HepG_2$ cells or OVCAR-3 cells were allowed to attach for 24 or 48 hours, respectively.

Biochemical Assays

Trypan Blue Exclusion Assay

In some assays, cell viability was estimated by the trypan blue exclusion assay. Viable cells exclude the dye, thus trypan blue uptake therefore suggests loss of viability. Following varying conditions, culture medium (500 µl/well) was aspirated and cells were sedimented by centrifugation (4,500 rpm for 5 min). The remaining cells on the plate were treated with 0.25% Trypsin-EDTA, triturated, and combined with original cells. Cells were then loaded on a hematocytometer slide with trypan blue at the ratio 1:1 (v/v), and the number of viable cells (unstained) and dead cells (stained) were counted in quadruplicate samples under light microscope. Cell viability was calculated as 100 × (unstained cells)/(stained +unstained cells).

LDH Assay

Lactate dehydrogenase (LDH) release was also used in some assays to evaluate viability. This colorimetric assay quantitatively measures LDH release upon cell plasma membrane damage. LDH is measured with a coupled enzymatic assay that results in the conversion of a tetrazolium salt (INT) into a red formazan product. The amount of color formed is proportional to the number of lysed cells. Following incubation of cells with nanoparticles, 50 ul of supernatant was removed to another plate followed by addition of 50 ul of substrate mix. The plate was covered with foil to protect it from light and incubated for 30 minutes at room temperature. Fifty ul of a stop solution was then

added to each well. Absorbance was measured at 490 nm using a microplate reader (Wallace 1420 Victor 2, Perkin Elmer Inc).

MTT Assay

The colorimetric MTT ((3-(4, 5-dimethylthiazol-2-yl) 2, 5-diphenyl tetrazolium bromide) test assesses cell metabolic activity based on the ability of the mitochondrial succinate-tetrazolium reductase system to convert the yellow dye (MTT) to a blue-colored formazan. Metabolic activity is proportional to the colored product formed [89]. Briefly, following incubation of cells with nanoparticles, the media was aspirated and replaced with 90 ul of serum-free media. Ten µl of an MTT stock solution (5 mg/ml) was added to each well followed by incubation for 4 hours at 37^{o}C. The supernatant was then removed and cells were lysed with 100 µl DMSO. Absorbance was recorded at 550 nm using a microplate reader.

Caspase 3/7 Assay

Caspase 3/7 activity can be used to detect induction of apoptosis. Cells were exposed to nanoparticles for varying times. The luminogenic caspase 3/7 substrate containing the tetrapeptide sequence DEVD was used for caspase 3/7 cleavage and generation of a luminescent signal following a standard protocol (Promega, Madison, WI). Briefly, 100 µl of Caspase-Glo3/7 reagent were added to each well followed by incubation at room temperature for 1 hour. The luminescence of each sample was measured using a microplate reader.

Measurement of Reactive Oxygen Species

Total reactive oxygen species (ROS) were measured using the specific molecular probe CM-H_2DCFDA (Invitrogen, Carlsbad, CA). This reagent is a cell-permeant indicator for reactive oxygen species that is non-fluorescent until acetate groups are cleaved by endogenous esterases and subsequent oxidization by ROS. The fluorescence intensity is proportional to the concentration of ROS [90]. Phosphate buffered saline containing 1% fetal bovine serum was incubated with CM-H_2DCFDA (10 µM) in 96 well plates for 30 min at 37^{o}C. A range of concentrations of nanoparticle or nanoparticle conjugates was then added, with or without UVA irradiation (0, 1.5, 3, 6 or 9 kJ/m^2). The intensity of fluorescence was determined using a microplate reader with excitation/emission at 485 nm/530 nm.

Intracellular ROS levels were monitored using CM-H_2DCFDA. After treatment, the medium was removed and replaced with serum free medium. After 30 min of incubation with 10 µM CM-H_2DCFDA, the cells were rinsed three times with PBS. Intracellular fluorescence was measured through scanning the whole well using excitation and emission wavelengths of 485 and 530 nm with a microplate reader. The values were expressed as percent of intensity in control wells.

DNA Fragmentation Assay

DNA fragmentation is a hallmark of apoptosis. HepG_2 cells were collected by centrifugation at 1,000 rpm/min for 5 minutes and the supernatant was discarded. The pellet was washed with PBS and then lysed in 500 µl lysis buffer (0.5% Triton x-100, 20 mM EDTA and 5 mM Tris pH 8) at 50^{o}C for 45 minutes.

The lysate was first extracted with 500 µl of phenol:chloroform:isoamyl alcohol (25:24:1) twice, and once with 100% chloroform. Then, 50 µl of 3 M sodium acetate were added and nucleic acids were precipitated overnight with 1 volume of ethanol. The pellet was then collected by centrifugation at 12,000 x g at 4 ^{o}C for 10 minutes. The pellet was washed with 70% ethanol, air-dried and dissolved in 100 µl of 10 mM Tris, 1 mM EDTA, pH 8 (TE) buffer. RNA was digested with RNase (0.5 µg/ml) at 56^{o}C for 2 hours. DNA concentration was quantified with a Nanodrop and then analyzed by 1.8% agarose gel electrophoresis in 45 mM Tris-borate containing 1 mM EDTA. Twenty µg of DNA was loaded into each well and separated at 1.5 v/cm for 3 hours. DNA was stained with ethidium bromide, visualized under UV light and photographed.

Western Blotting

Metallothionein protein level was determined by western blot, using β-actin as an internal standard. CdTe nanoparticle treated and untreated $HepG_2$ cells were rinsed twice with PBS (pH 7.4). Total proteins were extracted by adding 500 µl of cold lysis buffer [200 mM Tris–HCl (pH 7.4), 500 mM NaCl, 100 mM EDTA, 100 mM phenylmethanesulfonyl fluoride; 100 mM DTT, 10 mM Typsin inhibitor and 0.3% Tween-20] to the cell pellets for 30 min on ice. The mixtures were centrifuged at 10,000 x *g* for 30 min at 4℃. The cytosolic supernatant proteins were measured by the Bradford assay with bovine serum albumin (BSA) as the standard. Samples (20 µg of protein) were mixed with 5x sample buffer containing 0.3 M Tris–HCl (pH 6.8), 25% 2-mercaptoethanol, 12% sodium dodecyl sulfate (SDS), 25 mM EDTA, 20% glycerol and 0.1% bromophenol blue.

The mixtures were boiled at 95℃ for 5 min, and then loaded onto and separated in 12% SDS–polyacrylamide minigels at a constant current of 20 mA. Following electrophoresis, proteins were transferred onto a membrane (PVDF, Millipore) with transfer buffer (192 mM glycine, 25 mM Tris–HCl pH 8.9, and 20% methanol) for 2 hours at 40 volts. The membrane was then washed with Tris-buffered saline (10 mM Tris pH 8.0, 150 mM NaCl) containing 0.05% Tween-20 (TBST) and blocked in TBST containing 5% non-fat dried milk. The membrane was further incubated at 4℃ for 2 hours with specific antibodies MT (1:2000) and β-actin (1:5000). After hybridization with primary antibodies, the membrane was washed with TBST three times, incubated with horseradish peroxidase-labeled secondary antibody for 60 min at room temperature, and then washed with TBST (3x). Detection was performed with ECL^{TM} (Enhanced Chemiluminescence) western blotting reagents (Amersham Pharmacia Biotech).

Real time RT-PCR

The expression of metallothionein RNA was quantified by real time reverse transcription–polymerase chain reaction (Real-time RT-PCR) analysis. Beta-actin mRNA was used as an internal standard control. $HepG_2$ cells were plated into 100 mm tissue culture dishes and allowed to attach for 24 hours. Various concentrations of CdTe nanoparticles were added to the cells for 24 hours. RNA was extracted with TRIzol RNA isolation kit (Invitrogen) according to manufacturer's instructions. Total RNA (1 µg) was treated with 1 µl DNase I (Invitrogen) at 37^0C for 30 minutes to remove contaminating genomic DNA. The sense and antisense sequence primers used were: MT II: 5´-CCG ACT CTA

GCC GCC TCT T-3´, 5´-GTG GAA GTC GCG TTC TTT ACA- 3´; β-actin: 5'-AGAAAATCTGGCACCACACC-3'; 5'-GGGGTGTTGAAGGTCTCAAA-3'. For each sample, 1 µg of RNA was reverse-transcribed. cDNA was synthesized using 200 ng random primers (Invitrogen), 200U superscript II reverse transcriptase and 0.25 mM dNTP mix. Reaction mixtures were then treated with *E. coli* RNase H at 37^0C for 20 minutes to remove RNA. The 20-µl real-time PCR amplification mixture contained 2 µl of template cDNA, 1 µl of primer (10 uM) mix, and 10 µl of 2x SYBR master mix (Applied Biosystems). Reactions were conducted at 50℃ for 2 min and 95℃ for 10 min, foll owed by 40 cycles at 95℃ for 15 s and 60℃ for 1 min. Relative gene expression was calculated as 2–CT (threshold cycle) values. Real-time PCR was performed on an ABI PRISM 7500 (Applied Biosystems).

Microscopy

Tissue Distribution using TEM

In the tissue distribution studies, samples of livers and brains were collected 24 hours after treatment. Tissues (approximately 1 gram) were digested and Cd levels measured using atomic absorption spectrometry. The limit of detection was 0.01ppm.

Liver and brain were collected and cut into 1 mm cubes and immediately immersion fixed in buffered (pH 7.0-7.2) 2% glutaraldehyde. The samples were dehydrated in ethanol and embedded in 100% embedding medium. Thick and thin sections specimen were cute using an ultramicrotome (Sorvall MT-6000). Tissue samples were evaluated using transmission electron microscopy (JEOL

JEM-2100) either without prior staining or following staining with Au/Pb, and analyzed bywith X-ray scanning.

Subcellular Distribution using Confocal Microscopy

$HepG_2$ cells or OVCAR-3 cells were exposed to CdTe nanoparticles (10 µM) or ZnO-MTAP nanoparticle conjugates (10 µM) for 1hour or 24 hours and examined using confocal microscopy. Cover slips with attached cells were washed 5 times to remove non-incorporated particles and sealed onto glass slides. Images were captured with a Leica TCS Sp2 microscope. The excitation wavelength was 480 nm and emission wavelengths were 640 nm, 570 nm and 530 nm for CdTe-red, -yellow or -green nanoparticles, respectively. With ZnO-MTAP conjugates, the excitation wavelength was 360 nm and the emission wavelength was 630 nm. CdTe nanoparticle localization was analyzed using Scion image software (Frederick, Md., USA).

Hoechst /PI Staining

Hoechst 33342 and propidium iodide (both from Invitrogen) were used to distinguish apoptotic and necrotic cells, based on nuclear morphology. Hoechst 33342 is a cell-permeant dye, whereas propidium iodide (PI) does not penetrate the plasma membrane of viable cells. Condensation of the nucleus stained with Hoechst 33342 is considered an indicator of apoptosis. In contrast, PI uptake indicates necrotic cells or cells in late-stage apoptosis, i.e., following loss of membrane integrity. OVCAR-3 cells were seeded into 24 well plates (1×10^5 cells/ml, 500 µl/well) and exposed to both ZnO nanoparticle conjugates (10 µM) and UVA (9 kJ/m^2). Thirty minutes before the end of the incubation period (3, 12

or 24 hours), Hoechst 33342 stain (5 µM, 30 min) or PI (2 µM, 15 min) was added. Cells were washed three times with phosphate buffered saline. Nuclear morphology was evaluated using a Nikon Eclipse TE 2000-u fluorescence microscope using UV filter for Hoechst 33342 staining and a G filter for PI staining.

Photodynamic Therapy of Nanoparticle Conjugates

Ultraviolet Irradiation Treatment

Irradiation of cells was conducted in a laminar flow hood. To determine the uniform area of UVA light irradiation, a Newport power meter (Model 1815-C) with an OD3 attenuator (883-UV, S/N 3995) was calibrated to 365 nm with low power. To study the effect of UVA on ovarian cancer cells, 96-well plates containing 1 x 10^4 cells/well were placed under the UVA lamp (Fisher Biotech FBUVLS-80) for 30, 60, 90 or 120 min (0.50 mW/cm^2), corresponding to an irradiation dose of 9, 18, 27 or 36 kJ/m^2. For dark conditions, plates were completely covered with aluminum foil to block any light entry into the plates and kept under the hood for the same time/conditions as cells being exposed to UVA. All plates were placed back into the cell culture incubator. Twenty hours after terminating irradiation, metabolic function was evaluated using the MTT assay.

In Vitro Photodynamic Therapy

OVACAR-3 cells (1x 10^5 cells/ml, 100 µl/well) were treated with ZnO-MTAP conjugates (0, 1 or 10 µM) for four hours and then washed three times with phosphate buffered saline. Cells were then exposed to either dark or UVA (9

kJ/m^2) as described above. Twenty hours later, cell viability was measured using the MTT assay.

Development of Ovarian Tumor Model in vivo

A long term goal of this project was to evaluate phototoxicity of the nanoparticle conjugates *in vivo*. We therefore attempted to develop a solid tumor model of the NIH:OVCAR-3 cells. Female BALB/c nude mice (5 weeks of age) were obtained from Charles River Laboratories (Wilmington, MA). The animals were housed in a micro-isolator cage and given standard autoclaved pellets and water. The mice were allowed to acclimate for 1 week and then treated with OVCAR-3 cells or vehicle. OVCAR-3 cells were cultured in T-75 culture flasks at 37^{o}C in a humidified atmosphere with RPMI 1640 culture medium supplemented with 10% fetal bovine serum (FBS). Cells at the seventh passage were harvested with 0.25% trypsin for 3 min and then resuspended in culture medium without FBS. After 3 washes with phosphate buffered saline (centrifugation at 1,000 rpm for 5 min), cells were stained with Trypan blue and viability counted with a hemocytometer.

To optimize the dose of cells for tumor growth, 8 mice were randomly divided into four groups and inoculated with 0, 1 x 10^7 (low dose)' 1.8 x 10^7 (medium dose) or 2.4 x10^7 (high dose) cells in 300 ul of PBS. Control mice were injected (i.p.) with 300 µl of PBS. Mice were observed every other day for 10 weeks for changes in body weight and general cage-side behavior/appearance. Tumor size was measured using a slide caliper and calculated using the standard formula: volume= length x (width) ^{2}/2.

At the end of the 10 week observation period, mice were euthanized with carbon dioxide. Blood was collected through cardiac puncture into a heparinized microtube. The tumor mass was demarcated and weighed. Organs and tissues, including the tumor, were removed and fixed in 10% formalin, and histopathological examination was conducted to evaluate tumor morphology.

Statistical Analysis

In MTT assays, LDH assays, caspase assays and real-time PCR analyses, data were reported as mean ± standard error (SE) based on at least triplicate observations from three independent experiments. Statistical significance was determined by one-way analysis of variance (ANOVA) followed by Dunnett's multiple comparison test. Graded responses were evaluated using MANOVA. Phototoxicity and oxidative stress data were analyzed with student's t-test. In all cases, $p<0.05$ was considered statistically significant. All statistical analyses were performed using the Graph Pad Prism® software package (version 4.0).

CHAPTER 3

RESULTS

Toxicity of CdTe NPs *in vitro* and *in vivo*

Cytotoxicity of CdTe Nanoparticles

We used the trypan blue, LDH and MTT assays to evaluate cell viability in $HepG_2$ cells following exposure to CdTe nanoparticles. The time-dependent effects of CdTe nanoparticles on cell viability is shown in Figure 4. Concentration-dependent effects are shown in Figure 5, Figure 6, and Figure 7. Moreover, Figure 7 shows that CdTe-Red (6 nm), CdTe-Yellow (4 nm), and CdTe-Green (2 nm) nanoparticles may elicit size dependent cytotoxicity. The IC_{50} (concentration causing 50% reduction in cell viability measured by the MTT assay) values of the three nanoparticles were 19.1, 4.8, 3.0 uM for CdTe-Red, CdTe-Yellow and CdTe-Green particles, respectively. One possibility for cytotoxicity in these preparations was that free cadmium may have been in the samples as prepared. We therefore purified a sample of CdTe-red using methanol extraction, and then compared the cytotoxicity of the sample as prepared with purified sample. Figure 8 shows that, although the purified nanoparticles still exhibited similar photophysical properties with the “as

prepared" sample, their cytotoxicity was markedly reduced. These data suggest that the CdTe nanoparticles as prepared may indeed have some free cadmium or other contaminant that is cytotoxic.

One potential problem in the use of any nanomaterial is aggregation. We examined the time-dependent aggregation of CdTe-Red nanoparticles using microscopy. There was apparent aggregation/agglomeration of the CdTe-Red nanoparticles over time (Figure 9). The aggregation of the particles appeared to be primarily extracellular, however, as similar aggregates were noted when culture medium containing the nanoparticles was incubated in the absence of any cells (data not shown).

Traditionally, water soluble CdTe nanoparticles have been synthesized under inert conditions. Figure 10 shows that synthesis in either air or nitrogen had little apparent effect on the the cytototoxicity of CdTe-red particles. With the smaller CdTe-yellow and CdTe-green nanoparticles, there was a suggestion of lesser cytotoxicity with nanoparticles synthesized in nitrogen relative to those synthesized in air (Figure 11, 12). It must be stressed, however, that there were statistical differences in cytotoxic potential between CdTe nanoparticles prepared in either air or nitrogen.

Evaluation of Mode of Cytotoxicity Induced by CdTe Nanoparticles

There are two basic types of cell death, apoptosis and necrosis. To determine the cytotoxic mechanism of CdTe nanoparticles in $HepG_2$ cells, we used three methods to evaluate apoptosis. Figure 13 shows that nuclear condensation, an indicator of apoptosis, was elicited after 24 hours incubation

with CdTe-red particles, but not at an earlier timepoint (i.e., 4 hours). Similarly, caspase 3/7 activity was induced by CdTe-red particles in a dose- and time-dependent manner (Figure 14 and 15). In addition, the hallmark of apoptosis, DNA fragmentation, appeared after 48 hours exposure to CdTe-Red nanoparticles (Figure 16).

Effect of CdTe Nanoparticles on Metallothionein Expression

Our previous study showed that free cadmium may at least partially contribute to the cytotoxicity of CdTe nanoparticles. It is well known that cadmium could induce the expression of metallothionein in $HepG_2$ cells. Therefore, we evaluated metallothionein expression in $HepG_2$ cells exposed to CdTe nanoparticles. Figure 17 shows metallothionein mRNA level was increased by CdTe nanoparticle at lower concentrations (0.2 to 1 μM) but was reduced at higher concentrations (20 - 100 μM). Figure 18 shows that metallothionein protein levels were decreased in CdTe treated cells.

Effect of the Size of CdTe Nanoparticles on Their Subcellular Distribution

As mentioned before, the size of CdTe nanoparticles can play an important role in their optical properties and cytotoxic potential. Size may be also critical in cellular transport processes as they interacted with biological membranes and channels. Therefore, we evaluated subcellular distribution of different sized CdTe nanoparticles. Figure 19 shows apparent size- and time-dependent distribution of CdTe nanoparticles in $HepG_2$ cells. After 1 hour incubation, CdTe-Red (6 nm) and CdTe-Yellow (4 nm) particles appeared mainly bound to the plasma membrane while CdTe-Green (2 nm) appeared to be visible

in the cytosol. After 24 hours exposure, however, CdTe-Red (6 nm) and CdTe-Yellow (4 nm) appeared to be more diffusely located within the cytoplasm while CdTe-Green (2 nm) appeared to distribute into the nucleus.

Acute Toxicity of CdTe-Red Nanoparticles in Rats

Twenty-four hours after treatment, there was a slight but significant reduction in body weight of CdTe-Red treated rats relative to controls (Figure 20). Core body temperature twenty-four hours after treatment was unaffected (data not shown).

Rats were graded before treatment and at 0.5, 1, 2, 4 and 24 hours after treatment for functional signs of toxicity as described in methods. No overt signs of toxicity were observed in either nanoparticle-treated or control groups at any timepoint (data not shown). Figures 21 and 22 show motor activity was affected by systemic CdTe-Red nanoparticle treatment. Rearing scores were significantly reduced in nanoparticle-treated rats compared to vehicle controls from 0-2 hours after dosing, and there was a non-significant trend towards reduced ambulation. Interestingly, both rearing and ambulation counts were significantly increased 24 hours following nanoparticle exposure. There were no treatment-related differences in any blood-borne clinical endpoints measured (Table 1). Similarly, there were no significant effects of nanoparticle treatment on urinary indicators including protein, glucose, ketones, bilirubin or blood cells in the urine (Table 2). Following routine histopathological analysis, there were no treatment-related histopathological changes in any tissues (data not shown). Figure 23 shows a

microthrombosis of a small venule in lung tissue noted in both control and treated rats, and thus not related to treatment.

Tissue Distribution of CdTe Nanoparticles

CdTe nanoparticles appear to distribute within cells in a size-dependent manner (Figure 19). Evaluation of the distribution of nanoparticles *in vivo* will help determine whether the particles are effectively distributed and accumulate in tissues, or effectively blocked from entry into some tissues and eventually eliminated. Figures 24 and 25 show that cadmium accumulated in both brain and liver tissue in a dose–dependent manner 24 hours after CdTe nanoparticle treatment. Figure 26 and 27 shows liver imaged with TEM. Figure 26A is a sample of CdTe nanoparticles alone, while Figure 26B is a section of unstained liver following treatment with CdTe-Red *in vivo.* As noted in this figure, particles of about the same size as CdTe-Red can be seen in the unstained tissue. In contrast, no such particles were noted in tissues that had been stained for TEM (uranyl acetate and lead, Figure 27). X-ray scanning analysis in Figure 27 confirmed both Cd and Te in the particles, possibly an indicator that intact CdTe nanoparticles had entered the tissues following systemic administration.

Cytotoxicity of Fullerene Aggregates (nC_{60})

Effect of Synthetic Methods and Size on Cytotoxicity of nC_{60}

It has been reported that the chemical and physical properties of nC_{60} aggregates made through either solvent exchange or by extended stirring in water may have different properties [91].We therefore compared the cytotoxicity of nC_{60} aggregates synthesized through four different methods, i.e., solvent

extraction using tetrahydrofuran (THF), solvent extract using toluene/tetrahydrofuran/acetone (TTA), by sonication with toluene extraction (SON), or by prolonged stirring in aqueous media alone (AQ). Figure 28 shows that synthetic conditions may indeed influence the cytotoxicity of fullerene aggregates. Aggregates synthesized by extraction with TTA were more potent at reducing cell viability than aggregates prepared by the other three methods. Interestingly, when all samples were extensively evaporated to attempt to any residual organic solvent, the aggregates prepared by the AQ method now showed higher cytotoxicity (Figure 29), Cytotoxicity of the AQ sample was also concentration–dependent (Figure 30).

As noted before, oxidative stress has been hypothesized to contribute to the cytotoxicity of a variety of nanomaterials. We therefore evaluated whether nC_{60} could produce ROS. Figure 32 shows that nC_{60} produced ROS in a time-dependent manner. The cytotoxic potential of three different sized nC_{60} (119, 145 and 152 nm) were studied. Figure 31 shows that, within this size range, there is no apparent size-related difference in cytotoxicity. .

Phototoxicity of ZnO-MTAP NP Conjugates

Reactive Oxygen Species Generation by Nanoparticle Conjugates

The principle of self-lighting photodynamic therapy was described in the previous chapter. The generation of ROS under irradiation is the key aspect of this approach. We thus evaluated if ZnO-MTAP conjugates could generate ROS under dark or UVA irradiation conditions. Figure 33 shows ROS production by different concentrations of ZnO-MTAP conjugates under dark and light

conditions. Essentially, no evidence of ROS generation was noted with ZnO-MTAP conjugates under dark conditions, while concentration- and irradiation dose-dependent effects were noted with UVA irradiation.

Cellular Localization of ZnO-MTAP Conjugates

We investigated if the conjugates could be taken up by ovarian cancer cells. OVCAR-3 cells were incubated with ZnO-MTAP conjugates (10 µM for 4 hours), and then evaluated with confocal microscopy. Figure 34 shows that the conjugates appeared to be primarily localized within the cytosol at this time.

In vitro Photodynamic Therapy

Since the nanoparticle conjugates were taken up into the cells, we proposed to see if the drug could be activated under irradiation. Therefore, we compared the phototoxicity and dark toxicity of ZnO-MTAP in OVCAR-3 cells. Figures 35 and 36 show OVCAR-3 cell viability was affected by increasing concentrations of ZnO-MTAP conjugates (24 hour exposure) or increasing intensity of UVA irradiation. Using the MTT assay, no effects on cell viability were seen with 0.1-10 µM ZnO-MTAP conjugates, whereas cell viability was reduced with the highest UVA intensity (36 kJ/m^2). Phototoxicity of the ZnO-MTAP conjugates was then evaluated using a subtoxic UV exposure. As shown in Figure 37, neither UVA (9 kJ/m^2) nor ZnO-MTAP nanoparticle conjugates alone affected cell viability. When cells were exposed to both conjugates and UVA, however, concentration-dependent reduction in viability was noted, with maximal (92%) reduction in viability noted with UVA illumination and the higher concentration (10 µM) of ZnO-MTAP conjugates.

Cell Death Induced by ZnO-MTAP Conjugates and UVA Irradiation

Figure 38 shows that caspase 3/7 was activated from 3-6 hr after exposure to ZnO-MTAP conjugates and UVA irradiation, but caspases decreased at later time-points. Figure 39 shows Hoechst 33342 and propidium iodide staining from 3-24 hr after similar exposure conditions. Nuclear condensation with Hoechst 33342 staining at 3 hr after treatment suggested an early apoptotic response. Uptake of propidium iodide at 12 hours after treatment suggested a delayed necrotic response. At the latest timepoint examined (24 hr), most of the cells showed propidium iodide uptake indicating widespread membrane damage and likely necrosis.

Table 3 shows the different types of nanoparticle conjugates that were evaluated for cytotoxic potency under dark and irradiated conditions, using either UVA, X-ray or laser. Of all, only the ZnO-MTAP showed any potential for photoactivation.

Development of Ovarian Tumor in Nude Mice

As described before, nude mice were injected with vehicle or one of three concentrations of NIH OVCAR-3 cells. There were no gross functional changes in any mice throughout the 10-week period. Mice that developed tumors moved somewhat slower than mice that had no obvious tumor. However, two mice in the high dose group (s.c.) showed apparent ascites accumulation at the sixth week after inoculation, and exhibited a solid mass on the seventh week. In the eighth week after inoculation, another high-dose mouse, one medium dose, and one low dose mouse exhibited a tumor on the abdomen near the site of injection. One

medium dose mouse (i.p) began to develop ascites during the eighth week post-inoculation.

Tumor size was measured using a slide caliper. Solid tumors developed in 6 of 8 inoculated mice, including 5 in subcutaneous tissue and 1 in the peritoneal cavity. Body weight changes were not dose-related (Figure 40), while the rate of tumor growth was dose-related, i.e., the higher dose led to more extensive tumor growth (Figure 41-42). The neoplasm developing in subcutaneous tissue was attached to the external body wall and did not invade the peritoneal cavity (Figure 43). However, the neoplasm that developed in the peritoneal cavity showed "milky" fluid in the abdomen (Figure 44). Figures 45-47 demonstrate the microscopic morphology of subcutaneous and intraperitoneal tumors in H&E stained tissue sections. The neoplastic cells in subcutaneous and intraperitoneal tissues were evaluated via light microscopy, confirming proliferation of neoplastic cells at the different inoculation sites. Peritoneal fluid from the mouse with "milky" ascites was cytologically evaluated to confirm the presence of neoplastic cells (Figure 48). All mice were alive at 10 weeks post-inoculation at each of the three doses. These results suggest that the solid tumor model can be easily developed for any future studies.

Effect of Pre-exposure of N-acetyl Cysteine or Diethyl Maleate on Toxic Potential of CdTe, nC_{60}, and ZnO-MTAP/UVA

Oxidative stress can be modulated by conditions which either increase or decrease antioxidant status. For example, oxidative stress mediated toxicity can be reduced by supplementing intracellular antioxidant levels, e.g., by increasing

glutathione levels. On the other hand, ROS-mediated cytotoxicity can be increased by prior reduction of intracellular antioxidant levels, e.g., by reducing glutathione levels by preexposure to diethyl maleate. $HepG_2$ or OVCAR-3 cells were pre-treated with the glutathione precursor N-acetyl-cysteine (NAC, 5 mM) to evaluate the effects on cytotoxicity of various nanoparticles/ conjugates. In parallel studies, cells were pre-treated with the glutathione depletor diethyl maleate (DEM, 200 uM). H_2O_2 was used as a positive control. Metabolic activity (MTT assay), intracellular ROS levels and caspase 3/7 activity were measured to determine the influence of antioxidant status on cellular response.

H_2O_2 can induce oxidative stress [92]. We therefore used H_2O_2 as a positive control in studies evaluating oxidative stress of nanomaterials. Figures 49 and 50 show that the cytotoxicity of H_2O_2 was reduced by NAC pre-exposure, and increased by DEM pre-exposure. Figures 51 and 52 show that ROS generation by H_2O_2 was partially blocked by pre-exposure to NAC (5 mM, 2 hr), and was increased by DEM pre-exposure (200 µM). NAC alone had no effect on ROS levels while ROS was increased by pre-exposure to DEM (200 uM). These data suggest that ROS elicited by H_2O_2 can be influenced in a predictable manner by modulating antioxidant by these approaches.

Several studies suggest cadmium can induce oxidative stress [93, 94]. Therefore, we used Cd $(NO_3)_2$ as positive control in evaluations of the potential for CdTe nanoparticles to induce oxidative stress. Figure 53 shows that cytotoxicity of both CdTe and Cd $(NO_3)_2$ was greatly reduced by NAC (5 mM, 2hr) pre-exposure. Free cadmium was more potent than CdTe nanoparticles.

The differing dose-related effects on metabolic activity induced by CdTe versus Cd $(NO_3)_2$ suggest that cadmium containing nanoparticles and free cadmium may elicit cytotoxicity via different mechanisms. The reduced toxicity in cells preexposed to NAC could be be due to: 1) NAC reduced oxidative stress by increasing glutathione levels in the cells or 2) NAC directly adsorbed free cadmium released from the nanoparticles. Figure 54 shows that the cytotoxicity of CdTe and Cd $(NO3)_2$ was partially increased by pre-exposure to DEM (200 uM, 2 hr). However, no additive effect was noted. Furthermore, Figure 55 shows that ROS levels were not increased by exposure to CdTe (100 µM, 30 minutes), with or without pre-exposure to NAC. ROS levels increased with pre-exposure to DEM (200 uM) and CdTe exposure, but no additive effects were noted. These data suggested that oxidative stress may not be a prominent mechanism in CdTe-induced toxicity. The apoptosis induced by CdTe nanoparticles noted above may therefore be elicited through other molecular pathways.

As noted before some investigators have reported that nC_{60}-THF aggregates can elicit toxicity through lipid peroxidation [38]. We therefore evaluated if the toxicity of nC_{60}-AQ was mediated through oxidative stress. Figure 56 shows that cytotoxicity of nC_{60}-AQ (3,300 ppm) was partially reduced by NAC (5 mM, 2 hr), but was unaffected by DEM (200 uM, 2 hr). Figure 57 shows that ROS generated by nC_{60}-AQ aggregates was reduced by NAC pre-exposure, yet markedly increased by DEM pre-exposure. These data suggest that oxidative stress elicited by nC_{60}-AQ aggregates can be affected by modulating antioxidant levels in the cells. Figure 58 shows that caspase 3/7 was not activated in $HepG_2$

cells after exposure to nC_{60}-AQ. Toxicity may therefore not be mediated through caspase 3/7-induced apoptosis.

Oxidative stress can also be an important mechanism in photodynamic therapy [95, 96]. We evaluated if oxidative stress was important in the cytotoxicity of ZnO-MTAP conjugates exposed to UVA. Figure 59 shows that ROS generated by ZnO-MTAP/UVA were almost completely blocked by pre-exposure to NAC (5 mM), and increased by DEM pre-exposure (200 µM). The effect of DEM appeared additive in nature (i.e., about 50% increase over ZnO-MTAP/UVA alone, and about a 50% increase with DEM alone). Thus, these data suggest that ROS elicited by ZnO-MTAP/UVA can be affected in a predictable manner by modulating antioxidant levels in the cells. Figure 60 shows that the cytotoxicity of ZnO-MTAP/UVA was also substantially reduced by NAC pre-exposure, but relatively unaffected by DEM pre-exposure. Further studies need to evaluate the effects of DEM on lower concentrations of ZnO-MTAP. Figure 61 shows that NAC (5 mM) markedly blocked the increase in caspase 3/7 activity elicited by ZnO-MTAP/UVA, suggesting that apoptosis was at least partially mediated by oxidative mechanisms. However, while both ZnO-MTAP/UVA and DEM alone increased caspase 3/7 activity, there was no apparent additive effect (i.e., the combination exposure showed the least increase in caspase).

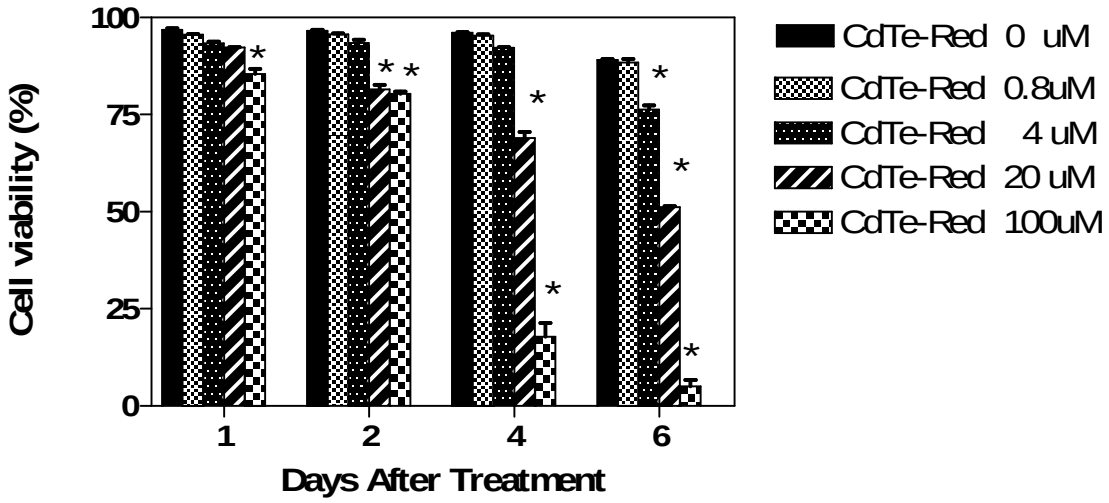

Figure 5. Effect of CdTe-Red nanoparticles on $HepG_2$ cell viability. $HepG_2$ cells were treated at different concentrations of nanoparticles for 1 day, 2days, 4days, and 6 days. At the end of the incubation period, cell viability was determined by the Trypan Blue Assay. The data were expressed as mean ± standard deviation (SD) for triplicate samples from three independent experiments. An asterisk indicates a statistically significant difference compared to control ($p<0.05$).

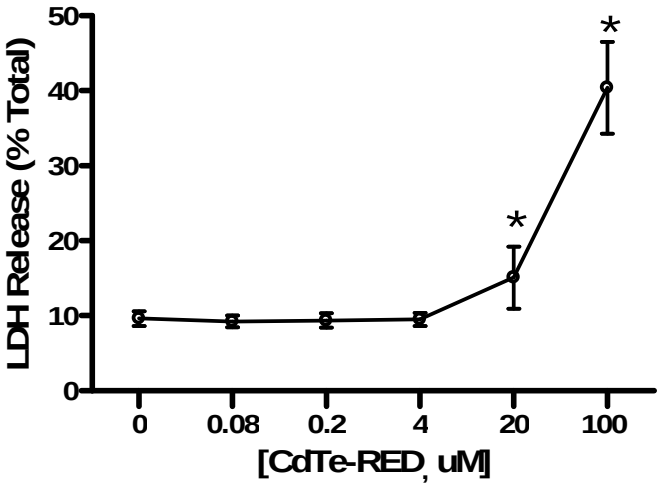

Figure 6. Effect of CdTe-Red nanoparticles on LDH release in $HepG_2$ cells. $HepG_2$ cells were treated with different concentrations of nanoparticles for 24 hours. Cell viability was determined by the LDH release assay. The data were expressed as mean ± standard deviation (SD) for triplicate samples from three independent experiments. An asterisk indicates a statistically significant difference compared to control ($p<0.05$).

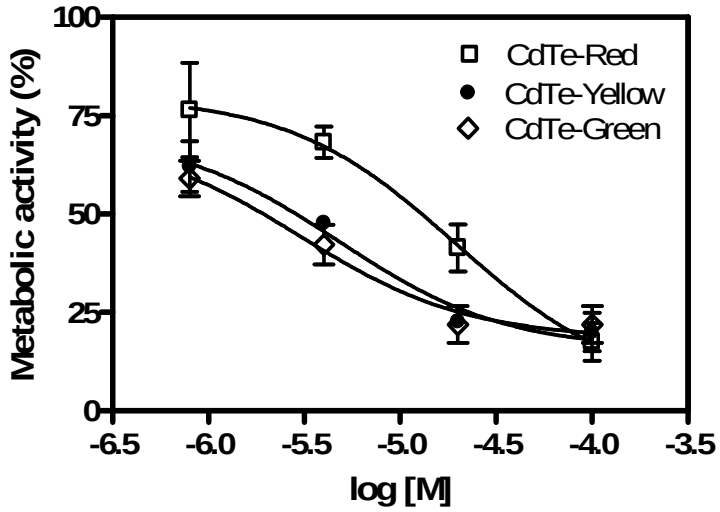

Figure 7. Effects of concentration and size of CdTe nanoparticles on $HepG_2$ cell viability. $HepG_2$ cells were cultured with different sized (CdTe-Red, CdTe-Yellow and CdTe-Green; 6 nm, 4 nm, and 2 nm) nanoparticles for 48 hours. The MTT assay was conducted at the end of the treatment period. The OD value of the control cells (nanoparticle-free medium) was taken as 1.0 and proportionate change in OD as affected by CdTe exposure was determined. The data were expressed as mean ± standard error (SE) using quadruplicate observations from three independent experiments.

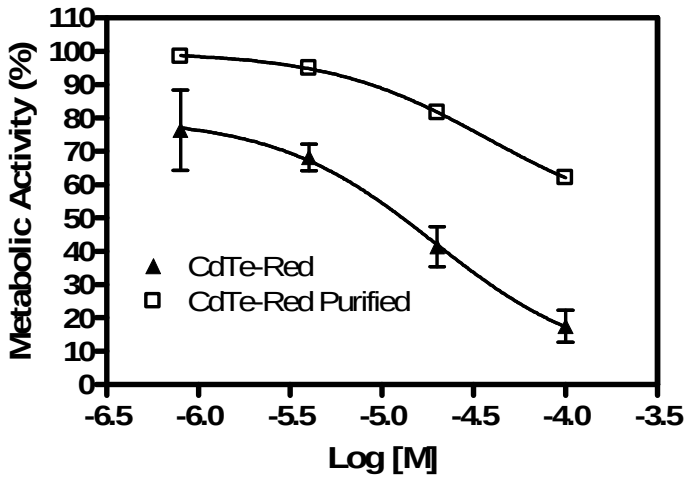

Figure 8. Effects of CdTe-Red nanoparticles as prepared and following partial purification on $HepG_2$ metabolic activity. $HepG_2$ cells were cultured with different concentrations of CdTe-Red nanoparticles for 48 hours. The MTT assay was then conducted to evaluate metabolic viability. The OD value of the control cells (nanoparticle-free medium) was taken as 1.0 and proportionate change in OD as affected by CdTe-Red exposure was determined. The data were expressed as mean ± standard error (SE) for quadruplicate observations from three independent experiments.

.

.

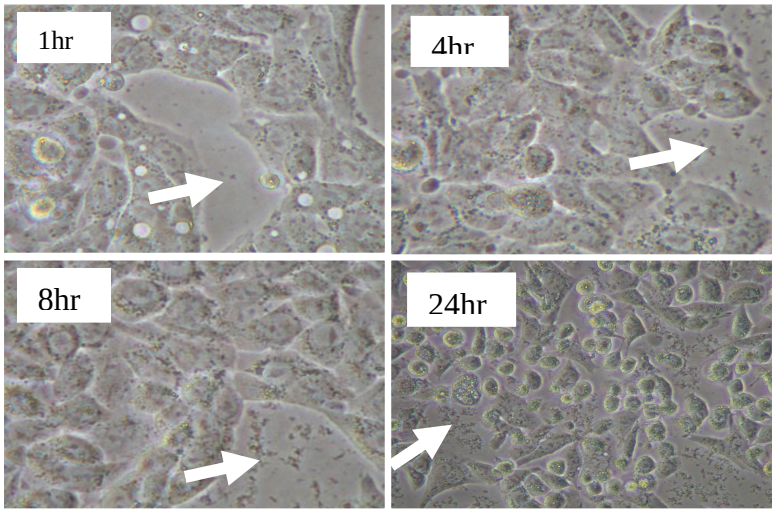

Figure 9. Aggregation of CdTe-Red nanoparticles. $HepG_2$ cells were cultured with CdTe-Red nanoparticles for up to 24 hours. Images were captured using a Nikon Eclipse TS100 light microscope and Nikon Coolpix 995 digital camera at 1, 4, 8 and 24 hour of exposure (magnification 400×). Arrows point to apparent time-dependent aggregation of the nanoparticles

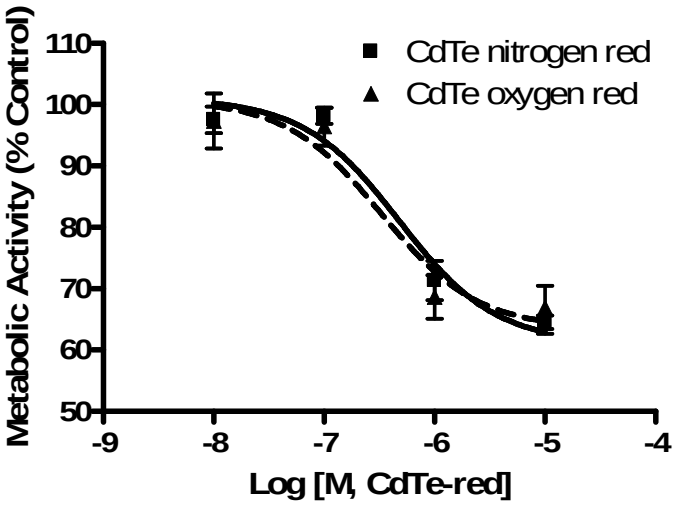

Figure 10. Effect of synthetic conditions (nitrogen or air atmosphere) on cytotoxicity of CdTe nanoparticles. $HepG_2$ cells were cultured with a range of concentrations of CdTe-Red nanoparticles (6 nm) made in either nitrogen (N_2) or air. Nanoparticles were added to cells at concentrations of 0, 10^{-8}, 10^{-7}, 10^{-6} and 10^{-5} M for 24 hours prior to evaluating cell viability by the MTT assay. Cell viability was evaluated as affected by exposure to CdTe-red nanoparticles synthesized in either N_2 or air. Values represent mean ± SEM of three different experiments with quadruplicates for each concentration of particles.

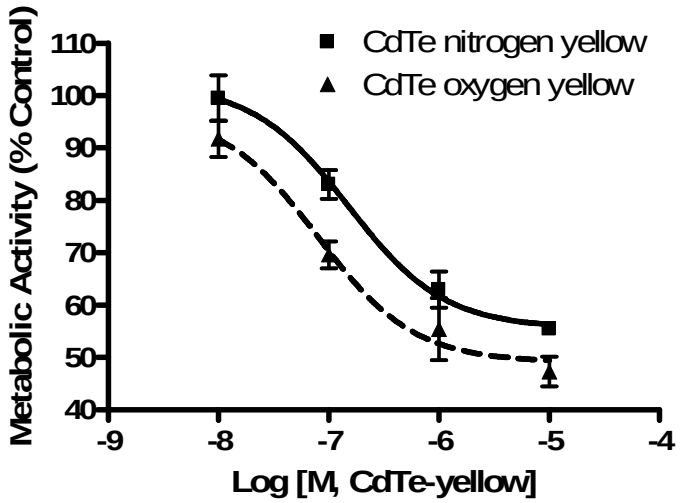

Figure 11. Effect of synthetic conditions (nitrogen or air atmosphere) on cytotoxicity of CdTe nanoparticles. $HepG_2$ cells were cultured with a range of concentrations of CdTe-yellow nanoparticles (4 nm) made in either nitrogen (N_2) or air. Nanoparticles were added to cells at concentrations of 0, 10^{-8}, 10^{-7}, 10^{-6} and 10^{-5} M for 24 hours prior to evaluating cell viability by the MTT assay. Cell viability was evaluated as affected by exposure to CdTe-yellow nanoparticles synthesized in either N_2 or air. Values represent mean ± SEM of three different experiments with quadruplicates for each concentration of particles.

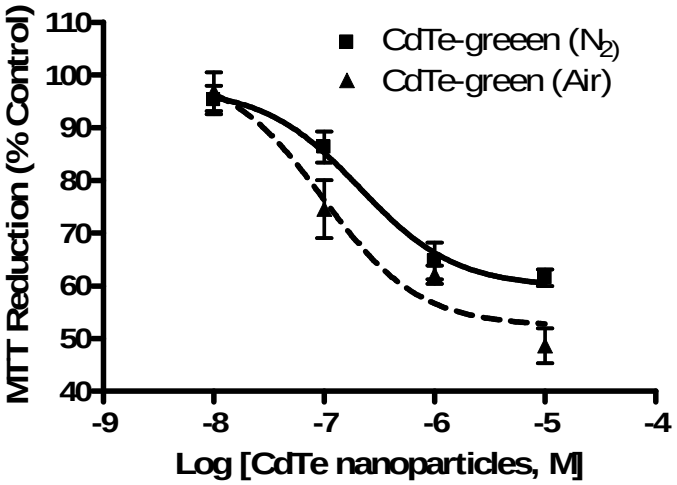

Figure 12. Effect of synthetic conditions (nitrogen or air atmosphere) on cytotoxicity of CdTe nanoparticles. $HepG_2$ cells were cultured with a range of concentrations of CdTe-green nanoparticles (2 nm) made in either nitrogen (N_2) or air. Nanoparticles were added to cells at concentrations of 0, 10^{-8}, 10^{-7}, 10^{-6} and 10^{-5} M for 24 hours prior to evaluating cell viability by the MTT assay. Cell viability was evaluated as affected by exposure to CdTe-green nanoparticles synthesized in either N_2 or air. Values represent mean ± SEM of three different experiments with quadruplicates for each concentration of particles.

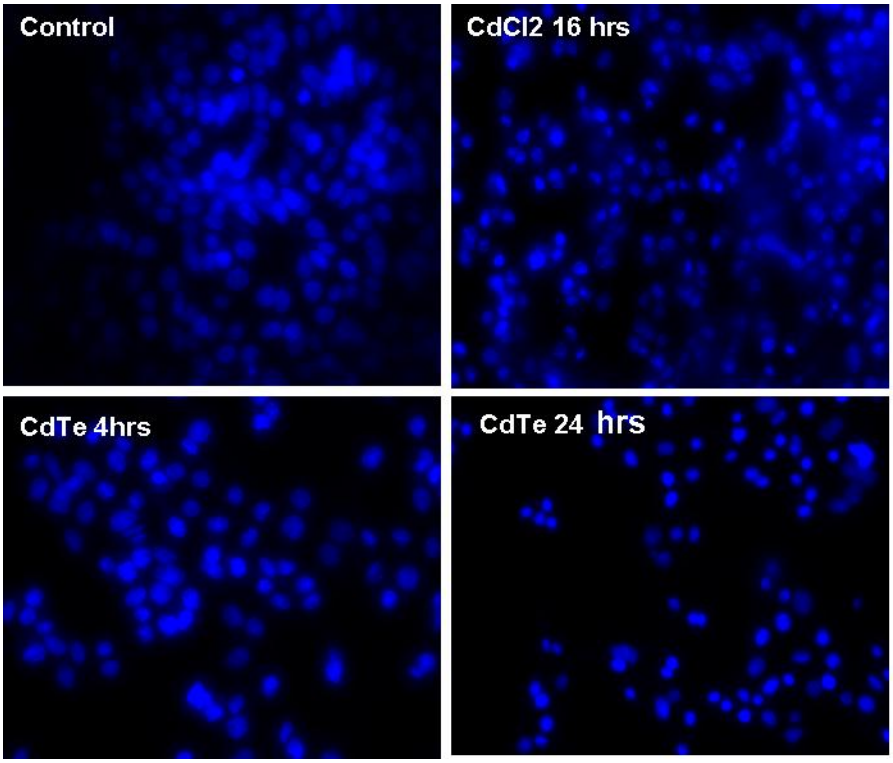

Figure 13. Effect of CdTe-Red on nuclear morphology of $HepG_2$ cells. $HepG_2$ cells (1×10^5 cells/ml) were incubated with CdTe-Red nanoparticles for 4 or 24 hours. At the specified time after incubation, cells were stained using the nuclear dye Hoechst 33342 (10 µM, 30 minutes). Nuclear morphology was observed using an inverted fluorescence microscope (20 x). $CdCl_2$ was used as a positive control.

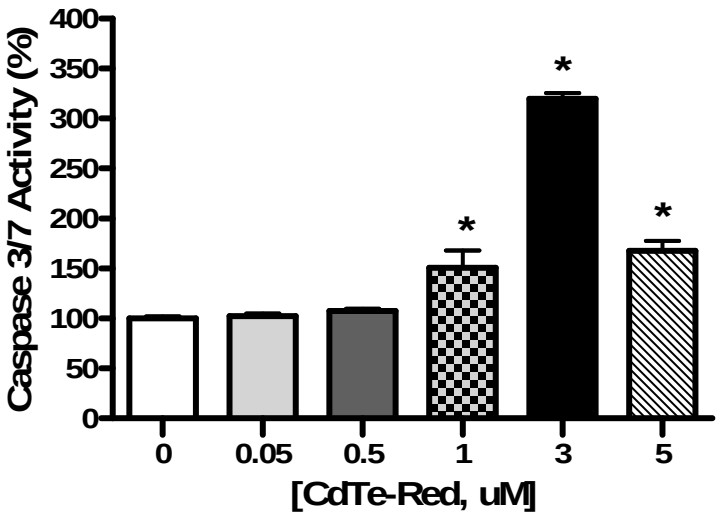

Figure 14. Activation of caspase 3/7 by CdTe-Red nanoparticles is concentration-dependent**.** $HepG_2$ cells were exposed to the indicated concentrations of CdTe-Red nanoparticles for 24 hours. The luminogenic caspase 3/7 substrate containing the tetrapeptide sequence DEVD was used for detecting activity. Caspase 3/7 activity of control cells was set to 100%. An asterick indicates a significant difference compared to control ($p < 0.05$).

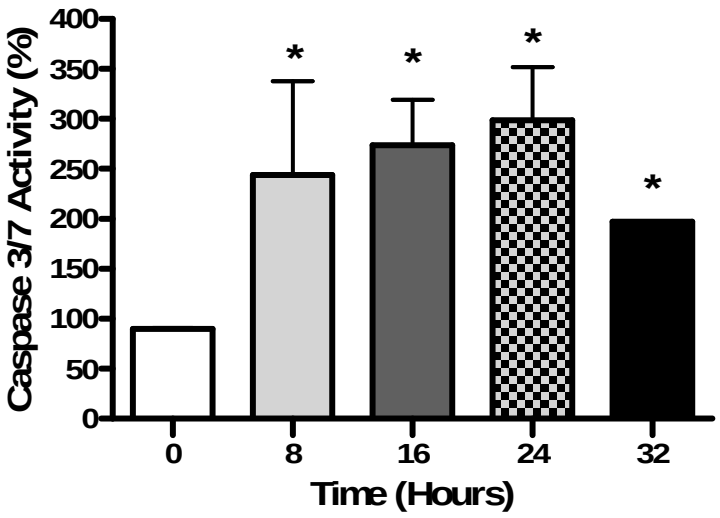

Figure 15. Activation of caspase 3/7 by CdTe-Red nanoparticles is time-dependent. Cells were exposed to CdTe-red nanoparticles (3 µM) for varying times (0, 8, 16, 24, 32 hours). The luminogenic caspase 3/7 substrate containing the tetrapeptide sequence DEVD was used to detect activity. Caspase 3/7 activity of control cells was set to 100%.

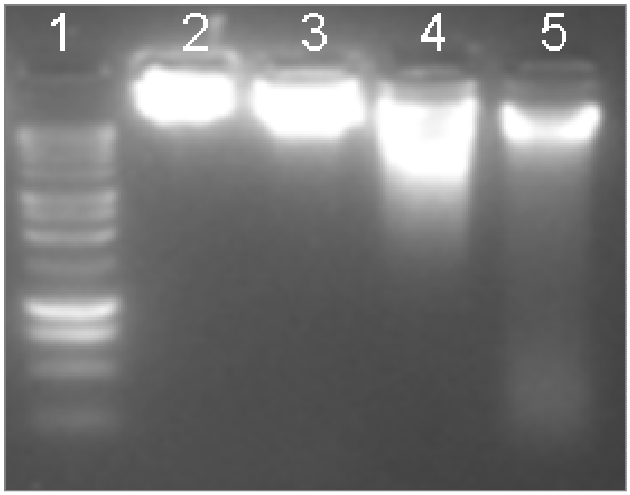

Figure 16. DNA fragmentation appears at 48 hours incubation with CdTe-Red nanoparticles. $HepG_2$ cells (5 X 10^6) were incubated with 0, 4, 20, or 100 µM (lane 2 to 5) of CdTe -red nanoparticle (6 nm) for 48 hours. Lane 1 contains the molecular weight marker. Attached and unattached cells were harvested and DNA was resuspended in 0.5% triton-X 100 cell lysis buffer for 45 minutes. DNA in the supernatant fraction after centrifugation was extracted twice with phenol/chloroform/isoamyl (25:24:1, v/v/v) and once with chloroform, followed by precipitation with ethanol. RNA in the pellet was digested with RNAase for 2 hour at 56^{o}C. Equal amounts of DNA were separated in agarose gel (1.8%) for 3 hour at 1.5 V/cm. DNA in the gel was visualized under UV light after staining with ethidium bromide (0.5 mg/ml).

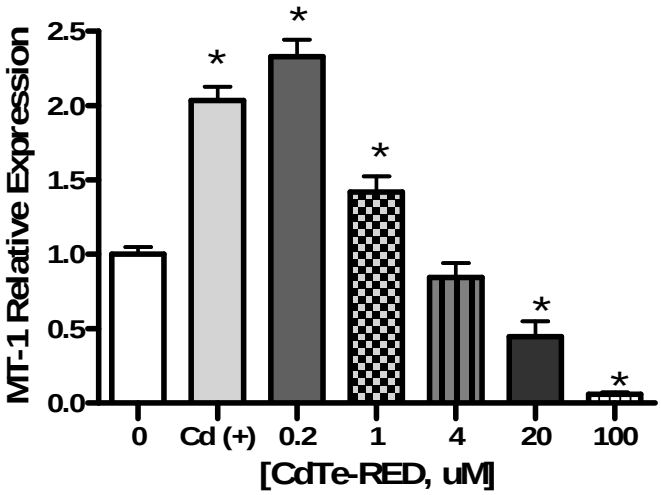

Figure 17. Real time RT-PCR analysis of metallothionein mRNA in HepG2 cells treated with CdTe-Red nanoparticles. HepG2 cells (2 X 10^5/ml) were exposed to one of a range of concentrations of CdTe-Red nanoparticles for 24 hours. Cadmium nitrate (0.2 µM) was used as a positive control. Expression of metallothionein (MT) mRNA was analyzed by real time RT-PCR. Beta-actin was used as an internal control. The ratio of RT-PCR product of MT-I to beta-actin was calculated. The data were expressed as mean ± standard error (SE) for quadruplicate observations from three independent experiments.

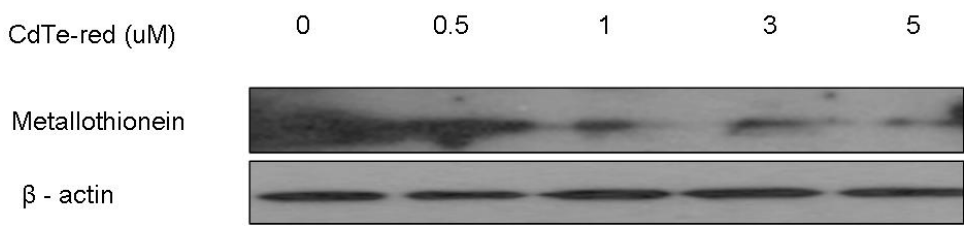

Figure 18. Inhibition of metallothionein levels in $HepG_2$ cells by CdTe-red nanoparticles. Cells were exposed to CdTe-red nanoparticles for 24 hours. Total protein was isolated and concentration was estimated using the Bradford assay. Twenty µg of total protein was denatured and separated on a 12% polyacryamide gel. After the protein was transferred to the membrane, the membrane was further incubated for 2 hours with specific antibodies for MT (1: 2000) and β-actin (1:5000). Then the membrane was incubated with horseradish perooxidase-labelled secondary antibody for 1 hour. Detection was performed with ECL™ chemiluminescence western blotting reagents (Amersham Pharmacia Biotech, UK). β-actin, the house keeping gene, was used as an internal control.

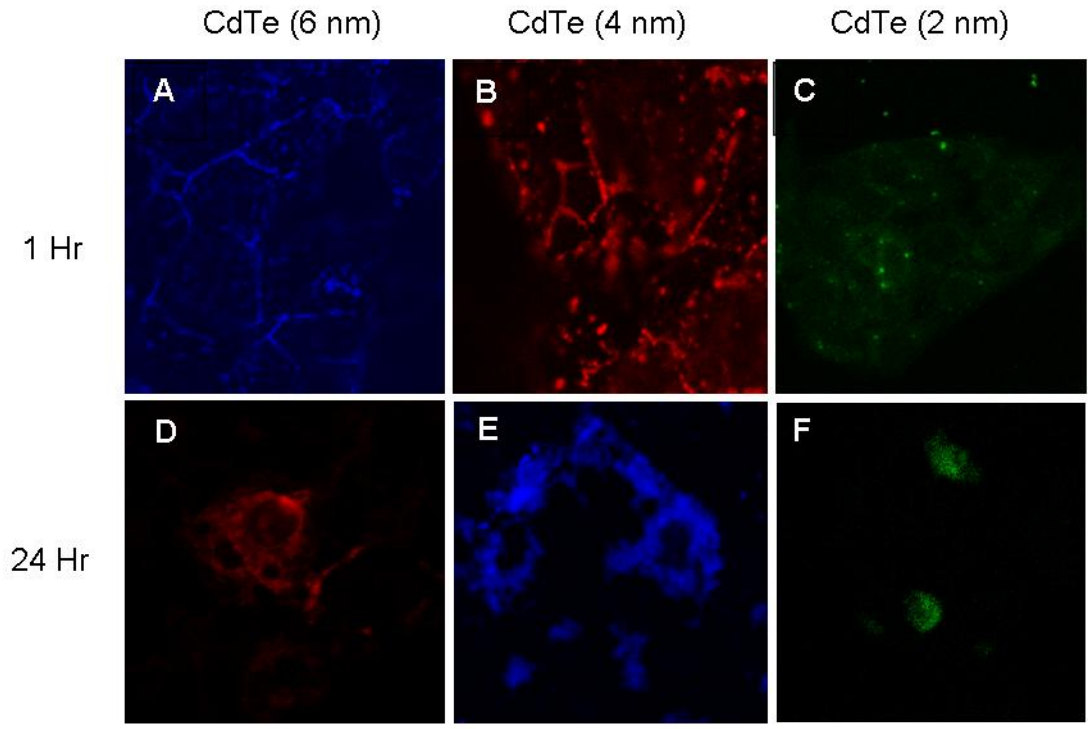

Figure 19. Size- and time- dependent CdTe nanoparticle distribution in $HepG_2$ cells. Cells were imaged with 400 nm excitation and A) 630 nm B) 570 nm C) 530 nm emission following 1 hour exposure to A) 6 nm (CdTe-Red), B) 4 nm (CdTe-Yellow), or C) 2 nm (CdTe-Green)nanoparticles. Imaging was also conducted after 24 hours exposure D-F)..

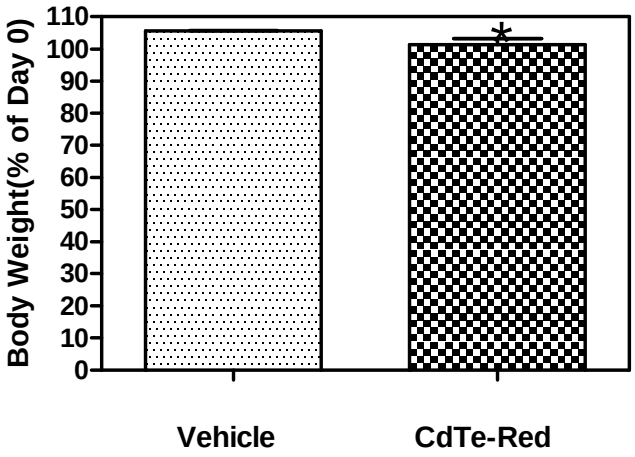

Figure 20. Body weight changes at 24 hours after systemic injection of CdTe-Red nanoparticles (2 mM, 1 ml/kg) or vehicle. Body weight at Day 0 was just prior to injection. The data were expressed as mean ± standard error (SE) (n= 8/treatment group). An asterisk indicates a statistically significant difference compared to control ($p<0.05$).

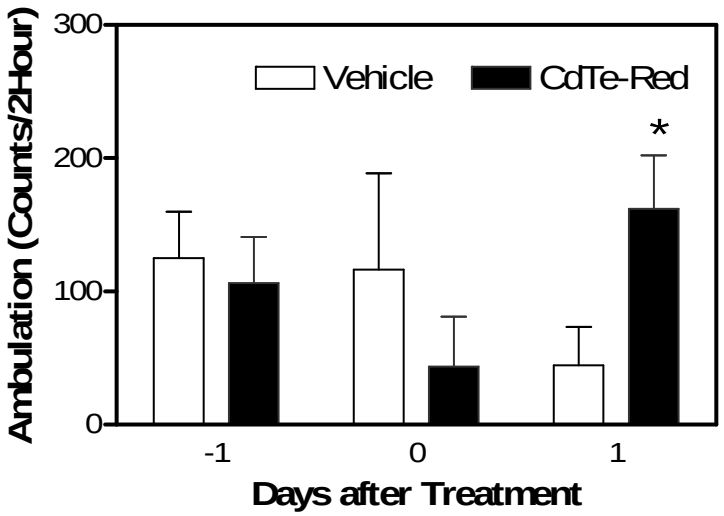

Figure 21. Effect of systemic administration of CdTe-Red nanoparticles on horizontal motor activity (ambulation) in rats. Ambulation was measured for two hours on the day before dosing (Day-1), on the day of treatment (Day 0), and on the day after dosing (Day 1). Photobeam interruptions were recorded as described in Methods. The data are expressed as mean ± standard error (n=8/treatment group). An asterisk indicates a statistically significant difference compared to vehicle-treated controls ($p < 0.05$).

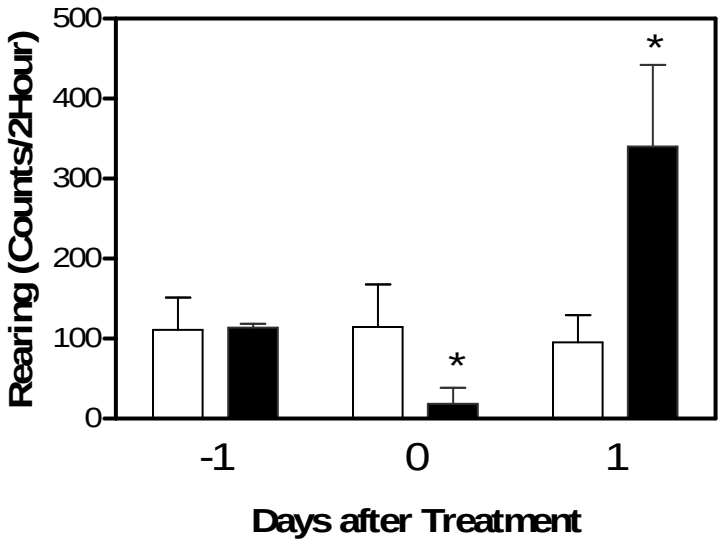

Figure 22. Effect of systemic administration of CdTe-Red nanoparticles on vertical motor activity (rearing) in rats. Rearing was measured for two hours on the day before dosing (Day -1), on the day of treatment (Day 0), and on the day after dosing (Day 1). Photobeam interruptions were recorded as described in Methods. The data are expressed as mean ± standard error (n= 8/treatment group). An asterisk indicates a statistically significant difference compared to vehicle-treated controls ($p < 0.05$).

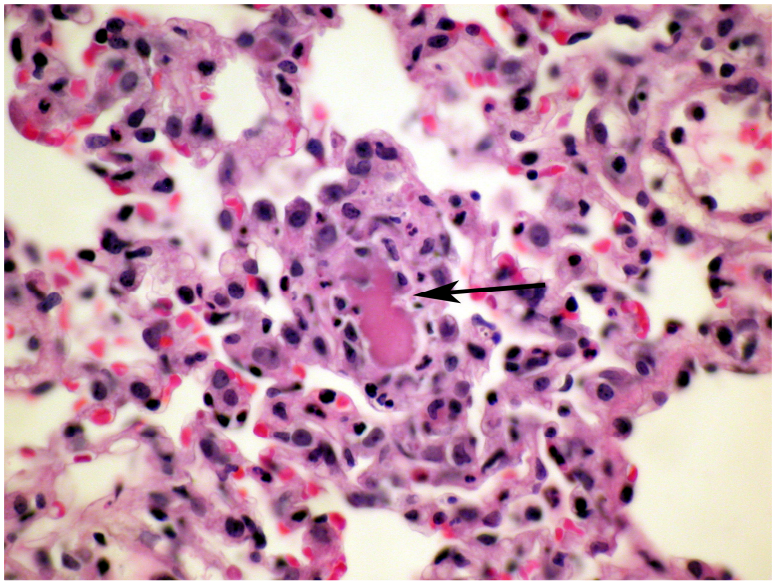

Figure 23. Microthrombosis of a small venule in the lung of a treated rat 24 hours after intravenous injection CdTe nanoparticle. This type of lesion was also seen in control animals and was therefore not treatment related.

TABLE 1 Effect of systemic CdTe-Red nanoparticles on plasma chemistry parameters in rats[1]

Parameter	Unit	Vehicle	CdTe-Red
Alanine amino transferase	IU/L	70.4 ± 3.3*	91.4 ± 8.9
Total Bilirubin	mg/dL	0.14 ± 0.04	0.13 ± 0.02
Alkaline phosphatase	IU/L	460 ± 11	456 ± 31
Total Protein	g/dL	5.7 ± 0.4	5.5 ± 0.2
Albumin	g/dL	2.74 ± 0.04	2.78 ± 0.06
Globulin	g/dL	2.9 ± 0.4	2.8 ± 0.2
Albumin/Globulin ratio		0.99 ± 0.08	1.04 ± 0.07
Cholesterol	mg/dL	94.9 ± 1.8	93.1 ± 3.5
BUN	mg/dL	19.6 ± 2.3	17.0 ± 0.9
Creatinine	mg/dL	0.50 ± 0.00	0.50 ± 0.00
BUN/Creatinine ratio		43.6 ± 5.4	34.0 ± 1.8
Phosphorus	mg/dL	11.7 ± 0.3	11.7 ± 0.2
Calcium	mg/dL	11.2 ± 0.2	10.7 ± 0.2
Glucose	mg/dL	144 ± 2.0	145.6 ± 4.3
Sodium	mEq/L	139.9 ± 0.2	139.6 ± 0.6
Potassium	mEq/L	6.4 ± 0.1	6.7 ± 0.1
Na/K ratio		22.0 ± 0.6	20.7 ± 0.3
Chloride	mEq/L	96.1 ±1.1	94.9 ±0.9
CPK	IU/L	9436 ± 1441	9097 ± 1703

[1] Male Sprague Dawley rats were treated intravenously (*via* tail vein) with CdTe-Red nanoparticles (2 µmol/lkg) or vehicle as described in Methods. Whole blood was collected with heparinized needles on the day after dosing and plasma collected for measurement of clinical indicators.

* Values represent mean ± SE of eight rats/group

TABLE 2. Effect of systemic CdTe-Red nanoparticles on urinalysis parameters in rats[1]

Parameter	Vehicle	CdTe
Specific Gravity	1.04 ± 0.01*	1.04 ± 0.01
pH	7.6 ± 0.3	7.3 ± 0.3

[1] Male Sprague Dawley rats were treated as in Methods and following 2-hour motor activity measurements, transferred to metabolic cages for approximately 6-7 hours for the collection of urine. Glucose, bilirubin, occult blood and protein were not detected in any samples.

* Values represent mean ± SE of eight rats/group.

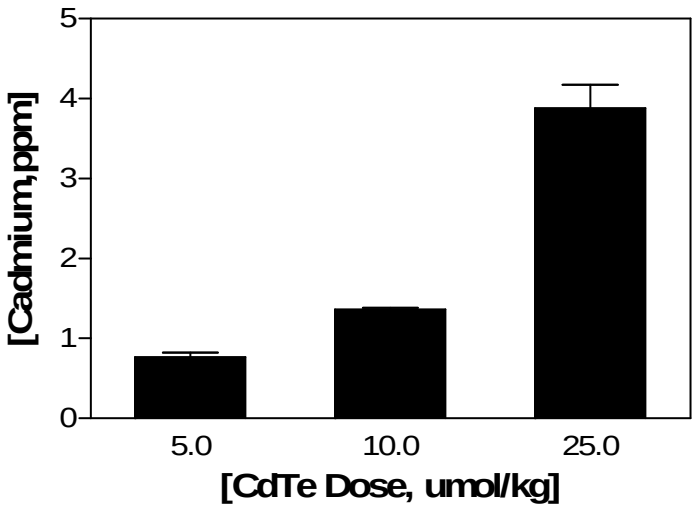

Figure 24. Accumulation of Cd in liver following systemic treatment with CdTe-Red nanoparticles. Livers were collected 24 hours after treatment. Tissues were digested and Cd content measured by atomic absorption spectrophotometry. The Cd level in the vehicle-only group was below 0.01 ppm (n=6/treatment group).

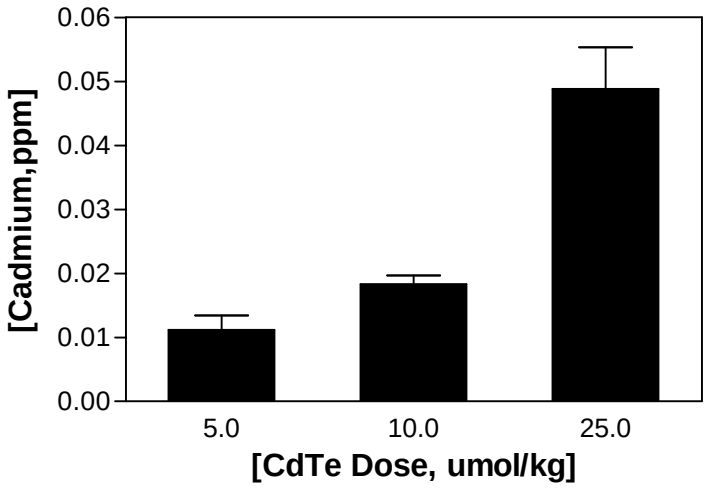

Figure 25. Accumulation of Cd in brain following systemic treatment with CdTe-Red nanoparticles. Brains were collected 24 hours after treatment. Tissues were digested and the Cd level was measured by atomic absorption spectrophotometry. The Cd level in the vehicle-only group was below 0.01 ppm (n=6/treatment group).

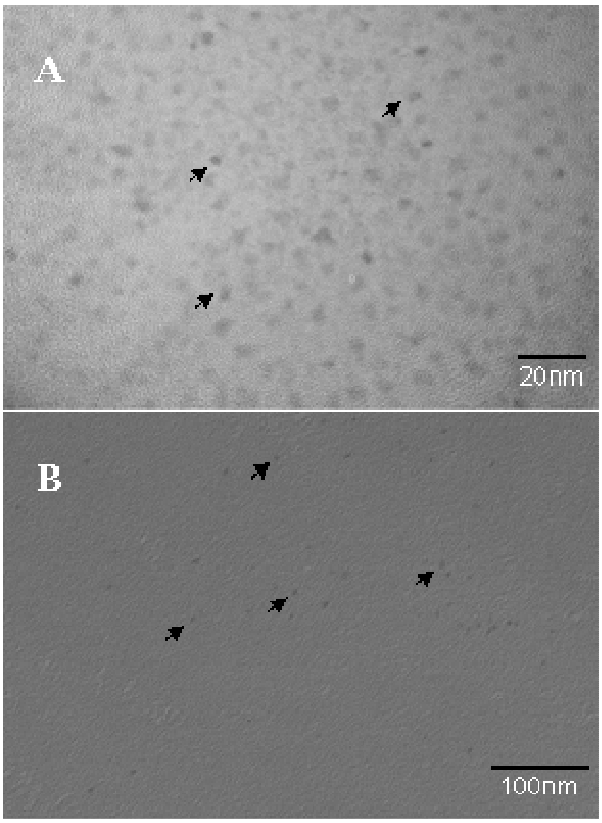

Figure 26. CdTe nanoparticles in liver after intravenous administration. Livers from rats treated with CdTe-Red (25 µmol/kg) were collected and fixed in 2% glutaraldehyde 24 hours after treatment. (A) CdTe-Red was deposited on a TEM grid and observed via transmission electron microscopy. The black sheres appear to be individual CdTe nanoparticles, with diameters around 6 nm (scale bar, 20 nm). (B) Livers samples were embedded and processed without staining and evaluated by transmission electron microscopy (scale bar, 100 nm). Note similarly appearing particles of approximately 6 nm diameter.

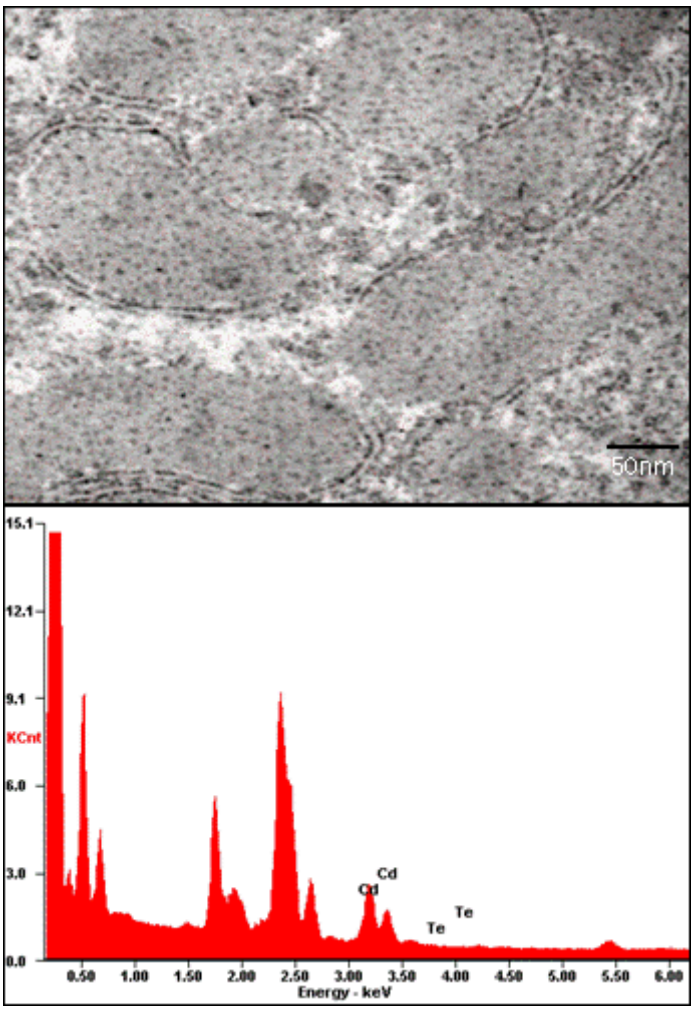

Figure 27. CdTe nanoparticle detection in liver after systemic administration. Liver was collected and fixed in 2% glutaraldehyde 24 hours after administration of CdTe-Red as described above. In this case, tissues were embedded and stained with uranyl acetate and lead. The image was captured with JEM 2100 transmission electron microscope and elemental analysis conducted using X-ray scanning (scale bar, 50 nm). Note presence of both Cd and Te.

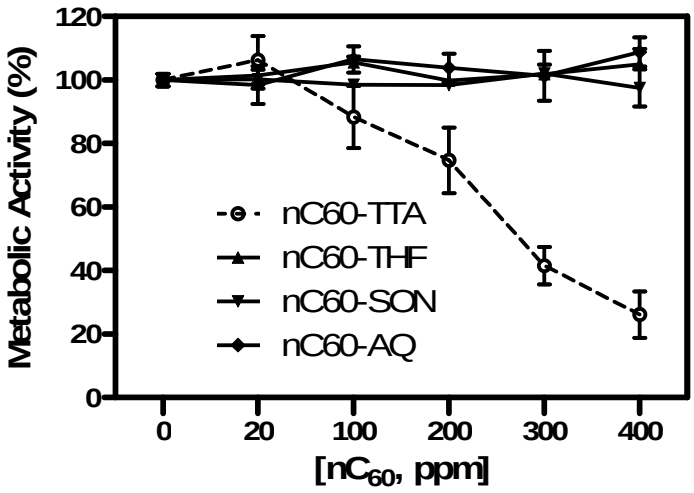

Figure 28. Effect of synthetic method (THF, TTA, SON, and AQ) on the cytotoxicity of nC_{60} in $HepG_2$ cells. $HepG_2$ cells were cultured with a range of concentrations of nC_{60} made by the THF, TTA, sonication, or AQ method. nC_{60} were added to cells at concentrations of 0, 20, 100, 200, 300, 400 ppm for 24 hours prior to evaluating cell viability by the MTT assay. The data were expressed as mean ± standard error (SE) using quadruplicate observations from three independent experiments

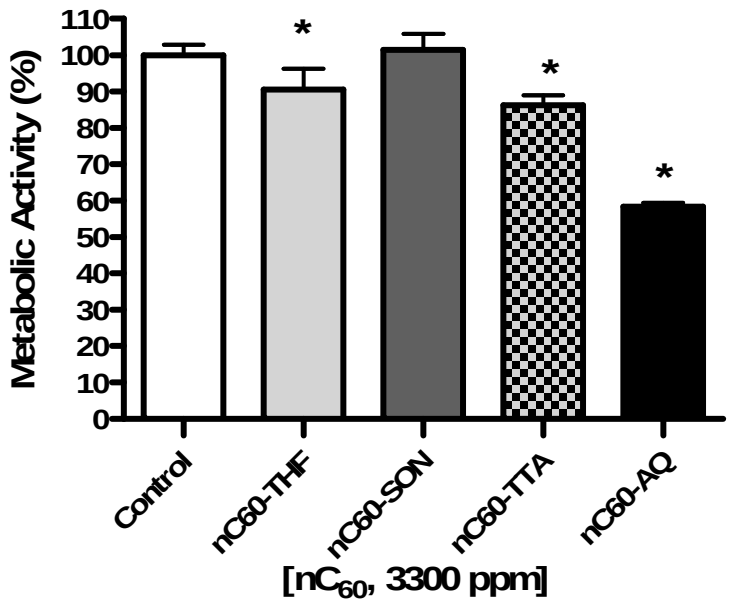

Figure 29. Effect of purified nC_{60} prepared by different methods on cell viability in HepG2 cells. nC_{60} prepared using THF, TTA, Sonication, or AQ methods were evaporated extensively using flash evaporation and stored at room temperature for one month. $HepG_2$ cells were cultured with these samples at a final concentration of 3,300 ppm for 24 hours, prior to evaluating cell viability . The data were expressed as mean ± standard error (SE) using quadruplicate observations from three independent experiments.

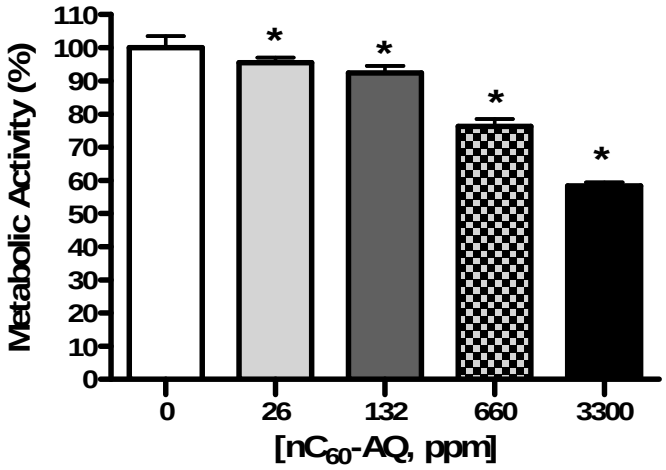

Figure 30. Effect of different concentrations of nC_{60}-AQ on $HepG_2$ cell viability. nC_{60}–AQ aggregates were added to cells at concentrations of 0, 26, 132, 660, and 3300 ppm for 24 hours prior to evaluating cell viability by the MTT assay. The data were expressed as mean ± standard error (SE) using quadruplicate observations from three independent experiments

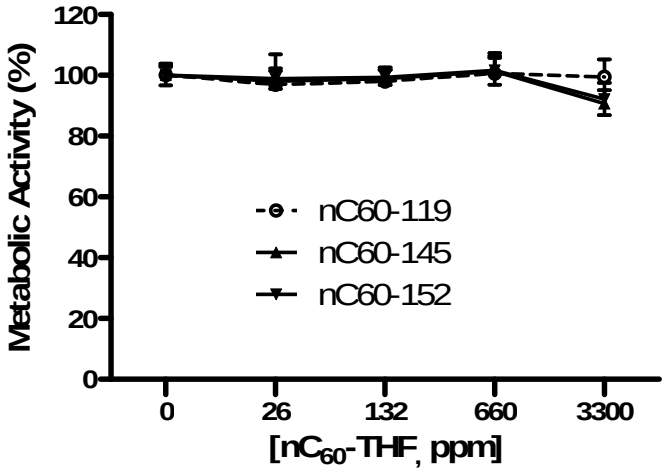

Figure 31. Effects of concentration and size of nC_{60}-THF aggregates on $HepG_2$ cell viability. Human $HepG_2$ cells were cultured with a range of concentrations of three size of nC_{60} made using THF method. nC_{60} aggregates were added to cells at concentrations of 0, 26, 132, 660, and 3300 ppm for 24 hours prior to evaluating cell viability by the MTT assay. The data were expressed as mean ± standard error (SE) using quadruplicate observations from three independent experiments

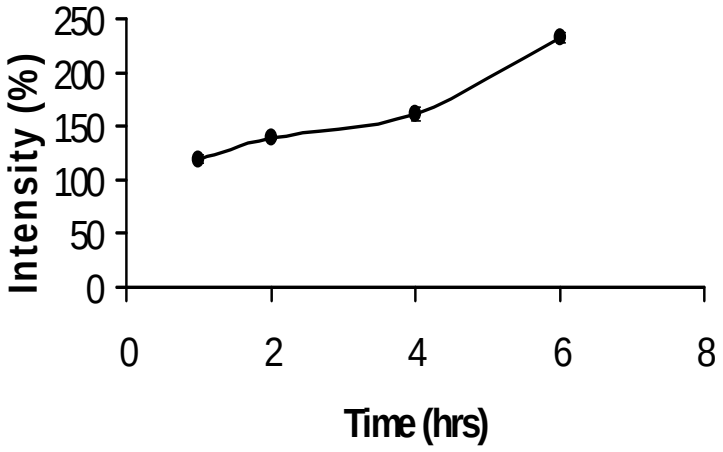

Figure 32. Effect of nC_{60}-AQ (3300 ppm) on ROS in $HepG_2$ cells. $HepG_2$ cells were cultured with 3,300 ppm of nC_{60}-AQ for 1, 2, 4, or 6 hours. The cells were washed with PBS twice and then incubated CM-H_2DCFDA (10 µM) in phosphate buffered saline for 30 min. Following washing with PBS, the fluorescence intensity (indicator of ROS) of the cells was determined using a microplate reader with excitation/emission at 485 nm/530 nm. The data were expressed as mean ± standard error (SE) using quadruplicate observations.

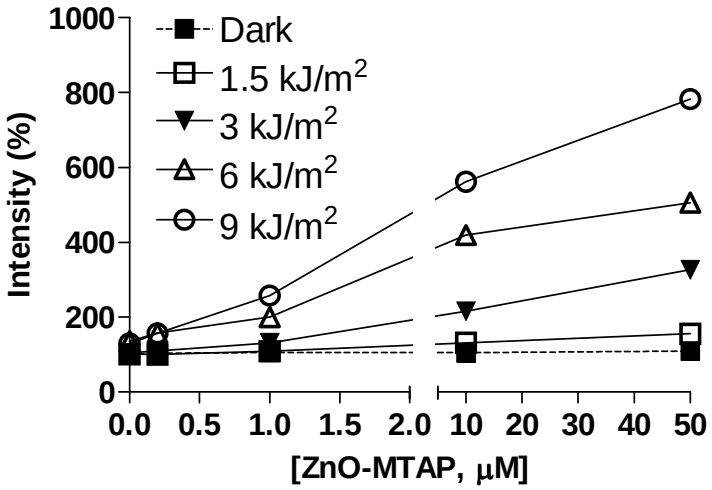

Figure 33. Reactive oxygen species generation by ZnO-MTAP conjugates in the presence or absence of UVA light. CM-H_2DCFDA (5 μM) was dissolved in PBS containing 1% serum and ZnO-MTAP conjugates (0-50 μM) were added 15 minutes later. The conjugates were then exposed to 0, 1.5, 3, 6 or 9 kJ/m^2 UVA. The fluorescence intensity (indicate ROS level) of the cells was determined using a microplate reader with excitation/emission at 485 nm/530 nm.

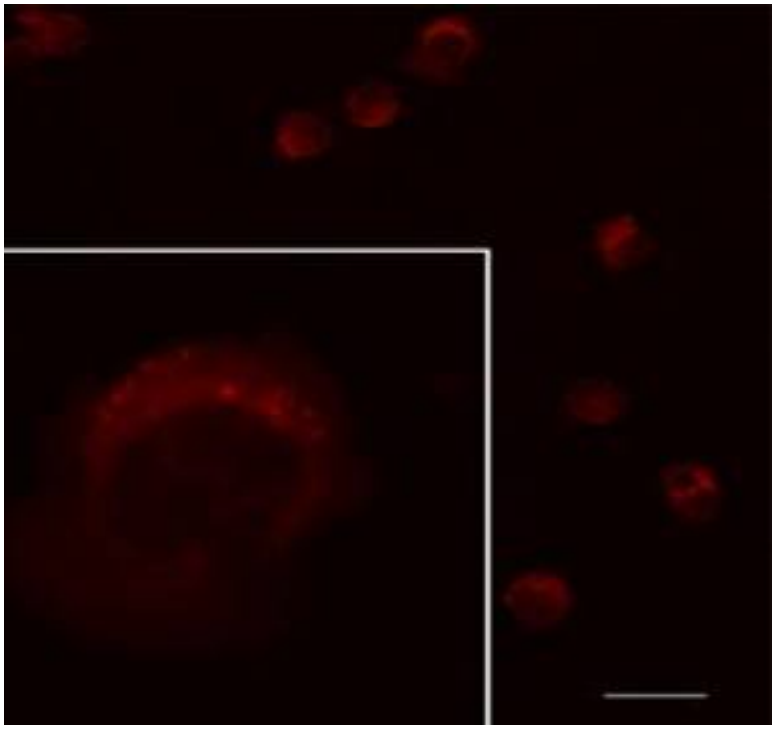

Figure 34. Uptake of ZnO-MTAP nanoparticle conjugates *in vitro*. NIH: OVCAR-3 cells were cultured with medium containing ZnO-MTAP conjugates (10 µM) for 4 hours on a cover slip in 10-cm cell culture plates. Cover slips with attached cells were then washed three times to remove free conjugates and sealed on a slide with clear nail polish. Images were captured with confocal laser scanning Leica TCS Sp2 microscope with excitation at 360 nm and emission at 630 nm. Conjugate localization was analyzed using Scion image software (bar = 150 µm). Inset image (higher magnification) shows nanoparticle conjugates localized in the cytoplasm.

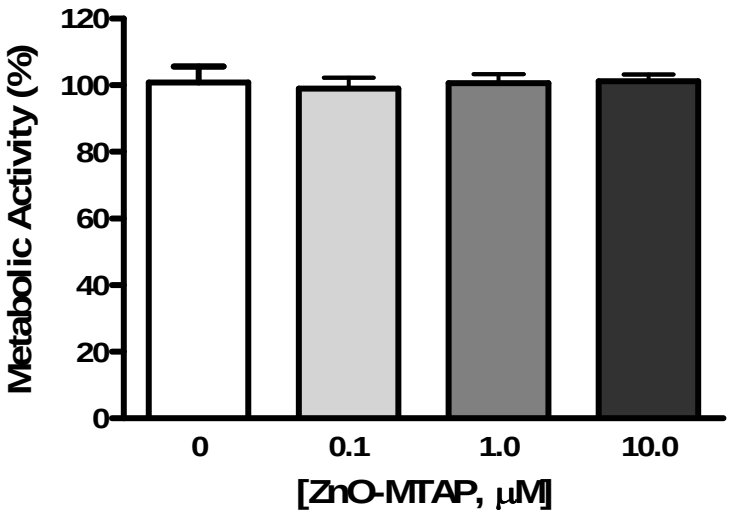

Figure 35. Effects of ZnO-MTAP conjugates alone on OVCAR-3 cell viability. Cells were seeded into 96-well plates ($1x10^5$ cells /ml) and allowed to attach for 48 hours. The cells were exposed to ZnO-MTAP conjugates (0.1, 1 or 10 μM) under dark conditions. Cell viability was evaluated 24 hours later using the MTT assay. An asterisk indicates a statistically significant difference compared to controls ($p < 0.05$).

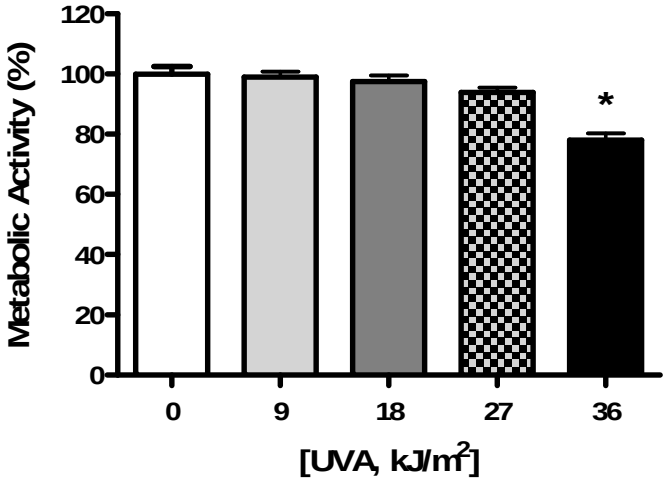

Figure 36. Effects of UVA irradiation alone on OVCAR-3 cell viability. Cells were seeded into 96-well plates ($1x10^5$ cells /ml) and allowed to attach for 48 hours. The cells were exposed to UVA at 9, 18, 27 or 36 kJ/m^2. Cell viability was evaluated 24 hours later using the MTT assay. An asterisk indicates a statistically significant difference compared to controls ($p < 0.05$)

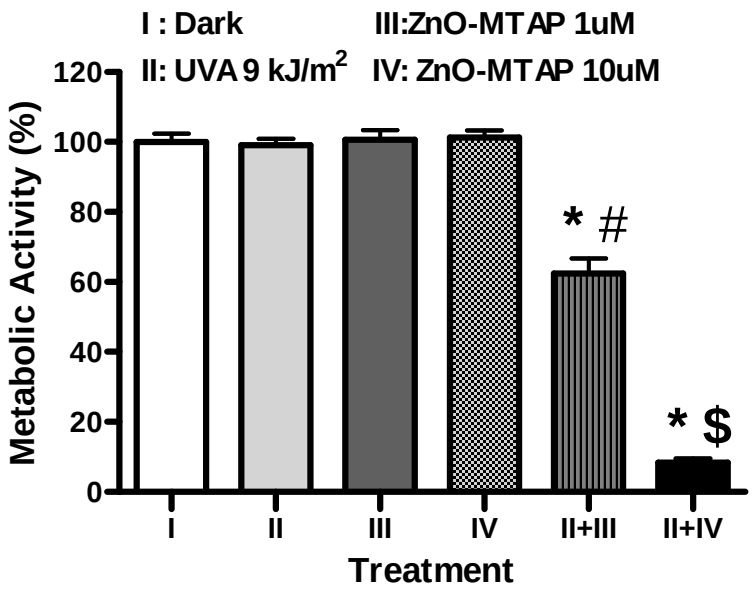

Figure 37. Effect of co-exposure to ZnO-MTAP conjugates and UVA on OVCAR-3 cell viability. OVCAR-3 cells were seeded (1 x 10^5 cells/ml) on 96-well plates 48 hours prior to treatment with ZnO-MTAP conjugates (1 or 10 µM) under dark conditions. After 4 hours, cells were irradiated with UVA at the dose of 0 (dark) or 9 kJ/m^2 and cell viability was evaluated twenty hours later. An asterisk indicates a statistically significant difference compared to group II ($p < 0.05$). A pound or dollar sign indicates a statistically significant difference compared to group III or group IV, respectively ($p < 0.05$).

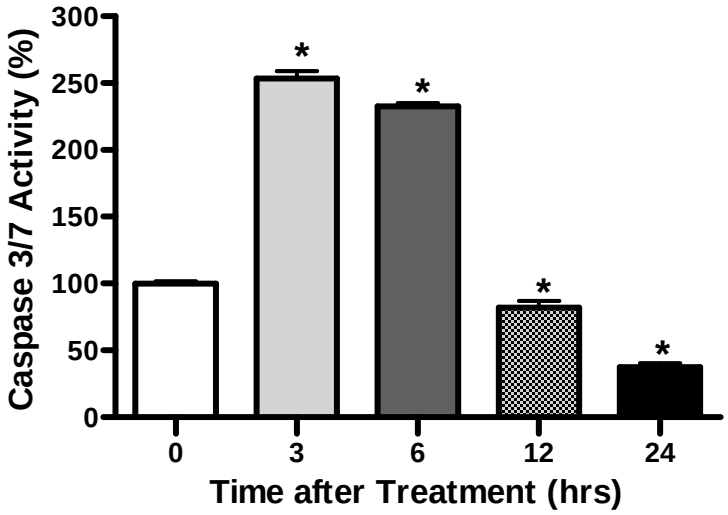

Figure 38. Effect of co-exposure to ZnO-MTAP conjugates and UVA on caspase 3/7 activity in OVCAR-3 cells. Cells were seeded into 96 well plates ($1x10^5$ cells /ml) and allowed to attach for 48 hours. ZnO-MTAP conjugates (10 µM) were then added and cells were subsequently exposed to UVA (9 kJ/m^2). Caspase 3/7 activity was measured at 3, 6, 12, or 24 hours later. An asterisk indicates a statistically significant difference compared to controls ($p < 0.05$).

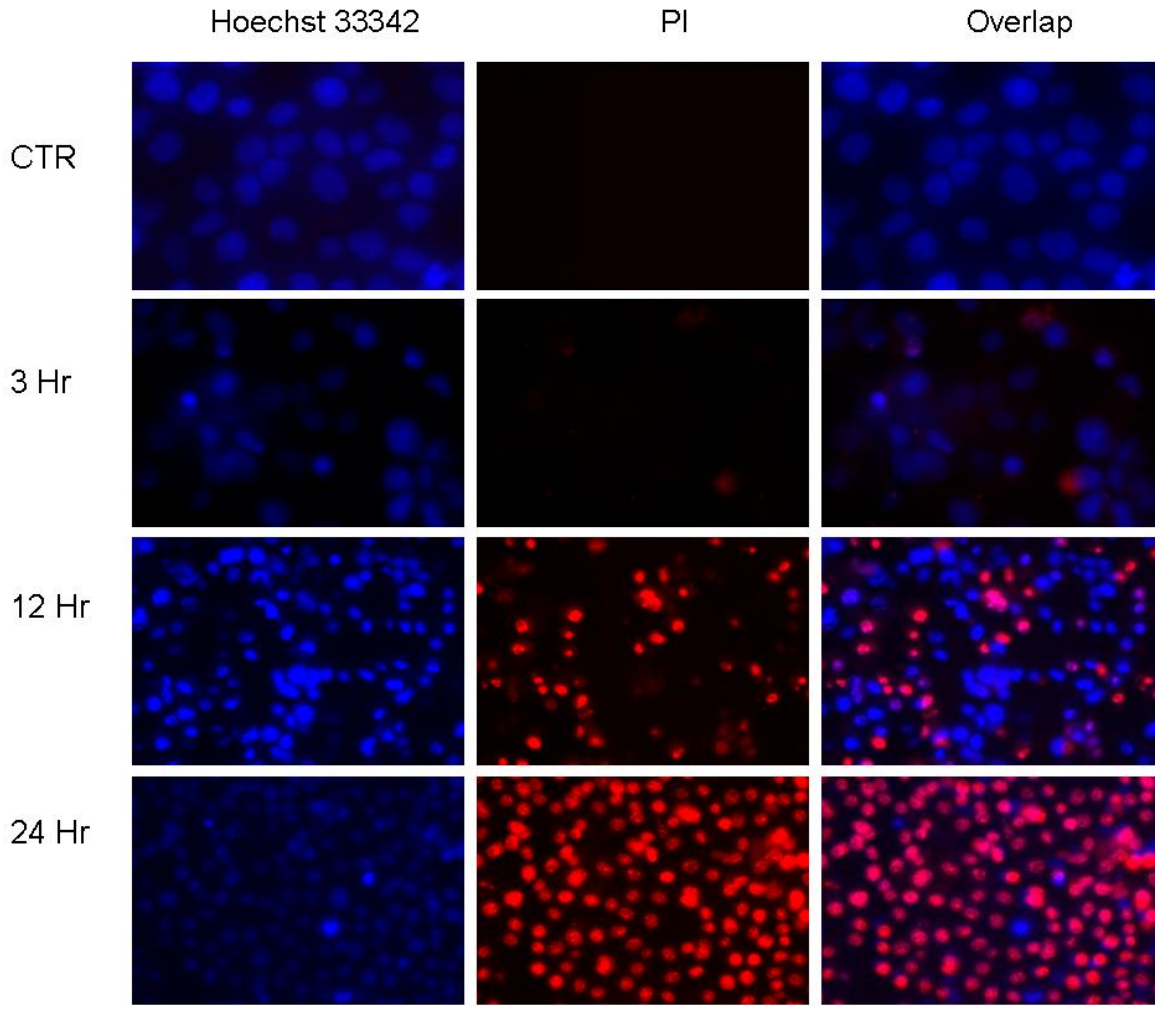

Figure 39. Hoechst 33342 and propidium iodide staining of OVCAR-3 cells co-exposed ZnO-MTAP (10 µM) and UVA light (9 kJ/m^2). At 0 (CTR), 3, 12 or 24 hours after exposure, cells were incubated with Hoechst 33342 or propidium iodide as described in methods. Nuclear morphology was evaluated by fluorescence microscopy. Magnification: 0 and 3 hr (400 x); 12 and 24 hr (200 x).

TABLE 3. Summary of dark toxicity and phototoxicity of nanoparticle conjugates

Nanoparticles	Dark Toxicity	UVA Activation	X-ray Activation	Laser 980 nm Activation
CaF2:Eu	IC50>50 ug/ml			
& Conjugates	IC50>50 ug/ml	No	No	-
ZnO	IC50=200 uM			
& Conjugates	IC50=150 uM	**Yes**	No	-
TiO2	IC50=10.1 uM			
& Conjugates	IC50=11.2 uM	No	No	-
LaF3Tb	IC50>3.5 mM			
& Conjugates	IC50=3.5 mM	-	No	-
LaF3YbEr	IC50> 1 mM			
& Conjugates	IC50> 1 mM	-	-	No
NaF3YbEr	IC50> 1 mM			
& Conjugates	IC50> 1 mM	-	-	No

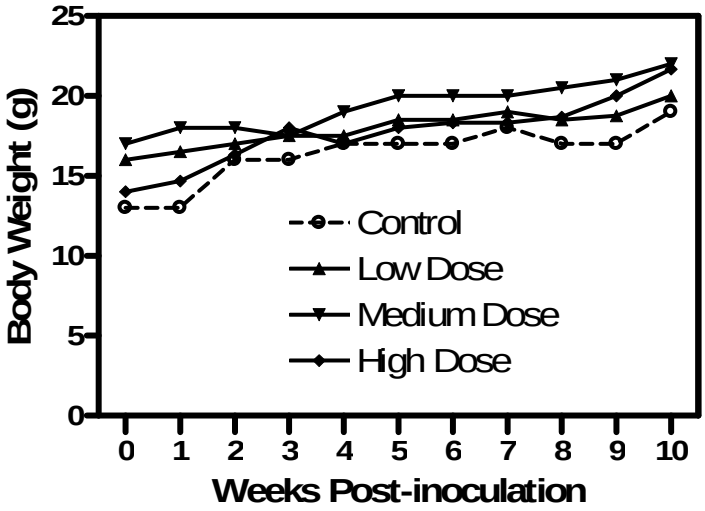

Figure 40. Effect of time after OVCAR-3 inoculation on on body weight in nude mice.Mice were inoculated with 1 x 10^7 (low dose), 1.8 x 10^7 (medium dose), or 2.4 x10^7 (high dose) OVCAR-3 cells in 300 µl of PBS (s.c.). One control mouse was injected with 300 µl of PBS (no tumor growth). The mice were weighed every week. No apparent treatment-related body weight change was noted.

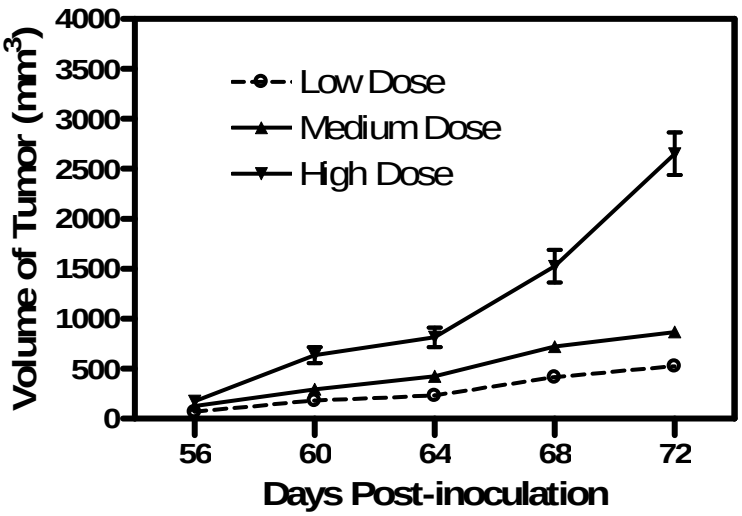

Figure 41. Effect of dose of OVCAR-3 cells on solid tumor growth. Mice were inoculated with 1 x 10^7 (low dose), 1.8 x 10^7 (medium dose), or 2.4 x10^7 (high dose) OVCAR-3 cells in 300 ul of PBS (s.c.). One control mouse was injected with 300 µl of PBS (no tumor growth). The sizes of the tumors were measured using a slide caliper every four days starting on day 56 post-inoculation. The volume of tumor increased in a dose-related manner.

Figure 42. Mice at 10 weeks post-injection with OVCAR-3 tumor cells. CTR-control mouse inoculated with PBS. Low-mouse injected with low-dose of OVCAR-3 cells. Medium-mouse injected with the medium dose of OVCAR-3 cells. High-mouse inoculated with the high dose of OVCAR-3 cells. Arrows indicate solid, subcutaneous masses of neoplastic cells that developed at the site of inoculation.

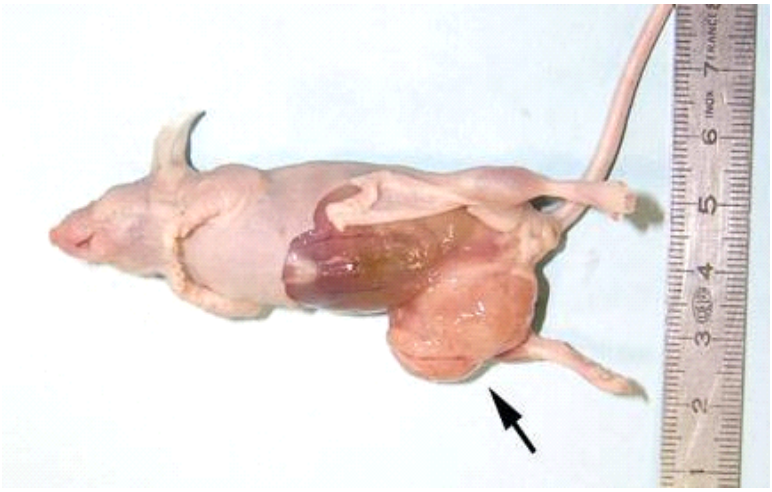

Figure 43. Mouse inoculated with the high dose of OVCAR-3 cells (s.c.) with skin removed from the mass to demonstrate a well-demarcated neoplastic mass within the subcutis in the inguinal region. The neoplasm is attached to the external surface of the body wall but does not extend into the peritoneal cavity.

.

Figure 44. Mouse inoculated with the medium dose of OVCAR-3 cells (i. p). Note the white milky fluid composed of neoplastic cells in the peritoneal cavity surrounding the abdominal viscera. No solid subcutaneous mass was present in this mouse.

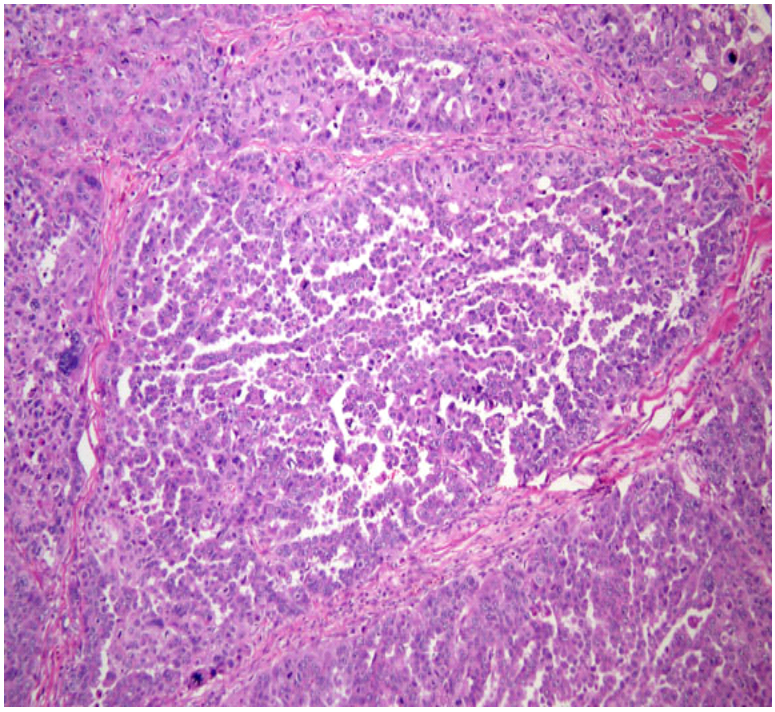

Figure 45. Photomicrograph of a solid, subcutaneous, experimentally-induced ovarian carcinoma. The mass is multinodular with neoplastic cells arranged in multiple cords and nests. H&E stain (100 x magnification).

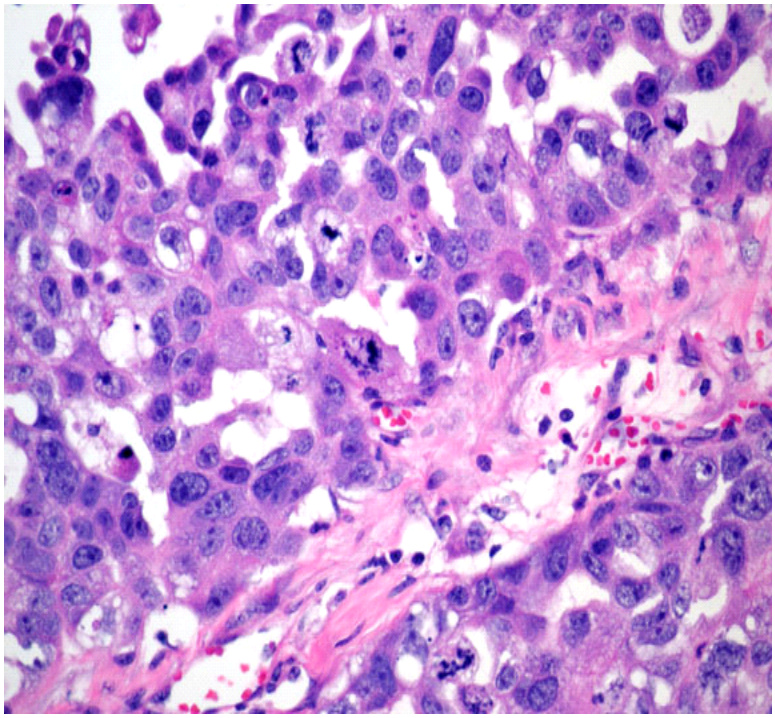

Figure 46. Photomicrograph of cellular detail in solid subcutaneous tumor. Neoplastic cells exhibit moderate to marked aniocytosis and anisokaryosis; mitotic figures are frequent (arrows). H&E stain (400 x magnification).

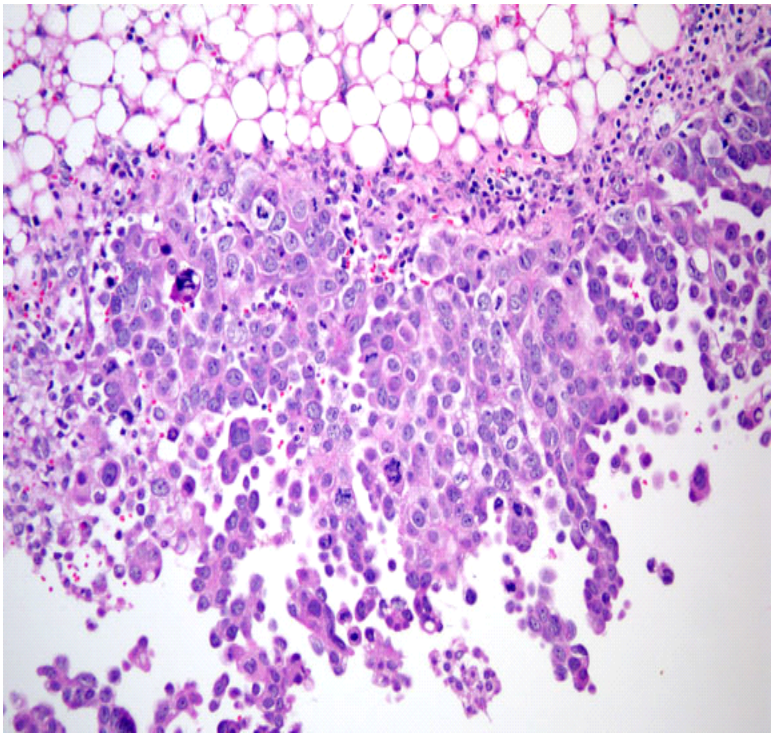

Figure 47. Solid aggregate of neoplastic cells proliferating on the serosal surface of intraperitoneal fat in intraperitoneal tumor bearing mouse. Solid intraperitoneal proliferations of cells were not grossly visible but were seen on microscopic examination. Cellular morphology and architectural arrangement is similar to that of solid, subcutaneous tumors. H&E stain (200 x magnification).

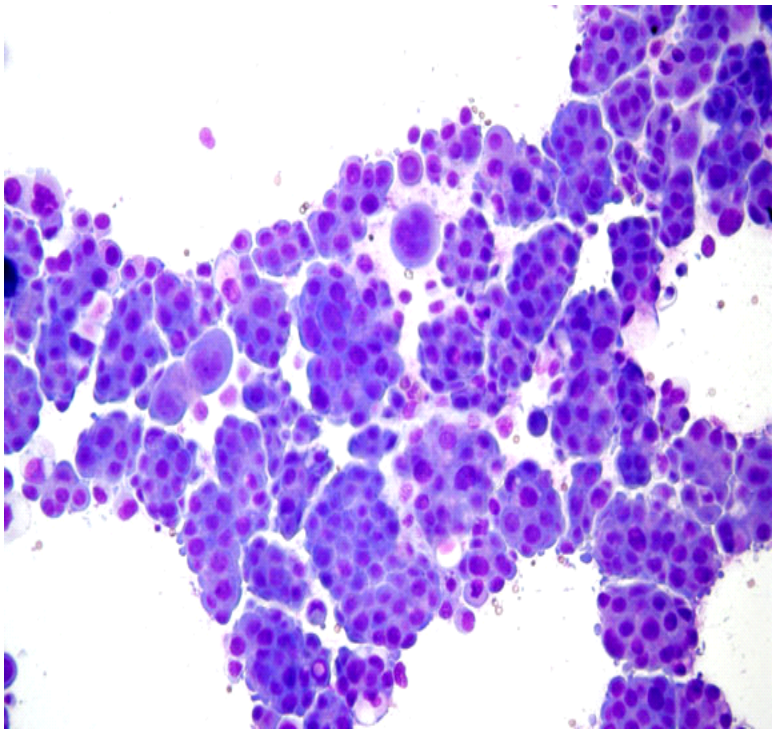

Figure 48. Photomicrograph of cytologic preparation of intraperitoneal fluid from an intraperitoneal tumor-bearing mouse. Neoplastic cells are arranged in small clumps and clusters or occasionally as individual cells. Cellular atypia appears more marked than in histopathologic sections of solid tumors. Diff-quick stain (200 x magnification).

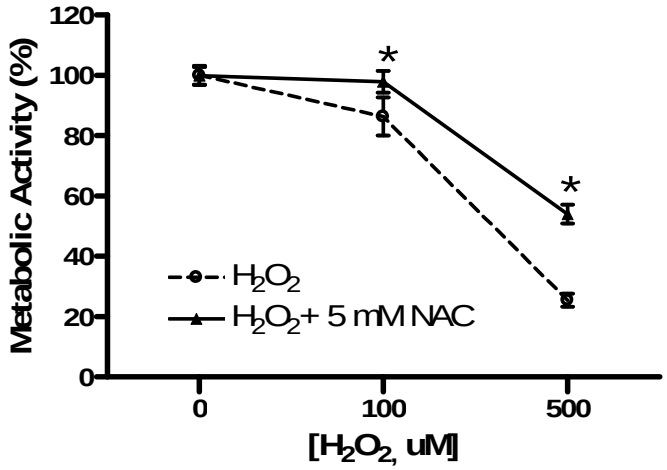

Figure 49. Effect of NAC on metabolic activity reduction by H_2O_2. $HepG_2$ cells were seeded (2 x 10^5 cells/ml) on 96-well plates 24 hours prior to treatment with H_2O_2 (100 or 500 µM). Cells were pre-exposed to N-acetyl-cysteine (NAC, 5 mM) for 2 hours followed by addition of H_2O_2. Metabolic activity was measured 48 hours later. An asterisk indicates a statistically significant difference compared to H_2O_2–only group ($p < 0.05$).

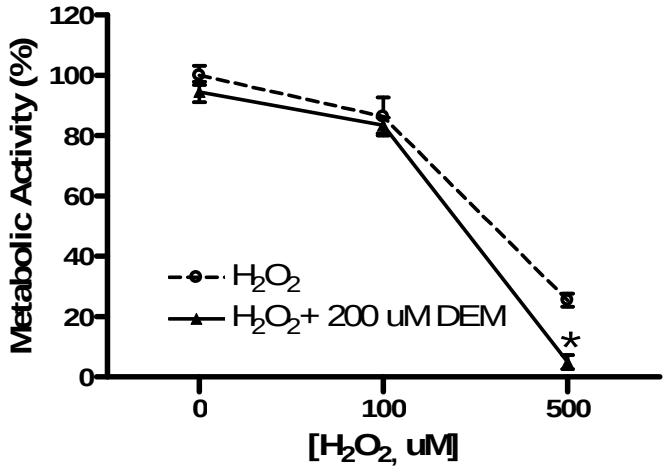

Figure 50. Effect of DEM on metabolic activity by H_2O_2. $HepG_2$ cells were seeded (2×10^5 cells/ml) on 96-well plates 24 hours prior to treatment with H_2O_2 (100 or 500 µM). Cells were pre-exposed to diethyl maleate (DEM, 200 µM) for 2 hours and then exposed to H_2O_2. Metabolic activity was measured 48 hours later. An asterisk indicates a statistically significant difference compared to H_2O_2-only group ($p < 0.05$).

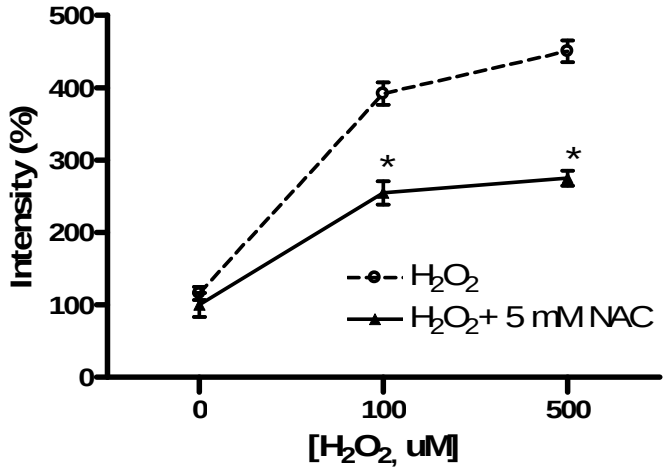

Figure 51. Effect of NAC on reactive oxygen species generation by H_2O_2. $HepG_2$ cells were seeded (2 x 10^5 cells/ml) on 96-well plates 24 hours prior to treatment with H_2O_2 (100 or 500 µM). Cells were pre-exposed to N-acetyl-cysteine (NAC, 5 mM) for 2 hours. CM-H_2DCFDA (10 µM) was added 30 minutes later. Reactive oxygen species were measured using a fluorescence microplate reader. An asterisk indicates a statistically significant difference compared to H_2O_2-only group ($p < 0.05$).

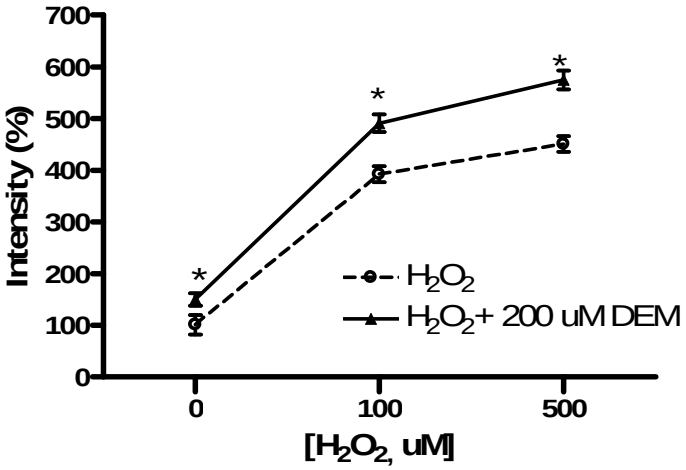

Figure 52. Effect of DEM on reactive oxygen species generation by H_2O_2. $HepG_2$ cells were seeded (2 x 10^5 cells/ml) on 96-well plates 24 hours prior to treatment with H_2O_2 (100 or 500 µM). Cells were pre-exposed to diethyl maleate (DEM, 200 µM) for 2 hours. CM-H_2DCFDA (10 µM) was added 30 minutes later. Reactive oxygen species were measured using a fluorescence microplate reader. An asterisk indicates a statistically significant difference compared to H_2O_2-only group ($p < 0.05$).

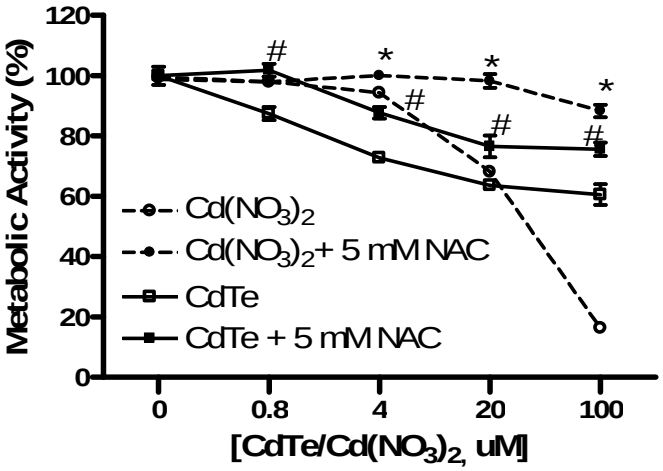

Figure 53. Effect of NAC on metabolic activity by CdTe and $Cd(NO_3)_2$. $HepG_2$ cells were seeded (2 x 10^5 cells/ml) on 96-well plates 24 hours prior to treatment with various concentrations of CdTe nanoparticles or $Cd(NO_3)_2$. Cells were pre-exposed to N-acetyl-cysteine (NAC, 5 mM) for 2 hours and then exposed to CdTe nanoparticles or $Cd(NO_3)_2$. Metabolic activity was measured 24 hours later. An asterisk indicates a statistically significant difference compared to $Cd(NO_3)_2$ only ($p < 0.05$). A pound sign indicates a statistically significant difference compared to CdTe only ($p < 0.05$).

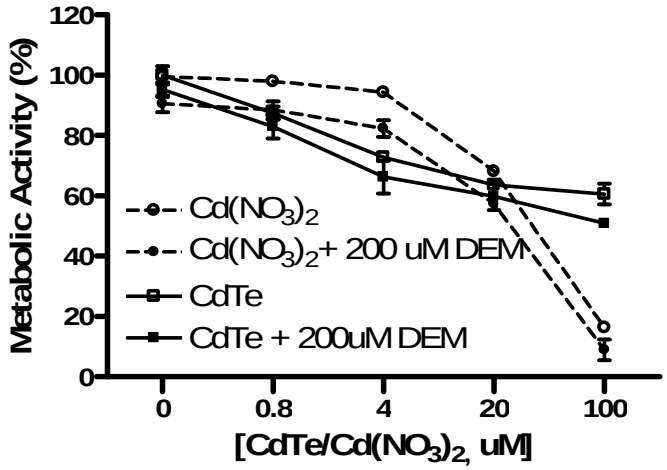

Figure 54. Effect of diethyl maleate (DEM) on changes in metabolic activity following CdTe or $Cd(NO_3)_2$ exposure. $HepG_2$ cells were seeded (2×10^5 cells/ml) on 96-well plates 24 hours prior to treatment with one of a range of concentrations of CdTe nanoparticles or $Cd(NO_3)_2$. Cells were pre-exposed to DEM (200 µM for 2 hours) and then exposed to CdTe nanoparticles or $Cd(NO_3)_2$. Metabolic activity was measured 24 hours later. An asterisk indicates a statistically significant difference compared to $Cd(NO_3)_2$ only ($p < 0.05$). A pound sign indicates a statistically significant difference compared to CdTe only ($p < 0.05$).

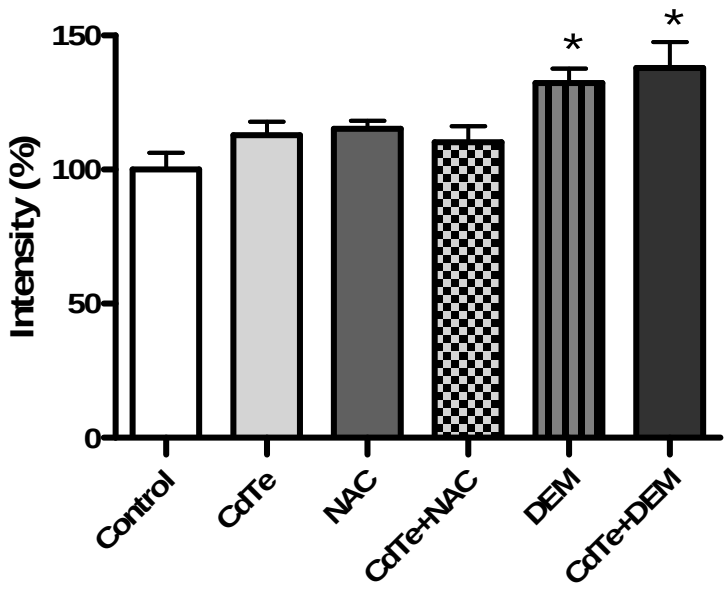

Figure 55. Effect of N-acetylcysteine (NAC) or diethyl maleate (DEM) on reactive oxygen species following exposure to CdTe nanoparticles. $HepG_2$ cells were seeded (2×10^5 cells/ml) on 96-well plates 24 hours prior to treatment with either NAC (5 mM) or DEM (200 µM) for 2 hours. The cultures were then exposed to CdTe-Red nanoparticles (100 µM for 30 minutes). CM-H_2DCFDA (10 µM) was added 30 minutes later. Reactive oxygen species were measured using a fluorescence microplate reader. An asterisk indicates a statistically significant difference compared to control ($p < 0.05$).

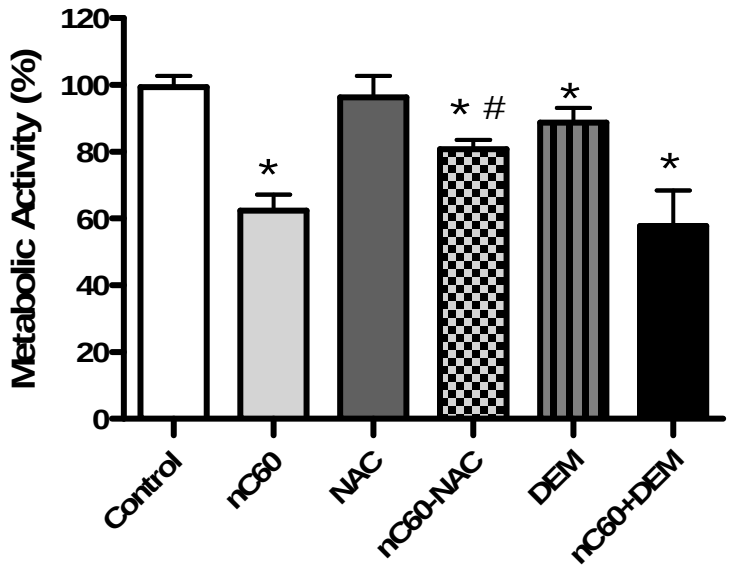

Figure 56. Effect of N-acetyl cysteine (NAC) or diethyl maleate (DEM) on metabolic activity changes following nC_{60}-AQ exposure. $HepG_2$ cells were seeded (2 x 10^5 cells/ml) on 96-well plates 24 hours prior to treatment with NAC (5 mM for 2 hours) and then exposed to nC_{60}-AQaggregates (3,300 ppm). Metabolic activity was measured 24 hours later. An asterisk indicates a statistically significant difference compared to control ($p < 0.05$). A pound sign indicates a statistically significant difference compared to nC_{60}–AQ only ($p < 0.05$).

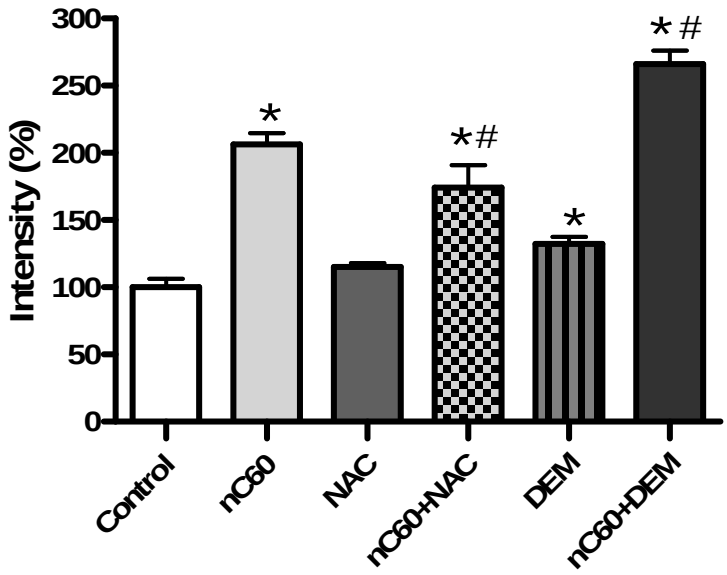

Figure 57. Effect of N-acetyl cysteine (NAC) or diethyl maleate (DEM) on reactive oxygen species levels following exposure to nC_{60}-AQ. $HepG_2$ cells were seeded (2 x 10^5 cells/ml) on 96-well plates 24 hours prior to pre-exposure to either NAC (5 mM) or DEM (200 µM) for 2 hours. The cultures were then exposed to nC_{60}-AQ (3,300 ppm). CM-H_2DCFDA (10 µM) was added 30 minutes later. Reactive oxygen species were measured using a fluorescence microplate reader. An asterisk indicates a statistically significant difference compared to control ($p < 0.05$). A pound sign indicates a statistically significant difference compared to nC60-AQonly ($p < 0.05$).

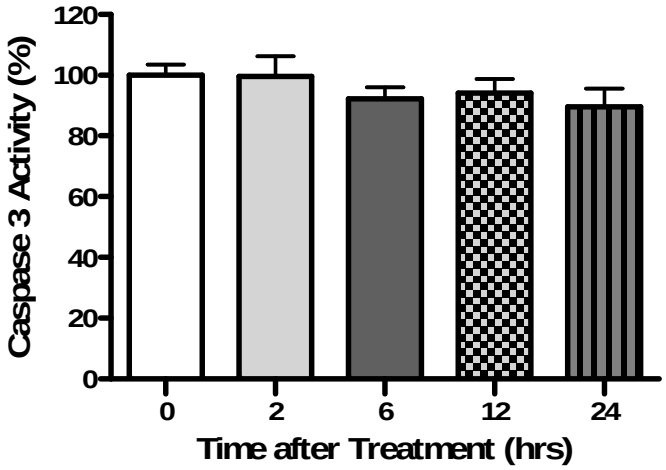

Figure 58. Effect of nC_{60}-AQ on caspase 3/7 activity. $HepG_2$ cells were seeded (1 x 10^5 cells/ml) on 96-well plates 24 hours prior to treatment with nC_{60}-AQ (3,300 ppm). Caspase 3/7 activity was measured at 2, 6, 12, or 24 hours later. An asterisk indicates a statistically significant difference compared to control ($p < 0.05$).

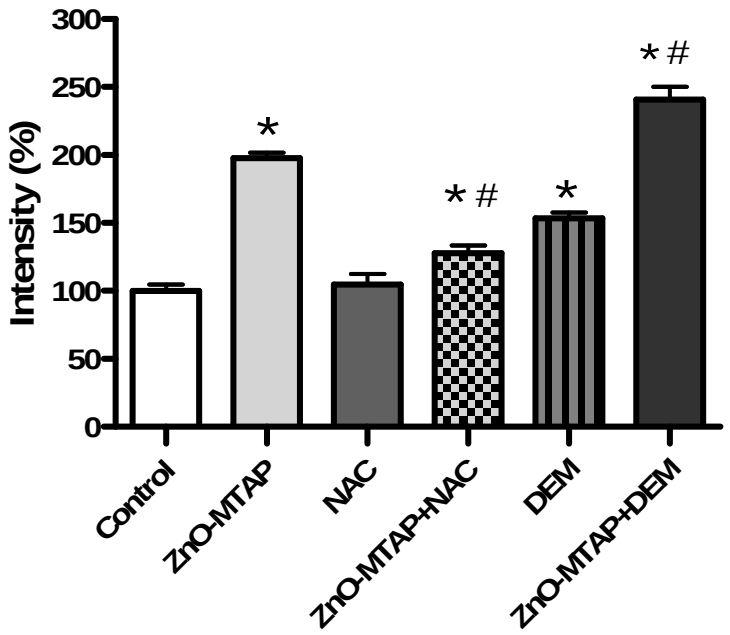

Figure 59. Effect of N-acetyl cysteine (NAC) or diethyl maleate (DEM) on reactive oxygen species levels following exposure to ZnO-MTAP conjugates and UVA light. OVCAR-3 cells were seeded (1 x 10^5 cells/ml) on 96-well plates 48 hours prior to treatment with ZnO-MTAP conjugates (10 µM) under dark conditions. After 2 hours, cells were pre-exposed to either NAC *5 mM) or DEM (200 µM) for 2 hours. The cultures were then exposed to 9 kJ/m^2 UVA. CM-H_2DCFDA (10 µM) was added 30 minutes later. Reactive oxygen species were measured using a fluorescence microplate reader. An asterisk indicates a statistically significant difference compared to control ($p < 0.05$). A pound sign indicates a statistically significant difference compared to ZnO-MTAP ($p < 0.05$).

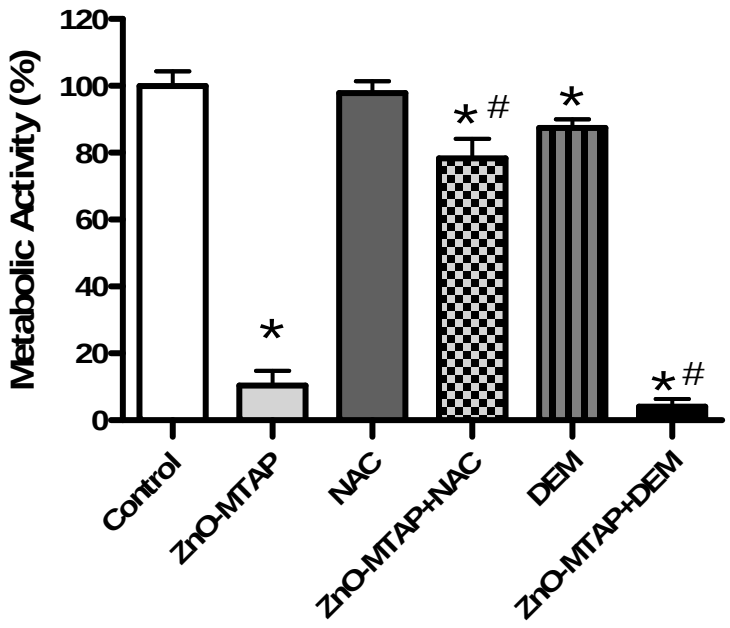

Figure 60. Effect of N-acetyl cysteine (NAC) or diethyl maleate (DEM) on metabolic activity changes following exposure to ZnO-MTAP conjugates and UVA light. OVCAR-3 cells were seeded (1 x 10^5 cells/ml) on 96-well plates 48 hours prior to treatment with ZnO-MTAP conjugates (10 µM) under dark conditions. After 2 hours, cells were pre-exposed to either NAC (5 mM) or DEM (200 µM) for 2 hours. The cultures were then exposed to 9 kJ/m^2 UVA. Metabolic activity was measured 24 hours later. An asterisk indicates a statistically significant difference compared to control ($p < 0.05$). A pound sign indicates a statistically significant difference compared to ZnO-MTAP ($p < 0.05$).

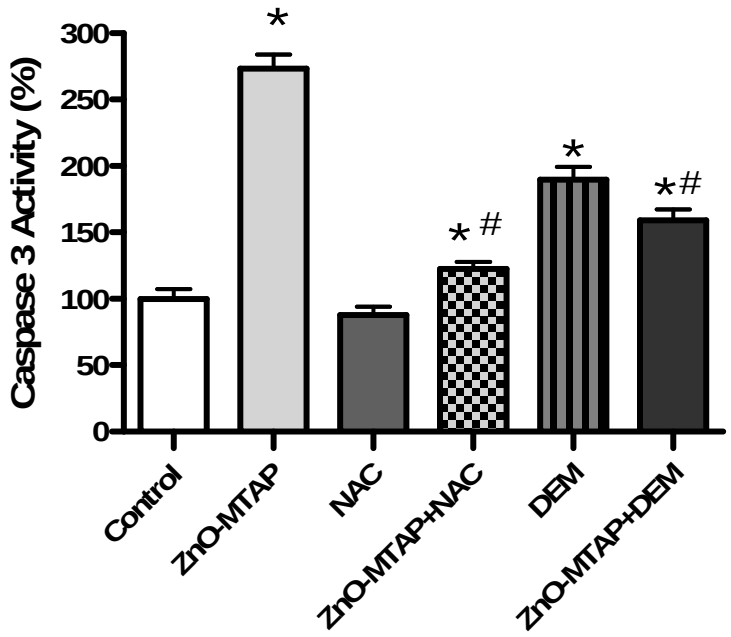

Figure 61. Effect of N-acetyl cysteine (NAC) or diethyl maleate (DEM) on caspase 3/7 activity following exposure to ZnO-MTAP conjugates and UVA light. OVCAR-3 cells were seeded (1 x 10^5 cells/ml) on 96-well plates 48 hours prior to treatment with ZnO-MTAP conjugates (10 µM) under dark conditions. After 2 hours, cells were pre-exposed to either NAC (5 mM) or DEM (200 µM) for 2 hours. The cultures were then exposed to 9 kJ/m^2 UVA. Caspase 3/7 activity was measured 3 hours later. An asterisk indicates a statistically significant difference compared to control ($p < 0.05$). A pound sign indicates a statistically significant difference compared to ZnO-MTAP ($p < 0.05$).

CHAPTER IV

DISCUSSION

Toxicity and Distribution of CdTe NPs *in vitro* and *in vivo*

We demonstrated that CdTe nanoparticles can elicit concentration- and size-dependent cytotoxicity in human hepatoma $HepG_2$ cells (Figure 5-7). Based on results obtained using the MTT assay for cell viability, different sized CdTe particles exhibited different cytotoxic potencies, with the smaller sized (green and yellow, 2-4 nm) nanoparticles being more potent than the larger sized (red, 6 nm) particles.

Shiohara and colleagues reported that the cytotoxicity of CdSe nanoparticles could depend both on the relative size of the particles and the cell types exposed [42]. Our results suggest that size can be important in the cytotoxicity of CdTe nanoparticles in $HepG_2$ cells. Lovric and coworkers [32] showed that different-sized CdTe nanoparticles exhibited differential subcellular distribution in rat pheochromocytoma (PC12) and N9 murine microglial cells, which could have a prominent role in their relative cytotoxic potential.

A previous study by Derfus and coworkers [31] suggested that cytotoxicity of CdSe was correlated with the liberation of Cd^{2+} from the nanoparticle lattice.

Using our synthetic methods, it was possible that some free Cd^{2+} remained in the nanoparticles “as prepared”. We therefore compared the cytotoxicity of CdTe-Red nanoparticles as prepared with nanoparticles that were partially purified by methanol sedimentation. While the purified nanoparticles still exhibited relatively similar photophysical properties, their cytotoxicity was markedly reduced compared to the nanoparticles as prepared (Figure 8). This suggests that the nanoparticles as prepared may have some free cadmium or other contaminant that could increase the cytotoxicity of nanomaterials.

We also estimated the stability of CdTe nanoparticles in culture. Aggregation of nanoparticles could have a dramatic effect on their physicochemical properties, and thus their utility in subsequent applications. There was apparent aggregation/agglomeration of the CdTe-Red nanoparticles over time (Figure 9). This aggregation appeared to be primarily extracellular, however, as similar clusters were noted when culture medium containing the nanoparticles was incubated in the absence of cells (data not shown). This could have importance in any potential applications of these or similar CdTe nanoparticles. If they cluster or aggregate under physiological conditions, this could impair their photophysical properties. It must be noted that these are relatively static conditions, and this aggregation may occur less readily under *in vivo* conditions, e.g., following systemic administration.

Relatively few studies have evaluated *in vivo* toxicity of nanoparticles in animal models [25, 26, 28, 97, 98]. Previous studies suggest that these types of particles may be useful for *in vivo* imaging [46], potentially following intravenous

administration. We therefore evaluated the potential toxicity of CdTe-Red particles in rats following intravenous administration. Systemic administration of CdTe nanoparticles could potentially lead to nanoparticle distribution throughout the body however, and potentially elicit organ-specific responses. While there was a minimal (but significant) reduction in body weight 24 hours after dosing, few signs of overt toxicity were noted following intravenous administration of these particles. Histopathologic analysis of major organ systems found no treatment-related evidence of organ damage. Clinical chemistry indicators also suggested no evidence of liver or kidney damage or other changes in classical blood or urinary markers (although there was a trend for elevated blood alanine aminotransferase).

Interestingly, locomotor activity was significantly **decreased** shortly after intravenous nanoparticle dosing, while activity levels were significantly **increased** 24 hours after dosing (Figure 18). Motor activity is an integrative measure of nervous system function [99, 100]. Thus, the robust changes in motor activity noted following nanoparticle administration suggest an alteration in nervous system function is elicited by systemic CdTe-Red exposure. Some nanoparticles have been reported to pass the blood brain barrier following systemic administration [98]. Thus, under some conditions the CdTe-Red particles used herein may gain access to the central nervous system and disrupt integrated neural functions. On the other hand, free cadmium (as either contaminant or from degradation) could be responsible. The relative role of the nanoparticles

themselves, or Cd from the nanoparticles, in these motor effects requires further study.

It should be noted that the exposure level in our in vivo study (2 µmol/kg, i.v.) is markedly lower than the exposure level studied inhalation administration of CdTe nanoparticles [28] .In contrast, our exposure level was higher than another study in mice using similar Cd-containing nanoparticles for biomedical imaging (6 nmol/mouse, i.v.) [46]. Thus, at a level of exposure that could apparently be useful in biomedical (e.g., imaging) applications, few signs of overt toxicity were noted while an integrative measure of neurobehavioral function, locomotor activity, was affected by CdTe nanoparticle administration.

Our studies demonstrate that CdTe nanoparticles can elicit cytotoxicity in $HepG_2$ cells, and that size and purification (contaminants) may be important modifying factors. With *in vivo* exposure to CdTe-Red particles, few signs of overt toxicity or clinical chemistry indicators of adverse response were noted, but changes in locomotor activity were observed. These studies provide a framework for further studies to characterize the toxic potential of CdTe-containing semiconductor nanoparticles.

As noted above, understanding the mechanism of toxicity for synthetic nanomaterials can be useful in developing safer materials or handling procedures, and potentially therapeutic or protective measures to prevent intoxication. To evaluate the possible mechanism of cytotoxicity elicited by CdTe nanoparticles, we evaluated indicators of apoptosis including Hoechst 33342 staining, caspase induction and DNA fragmentation. Nuclear condensation was

elicited after 24 hours incubation with CdTe-red particles, but not earlier (i.e., at 4 hours after exposure, Figure 13). Similarly, caspase 3/7 activity was induced by CdTe-red particles in a dose- and time-dependent manner (Figures 14 and 15). In addition, the hallmark of apoptosis, DNA fragmentation was noted in cells after 48 hours exposure to CdTe-Red nanoparticles (Figure 16). Thus, several endpoints suggested that CdTe nanomaterials may induce apoptosis in $HepG_2$ cells.

It is known that free cadmium can induce the expression of the heavy metal-binding protein, metallothionein, in $HepG_2$ cells. Cadmium may exist as free metal in preparations of Cd-containing nanoparticles, and it may be produced in such preparations during storage or through environmental/biological degradation. We therefore evaluated metallothionein expression in $HepG_2$ cells exposed to CdTe-Red nanoparticles, using cadmium (0.2 µM) as a positive control. Metallothionein mRNA was increased by CdTe-Red nanoparticles at lower concentrations (0.2 - 1µM) but decreased at higher concentrations (20 - 100 µM). This biphasic dose-response curve may indicate that low levels of cadmium in the nanoparticle preparation indeed increased expression of metallothionein, but that higher levels actually decreased its expression. Interestingly, metallothionein protein levels were lower in CdTe treated cells (Figure 18). This may indicate that cytotoxicity can be elicited by the CdTe nanoparticle themselves, as well as by free cadmium.

Discussion of the potential toxicity of semiconductor nanoparticles can be confounded by the high diversity of such nanomaterials being synthesized. It was

reported that the cytotoxicity of CdSe nanoparticles correlated with the liberation of free Cd^{2+} ions [31]. Recent studies reported that the cytotoxicity of CdSe nanoparticles depended both on the relative size of the particles and the types of target cells [42]. It has also been reported that marked cytotoxicity occurs in PC12 and N9 cells exposed to concentrations as low as 10 μg/ml CdSe [32]. Cell death was associated with chromatin condensation and membrane alterations and was more prominent with smaller (about 2 nm) than larger (about 5 nm) nanoparticles [32]. There is also evidence that surface chemistry, in particular surface characteristics that impair particle aggregation, has an important role in the cytotoxicity of nanoparticles [101]. Characterization of the surface and other physical properties is obviously a critical factor in the accurate assessment of biological reactivity/toxic potential. But even if nanomaterials being evaluated have been completely and carefully characterized, there is still the possibility of alteration or degradation of the materials once in the biological system(s).

In the study of inhaled particles, surface area and particle size played important roles in toxicity [25, 26, 97]. Furthermore, movement of the particles from the alveoli to interstitial spaces may have been facilitated by degradation of the particles into smaller units within the tissues, thus the transformation of nanomaterials inside the body is a potential concern [102, 103]. In a pulmonary toxicity study, CdTe nanoparticles elicited extensive pulmonary damage (expressed as increased lung weight, decreased macrophages, increased lactate dehydrogenase, increased protein content in bronchoalveolar fluid, terminal bronchiolar necrosis with fibrin exudates, and type II cell hyperplasia) [28, 104].

As CdTe nanoparticles are fine-tunable and will emit stable fluorescence at specific excitation wavelengths, confocal microcopy can potentially be a very useful tool for evaluating their localization. Transmission electron microscopy can also be useful for determining tissue distribution. To understand mechanisms of toxicity and thereby prevent or decrease the potential toxicity of these particles,. In addition, distribution studies of nanoparticles in vivo can help determine whether the particles are effectively distributed and accumulate in tissues, or effectively eliminated. Such findings will be important in further development and application of these types of materials.

As shown above (Figure 7), we observed size-dependent cytotoxicity of CdTe nanoparticles, i.e., 2 nm CdTe particles were more potent at decreasing cell viability in $HepG_2$ cells than 6 nm CdTe nanoparticles [105]. The results suggested that CdTe-Red may be transported into cells through the membrane into the cytoplasm, and possibly into the nucleus, in a size- and time-dependent manner. The apparent differential distribution of the different sized particles suggests that these nanoparticles may form complexes with proteins and possibly enter via endocytic pathways [106].

Our results are the first to suggest neurotoxic potential of CdTe nanoparticles following systemic administration (Figures 21 and 22). Cadmium was detected in both liver and brain following systemic dosing (Figure 24-27). However, the cadmium as measured (by atomic absorption) could be from intact nanoparticles entering the tissues, or from free cadmium as contaminant or degradation product. We used x-ray analysis to determine if both cadmium and

telluride could be detected in the same scan. Indeed, x-ray analysis suggested that both cadmium and telluride were together in the tissue.To our knowledge, this is the first demonstration of semiconductor nanoparticles in tissues by transmission electron microscopy using x-ray analysis. CdTe nanoparticles may therefore enter tissues (including brain) as intact nanomaterials following systemic administration. On the other hand, free cadmium and telluride could conceivably distribute into tissues and be detected in the same tissue section.

Cytotoxicity of nC_{60} in $HepG_2$ Cells

The chemical and physical properties of nC_{60} made by different methods could lead to differential biological effects. These differential properties include size, morphology, charge and hydrophobicity [91, 107]. Therefore, we compared the cytotoxicity of nC_{60} synthesized by four different methods, i.e., solvent extraction using tetrahydrofuran (THF), solvent extraction using toluene/tetrahydrofuran/acetone (TTA), sonication with toluene extraction (SON), and prolonged stirring in aqueous medium (AQ). We found marked differences in cytotoxicity with nC_{60} prepared by the different methods (Figure 24). Essentially, nC_{60} synthesized by extraction with TTA appeared more cytotoxic than the other three types of nC_{60}. These differences may not be due to the aggregates themselves, but due to residual organic solvent that was not removed during the preparation (Ausman, unpublished data). Others have suggested that the toxic effects of nC_{60} prepared with organic solvents may be due to residual solvent in the preparation [41].

To obtain more purified samples of nC_{60}, samples of aggregates prepared by the four different methods were extensively concentrated by flash evaporation. Following such purification, none of the preparations (up to 3,300 ppm) elicited cytotoxicity in $HepG_2$ cells (data not shown). We subsequently reevaluated these same samples after one month in storage. Interestingly, the AQ, THF and TTA nC_{60} samples all affected cell viability (Figure 29), and cytotoxicity of nC_{60}-AQwas concentration–dependent (Figure 30). Organic solvent retained in the nC_{60} prepared by some methods may be important under some conditions. The toxicity ofnC_{60} may not, however be only due to residual solvent. As previously noted with characterizations such as CdTe nanoparticles, surface properties or or size can potentially contribute to the toxicity of nanomaterials.

Although the cytotoxic mechanism of nC_{60}-AQ is unknown, it is possible that an epoxide can form at surface sites with prolonged exposure to oxygen (air), which could in turn change the physical properties and reactivities of the nanomaterials (e.g., leading to agglomeration, K. Ausman, personal communication). In addition, preparation of nC_{60}-AQ requires air (personal communication, K. Ausman); therefore oxygen may influence the the toxic potential of nC_{60}-AQ by facilitating oxidative mechanisms. Previous studies have shown that nC_{60}-THF induced cytotoxicity through oxidative stress, leading to lipid peroxidation in human dermal fibroblasts, human $HepG_2$ cells, and human astrocytes [38]. Our studies using a reactive oxygen species probe demonstrated increased levels of reactive oxygen species in a time-dependent manner after exposure to nC_{60}-AQ. Furthermore, ROS and cytotoxicity of nC_{60} were modulated

by pre-exposure to either NAC or DEM (Figures 56 and 57), providing further evidence of oxidative stress mechanisms in the toxicity of nC_{60}. Further studies could attempt to modulate the degree of possible oxygenation (epoxidation) of nC_{60} to determine its relative contribution to the toxicity of nC_{60}.

Phototoxicity and Distribution of NP Conjugates *in vitro*

Nanomaterials have numerous potential applications for targeted drug therapy [81-83]. We evaluated the potential phototoxicity of ZnO-MTAP conjugates using UVA irradiation as a chemotherapeutic approach against ovarian cancer cells. The cytotoxic potency of a photosensitizer depends directly on the amount of reactive oxygen species it generates [108]. Therefore, we measured reactive oxygen species produced by the ZnO-MTAP nanoparticle conjugates under both dark and light conditions using the fluorescent probe, CM-H_2DCFDA. Essentially no evidence of ROS generation was noted with ZnO-MTAP conjugates under dark conditions, while concentration- and irradiation dose-dependent effects were noted with UVA irradiation (Figure 33). Thus, these nanoparticle conjugates appeared effective at coupling irradiation with the luminescence of the particle to produce reactive species.

To evaluate if these conjugates could accumulate in cells, OVCAR-3 cells were incubated with ZnO-MTAP conjugates (10 µM) for 4 hours, and then evaluated by confocal microscopy. Indeed, conjugates appeared to accumulate in the cytosol of OVCAR-3 cells (Figure 34). A number of studies suggest that the uptake of various types of nanoparticles is mediated by an endocytic pathway [109-111]. Since reactive oxygen species typically have a short half-life,

internalization of nanoparticle conjugates is likely a critically important factor in effective photodynamic therapy for targeting specific cells.

Our studies demonstrated that ZnO-MTAP conjugates can be activated by UVA light to generate reactive oxygen species and to decrease cell viability in human OVCAR-3 ovarian cancer cells *in vitro*. In self-lighting photodynamic therapy, the emission wavelength of the nanoparticle should be matched to the absorbance wavelength of the photosensitizer for effective coupling. We reported that ZnO nanoparticles can effectively transfer energy to MTAP (about 83%) under UVA illumination after conjugation [86]. For safe photodynamic therapy, the photosensitizer should be inactive under dark conditions. Indeed, the ZnO-MTAP conjugates generated essentially no reactive oxygen species in the absence of irradiation (Figure 33). Considerable evidence suggests that mitochondrial function can be targeted in photodynamic therapy approaches [112-114]. We evaluated cell viability by the MTT assay, which relies on mitochondrial enzymes to reduce the formazan dye product. The reduced activity in the MTT assay in cells exposed to ZnO-MTAP conjugates in the presence of UVA suggests that the conjugates are photoactivated to generate reactive oxygen species, leading to mitochondrial damage and reduced cell viability. Thus, these conjugates demonstrate the proof of concept for self lighting photodynamic therapy using ZnO nanoparticles and UVA light.

It should be noted that any form of irradiation can potentially have adverse effects on cells and tissues [115, 116]. UVA (320-400 nm) is less harmful than either UVB (290-320 nm) or UVC (200-290 nm) due to its relatively low energy.

In clinical applications, UVA and a photosensitizer have been successfully used to treat skin diseases such as eczema and psoriasis [117]. In our studies, UVA alone at the highest exposure tested (36 kJ/m^2) led to reduced OVCAR-3 cell viability. We used 9 kJ/m^2, a subcytotoxic (Figurer 36) and biologically relevant level of exposure, to evaluate the potential phototoxicity of these conjugates [118] . While neither UVA nor the ZnO nanoparticles alone elicited cytotoxicity, the combination was highly effective at reducing cell viability (Figure 37).

There are two basic modes of cell death, i.e., necrosis and apoptosis. It has been reported that photoactivation of hematoporphyrin monomethyl ether (a porphyrin-derivative photosensitizer similar to MTAP) induced mainly necrosis in NuTu-19 ovarian cancer cells [119]. Wyld and coworkers suggested cell death in photodynamic therapy could occur through either necrosis or apoptosis, depending on the target cell type and various dosing conditions [120]. Our studies suggest that both apoptosis and necrosis can be elicited by photoactivation of ZnO-MTAP conjugates (Figure 39).

Nanotechnology applications for photodynamic therapy can utilize the advantage of size and surface properties of the materials for drug delivery [81-83]. Sunscreens containing nanoscale titanium dioxide or zinc oxide particles can effectively block UV light [4]. It has been reported that the phototoxicity of TiO_2 nanoparticles was increased by UVA light, with toxicity being related to generation of hydroxyl radical [121, 122]. We focused on the application of self-lighting optical properties of the ZnO nanoparticles in photodynamic therapy. We hypothesized that luminescence of ZnO particles elicited by UVA or other

irradiation could activate the photosensitizer MTAP, which would in turn transfer energy to molecular oxygen, followed by generation of reactive oxygen species and targeted cell destruction. The data provided indicate that these conjugates can indeed generate reactive oxygen species in the presence of UVA light that can in turn reduce tumor cell viability. Although the approach is effective with ovarian cancer cells *in vitro*, translation into whole animal applications is challenging. Nanoparticle conjugates may bind to tissue or blood proteins, potentially influencing their cellular uptake or tissue targeting. The optical properties of the nanoparticle conjugates could be modified *in vivo*. A number of studies suggest that the toxicity of nanomaterials may be markedly different in cellular and whole animal models [39, 105]. Thus, transitioning an approach from cell culture to whole animal has a number of potential pitfalls.

In our model of self-lighting photodynamic therapy, the irradiation source is perhaps the most challenging problem. X-ray irradiation is a convenient vector for photodynamic approach. Preliminary studies had indicated that X-ray irradiation could activate ZnO-MTAP conjugates in the solid state (data now shown). Thus, our initial efforts were directed at using x-irradiation to activate the conjugates in cells. Unfortunately, there was no apparent interaction between ZnO-MTAP conjugates and x-irradiation (data not shown). Thus, further work is needed to develop nanoparticle conjugates that can be activated by radiation sources that will allow deep tissue penetration. Our findings illustrate, however the overall potential for te approach of using luminescent nanoparticles conjugated with a photosensitizer in photodynamic therapy.

The ultimate goal of this project was to evaluate the phototoxicity of the nanoparticle conjugates *in vivo*. For this approach, the animal ovarian tumor model was necessary. We simultaneously developed a whole animal model of human ovarian cancer by inoculating OVCAR-3 cells into nude mice while we were studying the in vitro effects of the conjugates. We have shown that tumor growth is dose–related following subcutaneous inoculation, with solid tumor being grossly visible within 56 days after inoculation. The inoculated mice survived at least to 72 days after inoculation, without significant body weight change. An inoculation dose of 2.4 X 10^7cells/mouse appeared suitable for further studies. The development of the tumor was confirmed by necropsy and histopathological evaluation. We therefore demonstrated conditions for establishing a consistent ovarian tumor model in nude mice that could be used in future pharmacological evaluations of nanoparticle-conjugate photodynamic therapy.

Oxidative Stress as a Mechanism of Nanotoxicity

While novel engineered nanomaterials bring exciting applications and advances in technology, they also pose new concerns for regulation and safety evaluation. Tons of different nanoscale materials are potentially going to be released into the environment, thus risk assessment of nanomaterials will be increasingly needed. Development of biomarkers of nanotoxicity could be beneficial in the assessment of risk. Indicators of oxidative stress may be important biomarkers of toxicity for selected nanomaterials.

If toxicity of nanomaterials is elicited by oxidative stress, that toxicity should be reduced by enhancing intracellular antioxidant status. We studied this in vitro by pre-treating cells with N-acetyl-cysteine (NAC), precursor of glutathione, prior to nanomaterial challenge. On the other hand, ROS-mediated cytotoxicity should be increased by reducing intracellular antioxidant levels. To study this possibility, we pre-treated cells with the glutathione depletor diethyl maleate (DEM) before exposing the cells to the nanomaterials. Through these approaches, we were able to define whether ROS likely played a role in the toxicity of the selected nanomaterials under study.

We first evaluated whether CdTe nanoparticles can mediate toxicity through oxidative mechanisms using these approaches. It is well known that free cadmium can induce oxidative stress [93, 94, 123]. In our studies, however, the toxicity of cadmium-containing nanoparticles did not appear to be mediated through oxidative stress (Figure 53-55). Although the toxicity of CdTe nanoparticles was reduced by pre-exposure to NAC, this is likely because of direct chemical-chemical interactions (i.e., the NAC bound directly to free cadmium or possibly the CdTe nanomaterials). These results generally agree with a previous study showing that NAC (4 mM) could block cytotoxicity of CdTe-green nanoparticles [32]. Studies in which the ROS probe was used suggested however, that CdTe-induced caspase activation was not dependent on oxidative stress. Shi and coworkers reported that CdTe nanoparticles generated ROS in the presence of meso-tetra(4-sulfonatophenyl)porphine dihydrochloride (TSPP) with photoactivation, but no ROS were detected when the nanoparticles were

illuminated without TSPP [124]. It should be stressed that cells in all of our studies on the cytotoxicity of CdTe nanoparticles were exposed under dark conditions. Thus, while NAC appears to protect from CdTe cytotoxicity, it does not appear to be due to reducing the amount of ROS produced.

We then evaluated the possible role of ROS in nC_{60} toxicity. The nC_{60}-AQ increased ROS levels in a time-dependent manner (Figure 32). Furthermore, the elevation in ROS was blocked by pre-exposure to NAC (Figure 57). Moreover, nC_{60}-AQ induced cytotoxicity was reduced by pre-exposure to NAC and increased by pre-exposure to DEM (Figure 56). These findings suggest that the toxicity of nC_{60} is indeed mediated through oxidative stress. As mentioned before, purity can be an important factor in the biological reactivity of nanomaterials. Although a number of studies suggest a role for oxidative stress in the toxicity of nC_{60} [38, 40], it should be noted that these nC_{60} materials were typically synthesized using organic solvents. Recently, Henry and coworkers did not detect THF itself but did find gamma-butyrolactone, an oxidation product of THF, in nC_{60}-THF preparations, suggesting a possible role for this degradation product in the toxicity of these types of nanomaterials [125]. Unpublished findings also suggest that during aerobic storage of nC_{60}, oxygen may oxygenate the surface and alter reactivity. Our studies with nC_{60}–AQ showing apparent increased cytotoxic potential following storage support this possibility.

Apoptosis mediated through the caspase(s) pathway has been reported in a number of studies involving photodynamic therapy [126-130]. Oxidative stress can be an important mechanism in photodynamic therapy [95, 96]. In our studies,

we demonstrated that phototoxicity of ZnO-MTAP conjugates in the presence of UVA light involved caspase 3 activation and oxidative stress. While UVA light alone can cause oxidative stress with higher exposures (40 -90 kJ/ m^2) [131, 132], , the exposure level in our studies (9 kJ/m^2) did not induce oxidative stress (Figure 33).

In summary, both nC_{60} and ZnO-MTAP conjugates/UVA appeared to elicit cytotoxicity through ROS and oxidative stress. In contrast, the cytotoxicity of CdTe nanoparticles did not appear to be mediated through this mechanism.

It is clear from these studies that the toxicity of nanomaterials is dependent on numerous factors including the general type of nanostructure, the chemical constituents, contaminants, degradation products, surface modifications, and possibly numerous other characteristics. Characterization of the sample being investigated is paramount in understanding its toxic potential. Even if well characterized, however, there is still the possibility of change in the sample over time during storage, for environmental degradation, or for biological transformation within a living organism or ecosystem.

These studies demonstrate some approaches that can be taken to evaluate the toxicity of synthetic nanomaterials, or for that fact any chemical that has relatively little information available about its toxic potential. While in vitro studies are relatively straightforward, nanomaterials have some characteristics that may make them particularly difficult to study in whole animals. One such characteristic is agglomeration. If a nanomaterial is effective in a particular application by nature of its size, and multiple nanomaterials aggregate or

agglomerate in biological systems, this will likely change its function. We noted the apparent aggregation of CdTe nanoparticles in studies with HepG2 cells. Thus, even if a nanomaterial is exceedingly well characterized before use in a biological system, it may change by this process. Obviously, it is unclear what clustering or agglomeration of nanomaterials means for toxicity potential across different types of nanomaterials. There are many unknowns regarding the biological reactivity and toxic potential of the plethora of different types of nanomaterials known, and the likely greater number to be produced in the future. Approaches such as those outlined in this study can lay the groundwork, however, for understanding the biological effects of different types of nanomaterials necessary for safely realizing their vast array of potential applications.

CHAPTER V

CONCLUSIONS

1. Toxicity of engineered nanomaterials is an open question, to be evaluated on a case-by-case basis.
2. CdTe nanoparticles elicited cytotoxicity in $HepG_2$ cells *in vitro.* No apparent hepatotoxicity was noted following *in vivo* exposure, however.
3. Surface properties contribute to nanotoxicity. The size of CdTe nanoparticles and the oxidative potential of nC_{60} play an important role in their toxicity.
4. Composition/element of the nanomaterials is also important for their toxicity potential.
5. Purity of the nanomaterials (free metal, organic solvent) can be important. The full characterization of a nanomaterial preparation is essential for understanding its biological effects.
6. Indicators of oxidative stress may serve as biomarkers in risk assessment of some nanomaterials.
7. CdTe-induced cytotoxicity is size- and concentration-dependent, involving caspase 3 activation, DNA fragmentation and metallothionein induction, but apparently not mediated by oxidative stress.

8. CdTe alters motor activity following *in vivo* dosing, suggesting the possible disruption of nervous system function.
9. Subcellular distribution of CdTe is size- and time- dependent. Atomic absorption spectrometry and x-ray analysis of transmission electron micrographs suggested CdTe nanoparticles may distribute into tissues following systemic administration.
10. nC_{60}-AQ appear to elicit cytotoxicity through ROS and oxidative stress.
11. ZnO-MTAP conjugates elicit selective phototoxicity, apparently involving both apoptosis and necrosis. Apoptosis appeared mediated by caspase(s) and through ROS and oxidative stress.
12. An ovarian tumor model was successfully developed in nude mice by subcutaneous inoculation of NIH: OVCAR-3 cells. This model could be used in future *in vivo* studies to test the efficacy of nanoparticle conjugates.

REFERENCES

1. Hood E (2004) Nanotechnology: looking as we leap. *Environ Health Perspect* 112: A740-749
2. Hardman R (2006) A toxicologic review of quantum dots: toxicity depends on physicochemical and environmental factors. *Environ Health Perspect* 114: 165-172
3. Borm PJ, Robbins D, Haubold S, Kuhlbusch T, Fissan H, Donaldson K, Schins R, Stone V, Kreyling W, Lademann J, Krutmann J, Warheit D, Oberdorster E (2006) The potential risks of nanomaterials: a review carried out for ECETOC. *Part Fibre Toxicol* 3: 11
4. Oberdorster G, Oberdorster E, Oberdorster J (2005) Nanotoxicology: an emerging discipline evolving from studies of ultrafine particles. *Environ Health Perspect* 113: 823-839
5. Chan WC, Maxwell DJ, Gao X, Bailey RE, Han M, Nie S (2002) Luminescent quantum dots for multiplexed biological detection and imaging. *Curr Opin Biotechnol* 13: 40-46
6. Chen W, Joly AG, McCready DE (2005) Upconversion luminescence from CdSe nanoparticles. *J Chem Phys* 122: 224708
7. Morgan NY, English S, Chen W, Chernomordik V, Russo A, Smith PD, Gandjbakhche A (2005) Real time in vivo non-invasive optical imaging using

near-infrared fluorescent quantum dots. *Acad Radiol* 12: 313-323

8. Talapin DV, Rogach AL, Shevchenko EV, Kornowski A, Haase M, Weller H (2002) Dynamic distribution of growth rates within the ensembles of colloidal II-VI and III-V semiconductor nanocrystals as a factor governing their photoluminescence efficiency. *J Am Chem Soc* 124: 5782-5790
9. Bosi S, Da Ros T, Spalluto G, Prato M (2003) Fullerene derivatives: an attractive tool for biological applications. *Eur J Med Chem* 38: 913-923
10. Satoh M, Takayanagi I (2006) Pharmacological studies on fullerene (C60), a novel carbon allotrope, and its derivatives. *J Pharmacol Sci* 100: 513-518
11. Sijbesma R, Srdanov G, Wudl F, Castoro JA, Wilkins C, Friedman SH, DeCamp DL, Kenyon GL (1993) Synthesis of a fullerene derivative for the inhibition of HIV enzymes. *J Am Chem Soc* 115: 6510 - 6512
12. Tegos GP, Demidova TN, Arcila-Lopez D, Lee H, Wharton T, Gali H, Hamblin MR (2005) Cationic fullerenes are effective and selective antimicrobial photosensitizers. *Chem Biol* 12: 1127-1135
13. Mashino T, Okuda K, Hirota T, Hirobe M, Nagano T, Mochizuki M (1999) Inhibition of E. coli growth by fullerene derivatives and inhibition mechanism. *Bioorg Med Chem Lett* 9: 2959-2962
14. Harhaji L, Isakovic A, Raicevic N, Markovic Z, Todorovic-Markovic B, Nikolic N, Vranjes-Djuric S, Markovic I, Trajkovic V (2007) Multiple mechanisms underlying the anticancer action of nanocrystalline fullerene. *Eur J Pharmacol* 568: 89-98
15. Mashino T, Shimotohno K, Ikegami N, Nishikawa D, Okuda K, Takahashi K,

Nakamura S, Mochizuki M (2005) Human immunodeficiency virus-reverse transcriptase inhibition and hepatitis C virus RNA-dependent RNA polymerase inhibition activities of fullerene derivatives. *Bioorg Med Chem Lett* 15: 1107-1109

16. Miller GG, Romanova VS, Pokidysheva LN, Titova IV, Kaliberda EN, Rumsh LD, Andreeva OI, Rybalkin NP (2004) [HIV reproduction inhibition by amino acid and dipeptide derivatives of fullerene C60]. *Antibiot Khimioter* 49: 3-8
17. Ikeda A, Doi Y, Hashizume M, Kikuchi J, Konishi T (2007) An extremely effective DNA photocleavage utilizing functionalized liposomes with a fullerene-enriched lipid bilayer. *J Am Chem Soc* 129: 4140-4141
18. Yamakoshi YN, Yagami T, Sueyoshi S, Miyata N (1996) Acridine Adduct of [60]Fullerene with Enhanced DNA-Cleaving Activity. 61: 7236-7237
19. Dugan LL, Turetsky DM, Du C, Lobner D, Wheeler M, Almli CR, Shen CK, Luh TY, Choi DW, Lin TS (1997) Carboxyfullerenes as neuroprotective agents. *Proc Natl Acad Sci U S A* 94: 9434-9439
20. Cohen R, Velho V (2002) Update on respiratory disease from coal mine and silica dust. *Clin Chest Med* 23: 811-826
21. Chen SY, Hayes RB, Wang JM, Liang SR, Blair A (1989) Nonmalignant respiratory disease among hematite mine workers in China. *Scand J Work Environ Health* 15: 319-322
22. Perederii GS (1998) [The functional status and work capacity of coal mine workers with a history of an acute respiratory disease]. *Lik Sprava*: 164-167
23. Colvin VL (2003) The potential environmental impact of engineered

nanomaterials. *Nat Biotechnol* 21: 1166-1170

24. Frampton MW, Stewart JC, Oberdorster G, Morrow PE, Chalupa D, Pietropaoli AP, Frasier LM, Speers DM, Cox C, Huang LS, Utell MJ (2006) Inhalation of ultrafine particles alters blood leukocyte expression of adhesion molecules in humans. *Environ Health Perspect* 114: 51-58
25. Lam CW, James JT, McCluskey R, Hunter RL (2004) Pulmonary toxicity of single-wall carbon nanotubes in mice 7 and 90 days after intratracheal instillation. *Toxicol Sci* 77: 126-134
26. Warheit DB, Laurence BR, Reed KL, Roach DH, Reynolds GA, Webb TR (2004) Comparative pulmonary toxicity assessment of single-wall carbon nanotubes in rats. *Toxicol Sci* 77: 117-125
27. Oberdorster G (1996) Significance of particle parameters in the evaluation of exposure-dose-response relationships of inhaled particles. *Inhal Toxicol* 8 Suppl: 73-89
28. Morgan DL, Shines CJ, Jeter SP, Wilson RE, Elwell MP, Price HC, Moskowitz PD (1995) Acute pulmonary toxicity of copper gallium diselenide, copper indium diselenide, and cadmium telluride intratracheally instilled into rats. *Environ Res* 71: 16-24
29. Ballou B, Lagerholm BC, Ernst LA, Bruchez MP, Waggoner AS (2004) Noninvasive imaging of quantum dots in mice. *Bioconjug Chem* 15: 79-86
30. Voura EB, Jaiswal JK, Mattoussi H, Simon SM (2004) Tracking metastatic tumor cell extravasation with quantum dot nanocrystals and fluorescence emission-scanning microscopy. *Nat Med* 10: 993-998

31. Derfus AM, Chan WC, Bhatia SN (2004) Probing the Cytotoxicity of Semiconductor Quantum Dots *Nano Lett* 4 (1): 11-18

32. Lovric J, Bazzi HS, Cuie Y, Fortin GR, Winnik FM, Maysinger D (2005) Differences in subcellular distribution and toxicity of green and red emitting CdTe quantum dots. *J Mol Med* 83: 377-385

33. Chueh SC, Lai MK, Lee MS, Chiang LY, Ho TI, Chen SC (1999) Decrease of free radical level in organ perfusate by a novel water-soluble carbon-sixty, hexa(sulfobutyl)fullerenes. *Transplant Proc* 31: 1976-1977

34. Gharbi N, Pressac M, Hadchouel M, Szwarc H, Wilson SR, Moussa F (2005) [60]fullerene is a powerful antioxidant in vivo with no acute or subacute toxicity. *Nano Lett* 5: 2578-2585

35. Chen HH, Yu C, Ueng TH, Chen S, Chen BJ, Huang KJ, Chiang LY (1998) Acute and subacute toxicity study of water-soluble polyalkylsulfonated C60 in rats. *Toxicol Pathol* 26: 143-151

36. Yamawaki H, Iwai N (2006) Cytotoxicity of water-soluble fullerene in vascular endothelial cells. *Am J Physiol Cell Physiol* 290: C1495-1502

37. Nelson MA, Domann FE, Bowden GT, Hooser SB, Fernando Q, Carter DE (1993) Effects of acute and subchronic exposure of topically applied fullerene extracts on the mouse skin. *Toxicol Ind Health* 9: 623-630

38. Sayes CM, Gobin AM, Ausman KD, Mendez J, West JL, Colvin VL (2005) Nano-C60 cytotoxicity is due to lipid peroxidation. *Biomaterials* 26: 7587-7595

39. Sayes CM, Marchione AA, Reed KL, Warheit DB (2007) Comparative

pulmonary toxicity assessments of C60 water suspensions in rats: few differences in fullerene toxicity in vivo in contrast to in vitro profiles. *Nano Lett* 7: 2399-2406

40. Oberdorster E (2004) Manufactured nanomaterials (fullerenes, C60) induce oxidative stress in the brain of juvenile largemouth bass. *Environ Health Perspect* 112: 1058-1062
41. Isakovic A, Markovic Z, Nikolic N, Todorovic-Markovic B, Vranjes-Djuric S, Harhaji L, Raicevic N, Romcevic N, Vasiljevic-Radovic D, Dramicanin M, Trajkovic V (2006) Inactivation of nanocrystalline C60 cytotoxicity by gamma-irradiation. *Biomaterials* 27: 5049-5058
42. Shiohara A, Hoshino A, Hanaki K, Suzuki K, Yamamoto K (2004) On the cyto-toxicity caused by quantum dots. *Microbiol Immunol* 48: 669-675
43. Oberdorster G, Maynard A, Donaldson K, Castranova V, Fitzpatrick J, Ausman K, Carter J, Karn B, Kreyling W, Lai D, Olin S, Monteiro-Riviere N, Warheit D, Yang H (2005) Principles for characterizing the potential human health effects from exposure to nanomaterials: elements of a screening strategy. *Part Fibre Toxicol* 2: 8
44. Thomas K, Sayre P (2005) Research strategies for safety evaluation of nanomaterials, Part I: evaluating the human health implications of exposure to nanoscale materials. *Toxicol Sci* 87: 316-321
45. Thomas T, Thomas K, Sadrieh N, Savage N, Adair P, Bronaugh R (2006) Research strategies for safety evaluation of nanomaterials, part VII: evaluating consumer exposure to nanoscale materials. *Toxicol Sci* 91: 14-19

46. Gao X, Cui Y, Levenson RM, Chung LW, Nie S (2004) In vivo cancer targeting and imaging with semiconductor quantum dots. *Nat Biotechnol* 22: 969-976

47. Gannon CJ, Cherukuri P, Yakobson BI, Cognet L, Kanzius JS, Kittrell C, Weisman RB, Pasquali M, Schmidt HK, Smalley RE, Curley SA (2007) Carbon nanotube-enhanced thermal destruction of cancer cells in a noninvasive radiofrequency field. *Cancer* 110: 2654-2665

48. Elder A, Gelein R, Silva V, Feikert T, Opanashuk L, Carter J, Potter R, Maynard A, Ito Y, Finkelstein J, Oberdorster G (2006) Translocation of inhaled ultrafine manganese oxide particles to the central nervous system. *Environ Health Perspect* 114: 1172-1178

49. Sies H (1997) Oxidative stress: oxidants and antioxidants. *Exp Physiol* 82: 291-295

50. Parthasarathy S, Khan-Merchant N, Penumetcha M, Santanam N (2001) Oxidative stress in cardiovascular disease. *J Nucl Cardiol* 8: 379-389

51. MacNee W (2001) Oxidative stress and lung inflammation in airways disease. *Eur J Pharmacol* 429: 195-207

52. Kowluru V, Kowluru RA (2007) Increased oxidative stress in diabetes regulates activation of a small molecular weight G-protein, H-Ras, in the retina. *Mol Vis* 13: 602-610

53. Tas F, Hansel H, Belce A, Ilvan S, Argon A, Camlica H, Topuz E (2005) Oxidative stress in breast cancer. *Med Oncol* 22: 11-15

54. Battisti C, Formichi P, Radi E, Federico A (2008) Oxidative-stress-induced

apoptosis in PBLs of two patients with Parkinson disease secondary to alpha-synuclein mutation. *J Neurol Sci* 267: 120-124

55. Nathan C, Shiloh MU (2000) Reactive oxygen and nitrogen intermediates in the relationship between mammalian hosts and microbial pathogens. *Proc Natl Acad Sci U S A* 97: 8841-8848
56. Kontush K, Schekatolina S (2004) Vitamin E in neurodegenerative disorders: Alzheimer's disease. *Ann N Y Acad Sci* 1031: 249-262
57. Boothby LA, Doering PL (2005) Vitamin C and vitamin E for Alzheimer's disease. *Ann Pharmacother* 39: 2073-2080
58. Fong JJ, Rhoney DH (2006) NXY-059: review of neuroprotective potential for acute stroke. *Ann Pharmacother* 40: 461-471
59. Donaldson K, Borm P (2004) Particle and Fibre Toxicology, a new journal to meet a real need. *Part Fibre Toxicol* 1: 1
60. Donaldson K, Stone V, Tran CL, Kreyling W, Borm PJ (2004) Nanotoxicology. *Occup Environ Med* 61: 727-728
61. Baigi MG, Brault L, Neguesque A, Beley M, Hilali RE, Gauzere F, Bagrel D (2008) Apoptosis/necrosis switch in two different cancer cell lines: influence of benzoquinone- and hydrogen peroxide-induced oxidative stress intensity, and glutathione. *Toxicol In Vitro* 22: 1547-1554
62. Wochna A, Niemczyk E, Kurono C, Masaoka M, Kedzior J, Slominska E, Lipinski M, Wakabayashi T (2007) A possible role of oxidative stress in the switch mechanism of the cell death mode from apoptosis to necrosis--studies on rho0 cells. *Mitochondrion* 7: 119-124

63. Chatterjee S, Kundu S, Bhattacharyya A (2008) Mechanism of cadmium induced apoptosis in the immunocyte. *Toxicol Lett* 177: 83-89

64. Herzog KH, Schulz A, Buerkle C, Gromoll C, Braun JS (2007) Radiation-induced apoptosis in retinal progenitor cells is p53-dependent with caspase-independent DNA fragmentation. *Eur J Neurosci* 25: 1349-1356

65. Millar NL, Wei AQ, Molloy TJ, Bonar F, Murrell GA (2008) Heat shock protein and apoptosis in supraspinatus tendinopathy. *Clin Orthop Relat Res* 466: 1569-1576

66. Ndebele K, Gona P, Jin TG, Benhaga N, Chalah A, Degli-Esposti M, Khosravi-Far R (2008) Tumor necrosis factor (TNF)-related apoptosis-inducing ligand (TRAIL) induced mitochondrial pathway to apoptosis and caspase activation is potentiated by phospholipid scramblase-3. *Apoptosis* 13: 845-856

67. Jin CY, Moon DO, Lee JD, Heo MS, Choi YH, Lee CM, Park YM, Kim GY (2007) Sulforaphane sensitizes tumor necrosis factor-related apoptosis-inducing ligand-mediated apoptosis through downregulation of ERK and Akt in lung adenocarcinoma A549 cells. *Carcinogenesis* 28: 1058-1066

68. Eggert A, Grotzer MA, Zuzak TJ, Wiewrodt BR, Ho R, Ikegaki N, Brodeur GM (2001) Resistance to tumor necrosis factor-related apoptosis-inducing ligand (TRAIL)-induced apoptosis in neuroblastoma cells correlates with a loss of caspase-8 expression. *Cancer Res* 61: 1314-1319

69. Iitaka M, Kakinuma S, Fujimaki S, Oosuga I, Fujita T, Yamanaka K, Wada S, Katayama S (2001) Induction of apoptosis and necrosis by zinc in human

thyroid cancer cell lines. *J Endocrinol* 169: 417-424

70. Kumari MV, Hiramatsu M, Ebadi M (1998) Free radical scavenging actions of metallothionein isoforms I and II. *Free Radic Res* 29: 93-101
71. Giles NM, Watts AB, Giles GI, Fry FH, Littlechild JA, Jacob C (2003) Metal and redox modulation of cysteine protein function. *Chem Biol* 10: 677-693
72. Jemal A, Siegel R, Ward E, Murray T, Xu J, Thun MJ (2007) Cancer statistics, 2007. *CA Cancer J Clin* 57: 43-66
73. Herzog TJ (2006) The current treatment of recurrent ovarian cancer. *Curr Oncol Rep* 8: 448-454
74. Meden H, Fock M, Krauss T, Kuhn W (1999) [Efficiency, safety and tolerability of recombinant human interleukin-3 (rhIL-3) as supportive therapy accompanying dose-intensive carboplatin containing chemotherapy in ovarian cancer with special regard to thrombocytopenia]. *Zentralbl Gynakol* 121: 375-383
75. Deshane J, Siegal GP, Wang M, Wright M, Bucy RP, Alvarez RD, Curiel DT (1997) Transductional efficacy and safety of an intraperitoneally delivered adenovirus encoding an anti-erbB-2 intracellular single-chain antibody for ovarian cancer gene therapy. *Gynecol Oncol* 64: 378-385
76. Goff BA, Blake J, Bamberg MP, Hasan T (1996) Treatment of ovarian cancer with photodynamic therapy and immunoconjugates in a murine ovarian cancer model. *Br J Cancer* 74: 1194-1198
77. Ochsner M (1997) Photophysical and photobiological processes in the photodynamic therapy of tumours. *J Photochem Photobiol B* 39: 1-18

78. Canter RJ, Mick R, Kesmodel SB, Raz DJ, Spitz FR, Metz JM, Glatstein EJ, Hahn SM, Fraker DL (2003) Intraperitoneal photodynamic therapy causes a capillary-leak syndrome. *Ann Surg Oncol* 10: 514-524

79. Rovers JP, Saarnak AE, Molina A, Schuitmaker JJ, Sterenborg HJ, Terpstra OT (1999) Effective treatment of liver metastases with photodynamic therapy, using the second-generation photosensitizer meta-tetra(hydroxyphenyl)chlorin (mTHPC), in a rat model. *Br J Cancer* 81: 600-608

80. Jain KK (2008) Recent advances in nanooncology. *Technol Cancer Res Treat* 7: 1-14

81. Wieder ME, Hone DC, Cook MJ, Handsley MM, Gavrilovic J, Russell DA (2006) Intracellular photodynamic therapy with photosensitizer-nanoparticle conjugates: cancer therapy using a 'Trojan horse'. *Photochem Photobiol Sci* 5: 727-734

82. Yan F, Kopelman R (2003) The embedding of meta-tetra(hydroxyphenyl)-chlorin into silica nanoparticle platforms for photodynamic therapy and their singlet oxygen production and pH-dependent optical properties. *Photochem Photobiol* 78: 587-591

83. Ideta R, Tasaka F, Jang WD, Nishiyama N, Zhang GD, Harada A, Yanagi Y, Tamaki Y, Aida T, Kataoka K (2005) Nanotechnology-based photodynamic therapy for neovascular disease using a supramolecular nanocarrier loaded with a dendritic photosensitizer. *Nano Lett* 5: 2426-2431

84. Chen W, Zhang J (2006) Using nanoparticles to enable simultaneous

radiation and photodynamic therapies for cancer treatment. *J Nanosci Nanotechnol* 6: 1159-1166

85. Armelao L, Heigl F, Jurgensen A, Blyth RIR, Regier T, Zhou X-T, Sham TK (2007) X-ray Excited Optical Luminescence Studies of ZnO and Eu-Doped ZnO Nanostructures. *J Phys Chem C* 111: 10194-10200

86. Liu Y, Zhang Y, Wang S, Pope C, Chen W (2008) Optical behaviors of ZnO-porphyrin conjugates and their potential applications for cancer treatment. *Applied Physics Letters* 92. DOI 10.1063/1.2908211

87. Liu Y, Chen W, Joly AG, Wang Y, Pope C, Zhang Y, Bovin JO, Sherwood P (2006) Comparison of water-soluble CdTe nanoparticles synthesized in air and in nitrogen. *J Phys Chem B* 110: 16992-17000

88. Moser VC (1995) Comparisons of the acute effects of cholinesterase inhibitors using a neurobehavioral screening battery in rats. *Neurotoxicol Teratol* 17: 617-625

89. Campling BG, Pym J, Galbraith PR, Cole SP (1988) Use of the MTT assay for rapid determination of chemosensitivity of human leukemic blast cells. *Leuk Res* 12: 823-831

90. Li H, Burkhardt C, Heinrich UR, Brausch I, Xia N, Forstermann U (2003) Histamine upregulates gene expression of endothelial nitric oxide synthase in human vascular endothelial cells. *Circulation* 107: 2348-2354

91. Brant JA, Labille J, Bottero JY, Wiesner MR (2006) Characterizing the impact of preparation method on fullerene cluster structure and chemistry. *Langmuir* 22: 3878-3885

92. Shimizu T, Numata T, Okada Y (2004) A role of reactive oxygen species in apoptotic activation of volume-sensitive Cl(-) channel. *Proc Natl Acad Sci U S A* 101: 6770-6773

93. Yang Z, Yang S, Qian SY, Hong JS, Kadiiska MB, Tennant RW, Waalkes MP, Liu J (2007) Cadmium-induced toxicity in rat primary mid-brain neuroglia cultures: role of oxidative stress from microglia. *Toxicol Sci* 98: 488-494

94. Shaikh ZA, Vu TT, Zaman K (1999) Oxidative stress as a mechanism of chronic cadmium-induced hepatotoxicity and renal toxicity and protection by antioxidants. *Toxicol Appl Pharmacol* 154: 256-263

95. Frank J, Lambert C, Biesalski HK, Thews O, Vaupel P, Kelleher DK (2003) Intensified oxidative and nitrosative stress following combined ALA-based photodynamic therapy and local hyperthermia in rat tumors. *Int J Cancer* 107: 941-948

96. Luna MC, Ferrario A, Wong S, Fisher AM, Gomer CJ (2000) Photodynamic therapy-mediated oxidative stress as a molecular switch for the temporal expression of genes ligated to the human heat shock promoter. *Cancer Res* 60: 1637-1644

97. Borm PJ, Kreyling W (2004) Toxicological hazards of inhaled nanoparticles--potential implications for drug delivery. *J Nanosci Nanotechnol* 4: 521-531

98. Kim JS, Yoon TJ, Yu KN, Kim BG, Park SJ, Kim HW, Lee KH, Park SB, Lee JK, Cho MH (2006) Toxicity and tissue distribution of magnetic nanoparticles in mice. *Toxicol Sci* 89: 338-347

99. Moser VC, MacPhail RC (1987) Cholinergic involvement in the action of

formetanate on operant behavior in rats. *Pharmacol Biochem Behav* 26: 119-121

100. MacPhail RC (1987) Observational batteries and motor activity. *Zentralbl Bakteriol Mikrobiol Hyg [B]* 185: 21-27
101. Kirchner C, Liedl T, Kudera S, Pellegrino T, Munoz Javier A, Gaub HE, Stolzle S, Fertig N, Parak WJ (2005) Cytotoxicity of colloidal CdSe and CdSe/ZnS nanoparticles. *Nano Lett* 5: 331-338
102. Oberdorster G, Ferin J, Gelein R, Soderholm SC, Finkelstein J (1992) Role of the alveolar macrophage in lung injury: studies with ultrafine particles. *Environ Health Perspect* 97: 193-199
103. Kreyling WG, Semmler M, Erbe F, Mayer P, Takenaka S, Schulz H, Oberdorster G, Ziesenis A (2002) Translocation of ultrafine insoluble iridium particles from lung epithelium to extrapulmonary organs is size dependent but very low. *J Toxicol Environ Health A* 65: 1513-1530
104. Morgan DL, Shines CJ, Jeter SP, Blazka ME, Elwell MR, Wilson RE, Ward SM, Price HC, Moskowitz PD (1997) Comparative pulmonary absorption, distribution, and toxicity of copper gallium diselenide, copper indium diselenide, and cadmium telluride in Sprague-Dawley rats. *Toxicol Appl Pharmacol* 147: 399-410
105. Zhang Y, Chen W, Zhang J, Liu J, Chen G, Pope C (2007) In vitro and in vivo toxicity of CdTe nanoparticles. *J Nanosci Nanotechnol* 7: 497-503
106. Silverstein SC (1977) Endocytic uptake of particles by mononuclear phagocytes and the penetration of obligate intracellular parasites. *Am J Trop*

Med Hyg 26: 161-169

107. Brant J, Lecoanet H, Hotze M, Wiesner M (2005) Comparison of electrokinetic properties of colloidal fullerenes (n-C60) formed using two procedures. *Environ Sci Technol* 39: 6343-6351
108. Atsumi T, Iwakura I, Fujisawa S, Ueha T (2001) The production of reactive oxygen species by irradiated camphorquinone-related photosensitizers and their effect on cytotoxicity. *Arch Oral Biol* 46: 391-401
109. Kim JS, Yoon TJ, Yu KN, Noh MS, Woo M, Kim BG, Lee KH, Sohn BH, Park SB, Lee JK, Cho MH (2006) Cellular uptake of magnetic nanoparticle is mediated through energy-dependent endocytosis in A549 cells. *J Vet Sci* 7: 321-326
110. Qaddoumi MG, Gukasyan HJ, Davda J, Labhasetwar V, Kim KJ, Lee VH (2003) Clathrin and caveolin-1 expression in primary pigmented rabbit conjunctival epithelial cells: role in PLGA nanoparticle endocytosis. *Mol Vis* 9: 559-568
111. Tong L, Lu Y, Lee RJ, Cheng JX (2007) Imaging receptor-mediated endocytosis with a polymeric nanoparticle-based coherent anti-stokes Raman scattering probe. *J Phys Chem B* 111: 9980-9985
112. Chatterjee SR, Srivastava TS, Kamat JP, Devasagayam TP (1997) Lipid peroxidation induced by a novel porphyrin plus light in isolated mitochondria: possible implications in photodynamic therapy. *Mol Cell Biochem* 166: 25-33
113. Morgan J, Oseroff AR (2001) Mitochondria-based photodynamic anti-cancer therapy. *Adv Drug Deliv Rev* 49: 71-86

114. Hilf R (2007) Mitochondria are targets of photodynamic therapy. *J Bioenerg Biomembr* 39: 85-89

115. Edstrom DW, Porwit A, Ros AM (2001) Effects on human skin of repetitive ultraviolet-A1 (UVA1) irradiation and visible light. *Photodermatol Photoimmunol Photomed* 17: 66-70

116. Mahmoud BH, Hexsel CL, Hamzavi IH, Lim HW (2008) Effects of visible light on the skin. *Photochem Photobiol* 84: 450-462

117. Zarebska Z, Waszkowska E, Caffieri S, Dall'Acqua F (2000) PUVA (psoralen + UVA) photochemotherapy: processes triggered in the cells. *Farmaco* 55: 515-520

118. O'Donovan P, Perrett CM, Zhang X, Montaner B, Xu YZ, Harwood CA, McGregor JM, Walker SL, Hanaoka F, Karran P (2005) Azathioprine and UVA light generate mutagenic oxidative DNA damage. *Science* 309: 1871-1874

119. Song K, Kong B, Li L, Yang Q, Wei Y, Qu X (2007) Intraperitoneal photodynamic therapy for an ovarian cancer ascite model in Fischer 344 rat using hematoporphyrin monomethyl ether. *Cancer Sci* 98: 1959-1964

120. Wyld L, Reed MW, Brown NJ (2001) Differential cell death response to photodynamic therapy is dependent on dose and cell type. *Br J Cancer* 84: 1384-1386

121. Zhang AP, Sun YP (2004) Photocatalytic killing effect of TiO2 nanoparticles on Ls-174-t human colon carcinoma cells. *World J Gastroenterol* 10: 3191-3193

122. Uchino T, Tokunaga H, Ando M, Utsumi H (2002) Quantitative determination of OH radical generation and its cytotoxicity induced by TiO(2)-UVA treatment. *Toxicol In Vitro* 16: 629-635

123. Pathak N, Khandelwal S (2007) Role of oxidative stress and apoptosis in cadmium induced thymic atrophy and splenomegaly in mice. *Toxicol Lett* 169: 95-108

124. Shi L, Hernandez B, Selke M (2006) Singlet oxygen generation from water-soluble quantum dot-organic dye nanocomposites. *J Am Chem Soc* 128: 6278-6279

125. Henry TB, Menn FM, Fleming JT, Wilgus J, Compton RN, Sayler GS (2007) Attributing effects of aqueous C60 nano-aggregates to tetrahydrofuran decomposition products in larval zebrafish by assessment of gene expression. *Environ Health Perspect* 115: 1059-1065

126. Takahashi H, Itoh Y, Miyauchi Y, Nakajima S, Sakata I, Ishida-Yamamoto A, Iizuka H (2003) Activation of two caspase cascades, caspase 8/3/6 and caspase 9/3/6, during photodynamic therapy using a novel photosensitizer, ATX-S10(Na), in normal human keratinocytes. *Arch Dermatol Res* 295: 242-248

127. Plaetzer K, Kiesslich T, Oberdanner CB, Krammer B (2005) Apoptosis following photodynamic tumor therapy: induction, mechanisms and detection. *Curr Pharm Des* 11: 1151-1165

128. Matsubara A, Nakazawa T, Noda K, She H, Connolly E, Young TA, Ogura Y, Gragoudas ES, Miller JW (2007) Photodynamic therapy induces caspase-

dependent apoptosis in rat CNV model. *Invest Ophthalmol Vis Sci* 48: 4741-4747

129. Granville DJ, Levy JG, Hunt DW (1997) Photodynamic therapy induces caspase-3 activation in HL-60 cells. *Cell Death Differ* 4: 623-628

130. Gad F, Viau G, Boushira M, Bertrand R, Bissonnette R (2001) Photodynamic therapy with 5-aminolevulinic acid induces apoptosis and caspase activation in malignant T cells. *J Cutan Med Surg* 5: 8-13

131. Hoerter JD, Ward CS, Bale KD, Gizachew AN, Graham R, Reynolds J, Ward ME, Choi C, Kagabo JL, Sauer M, Kuipers T, Hotchkiss T, Banner N, Chellson RA, Ohaeri T, Gant L, Vanderhill L (2008) Effect of UVA fluence rate on indicators of oxidative stress in human dermal fibroblasts. *Int J Biol Sci* 4: 63-70

132. Maziere C, Conte MA, Leborgne L, Levade T, Hornebeck W, Santus R, Maziere JC (2001) UVA radiation stimulates ceramide production: relationship to oxidative stress and potential role in ERK, JNK, and p38 activation. *Biochem Biophys Res Commun* 281: 289-294

VITA

Yongbin Zhang

Candidate for the Degree of

Doctor of Philosophy

Dissertation: TOXICOLOGICAL AND PHARMACOLOGICAL ACTIONS OF ENGINEERED NANOMATERIALS

Major Field: Veterinary Biomedical Sciences

Biographical:

Education: Received Degree of Doctor of Veterinary Medicine from China Agricultural University in China in July 1997. Completed the requirements for Ph.D. Degree in Veterinary Biomedical Sciences at Oklahoma State University, Stillwater, Oklahoma in May, 2009.

Experience: Trained as a veterinary medicine student at China Agricultural University in China from 1992 to1997. Employed as a technical representative and manger at Beijing Miwon Feedstuff Company. Employed as a technical representative in Intervet International. Employed as a graduate research assistant at Oklahoma State University from 2004 to present.

Professional Memberships: Society of Toxicology, International Neurotoxicology Association

Name: Yongbin Zhang Date of Degree: May, 2009

Institution: Oklahoma State University Location: Stillwater, Oklahoma

Title of Study: TOXICOLOGICAL AND PHARMACOLOGICAL ACTIONS OF ENGINEERED NANOMATERIALS

Pages in Study: 146 Candidate for the Degree of Doctor of Philosophy

Major Field: Veterinary Biomedical Sciences (Toxicology)

Scope and Method of Study:

The toxicity of selected synthetic nanomaterials was studied using both *in vitro* and *in vivo* approaches. The toxicity of inorganic CdTe nanoparticles was first evaluated using both human HepG2 cells *in vitro* and systemic exposure in male rats *in vivo*. Cytotoxicity of organic fullerene aggregates was also evaluated in HepG2 cells. The potential utility of zinc oxide nanomaterials conjugated to a porphyrin derivative in the photodynamic therapy of ovarian cancer cells *in vitro* was evaluated. Mechanistic studies to determine the role of reactive oxygen species and oxidative stress in the cytotoxicity of all of these nanomaterials were conducted. A number of techniques/approaches including neurobehavioral assessments, biochemical assays, real-time PCR, western blotting, and both electron and confocal microscopy were used to address the biological consequences of nanomaterial exposure.

Findings and Conclusions:

1. CdTe nanoparticle-induced cytotoxicity is size- and concentration-dependent, involving caspase(s) activation, DNA fragmentation and metallothionein induction, but apparently not oxidative stress.
2. CdTe altered motor activity following *in vivo* dosing, suggesting possible disruption of nervous system function.
3. Subcellular distribution of CdTe was size- and time- dependent.
4. Intact CdTe nanoparticles appeared to distribute into tissues following intravenous administration in rats.
5. Surface properties, size, chemical composition, and purity of nanomaterial preparations can all contribute to nanotoxicity.
6. Fullerene aggregates appeared to elicit cytotoxicity via oxidative stress.
7. ZnO conjugates elicited selective phototoxicity involving both apoptosis and necrosis, mediated by caspase(s) activation and oxidative stress.

ADVISER'S APPROVAL: Carey Pope